The Stability of Ti_2AlC and V_2AlC with Al, and the Synthesis of Composites in the Al-Ti-B-C and Al-V-C systems

A Thesis

Submitted to the Faculty

of

Drexel University

by

Matthias Thomas Agne

in partial fulfillment of the

requirements for the degree of

Master of Science in Materials Science and Engineering

June 2015

Acknowledgements

Without unwavering support from my family I could never have accomplished what I have thus far. Mel, Suzi, and Graham, thank you for being a great family unit. I love you all.

To Dr. Michel Barsoum: I have the greatest respect and appreciation for your advisorship, instruction, and encouragement. To my friends and fellow researchers in the MAX/MXene group, particularly Dr. Babak Anasori, Dr. Darin Tallman, Grady Bentzel, and Michael Ghidu: your friendship and collaboration has been most enjoyable.

To the United States Army Research Office for making this work possible.

To Janette, Eric, Evan, and Emily for keeping me sane for the majority of my time at Drexel. We have been through a lot together and I am excited to see where life takes you.

To all of my friends and acquaintances who have given their time and resources for me, thank you and God bless.

Table of Contents

LIST OF TABLES

LIST OF FIGURES

.

Abstract

The Stability of Ti_2AlC and V_2AlC with Al, and the Synthesis of Composites in the Al-Ti-B-C and Al-V-C systems

Matthias T. Agne

Michel W. Barsoum, PhD.

As automotive, aerospace and the power industries increasingly look to carbide and boride based aluminum composites for their high specific strengths and increased thermal stability, it is important to characterize the equilibrium phase relations at temperatures common for processing these composites. Herein, two composite systems were investigated. Composites in the Al-Ti-B-C system were fabricated starting with Al, Ti_2AlC, and B_4C. Composites in the Al-V-C system were fabricated starting with elemental powders. The Ti_2AlC/B_4C powders were mixed in both 50/50 and 75/25 vol. % ratios and cold pressed into 53 % dense preforms. The preforms were pressureless melt infiltrated in the 900 to 1050 °C temperature range with Al. X-ray diffraction, XRD, and scanning electron microscopy, SEM, confirmed that neither Ti_2AlC nor B_4C was an equilibrium phase. The equilibrium phases were found to be Al, TiB_2, Al_3BC, and Al_4C_3 for the more B-rich composite and Al, TiB_2, TiC, and Al_4C_3 for the Ti-rich composite. From these results, the 1000 °C quaternary phase diagram adjacent to the Al-TiB_2-Al_4C_3 triangle and in the Al-rich corner was developed for the first time.

In the Al-V-C system, Al-V_2AlC composites were synthesized in situ by quenching from 1000 °C, however fully dense composites have yet to be realized. XRD and SEM investigations indicated a predominately two phase composite (Al and V_2AlC), and that some Al particles did not break their oxide shell. Furnace cooled samples did

not form two phase composites. Differential scanning calorimetry was used to determine the instability of V_2AlC with Al below ≈ 950 °C. Additionally, the Al-V-C phase diagram was characterized in the Al-rich corner at 800 °C. Al and V_2AlC were found to be in equilibrium with both Al_3V and Al_4C_3, but not with each other.

Chapter 1.
Introduction

1.1. Composites

Composite materials are generally classified as the combination of two or more constituent materials, having different properties, so that their combination enhances the properties of the conglomerate. It is advantageous to keep the constituent materials separate – as distinguished from dissolved, reacted or blended together – but combined in such a way as to form a solid unit of material. In this manner, the goal is to fabricate a composite with the best properties of each constituent material without accentuating their shortcomings. The progress of composite materials is, therefore, to contribute to the constant endeavor to optimize material properties.

Composites found in nature offer some perspective to the variety of material combinations that have existed before the efforts of materials science. Wood is a fibrous composite consisting of cellulose fibers in a lignin matrix. The combination of these two materials gives wood its strength and flexibility: the cellulose has high tensile strength but low stiffness and the lignin matrix holds the fibers together and provides rigidity [1]. Additionally, mollusk shells are composites containing 95 vol. % $CaCO_3$ platelets held together by a 5 vol. % protein-polysaccharide matrix. Due to the interlocking facets of the $CaCO_3$ platelets, the shell is about 10 times harder than monolithic $CaCO_3$. The addition of the polymer matrix prevents the shell from being too brittle, increasing the toughness by 1000 times that of monolithic $CaCO_3$ [2]. These are but two examples of natural

composites that demonstrate polymer-polymer and ceramic-polymer composites, respectively. Further examples of composites in nature are detailed elsewhere [3].

Mankind's experience with composites began by adding stone, straw or other reinforcement to mud bricks, and later limestone. The mud or limestone provides structural support under compression, but is easily broken under bending. The addition of fiber reinforcement to the brick increases its tensile strength [4]. While humanity has been using composites in the practical sense for thousands of years, the discipline of composites science has only been recognized since the early 1960s [1]. There is a demand from aerospace, transportation, energy and civil construction industries to develop lightweight materials with higher strength and stiffness than current materials. Composite systems may provide some of these solutions.

1.2. Metal matrix composites

Composites usually consist of a reinforcing phase dispersed in a matrix and have properties that are better than those of their individual components. When a metal is used as the matrix, the composite is called a metal matrix composite, MMC. The latter are custom made composites in which properties are tailored to fulfill the desired requirements. The first scientifically fabricated metal matrix composite can be dated back to 1924, when Schimd consolidated a mixture of aluminum and aluminum oxide powder as a dispersion hardened system and achieved higher hardness values than that of as cast aluminum [5].

Continuously reinforced MMCs were extensively investigated during the 1960s, in which high vol. % of the reinforcement (40-80 vol. %) was used. The role of the

matrix is mostly to transfer the applied load to reinforcement. The latter is the load-bearing component. The main disadvantages of these composites were high cost and limitations of fabrication.

In the 1980s discontinuously reinforced composites gained interest, with the development of Al composites reinforced with SiC and Al_2O_3 particles. The fraction of reinforcement is usually in the range of 5- 40 vol.%, which means that both the matrix and reinforcement contribute in load bearing. These composites become the most commercially attractive system due to their low cost, good workability and uniform properties compare to continuously reinforced composites.

1.3. Aluminum, its alloys and composites

Aluminum is the most abundant metal in the earth's crust, but is largely contained in rocks and minerals: two of the most common being potassium aluminum sulfate ($KAl(SO_4)_2 \cdot 12\ H_2O$) and aluminum oxide ($Al_2O_3$). Aluminum was first isolated by the Danish chemist, Hans Christian Oersted, in 1825; however, it was not until the 1880s that less expensive techniques to synthesize Al were developed. Having a relatively low density (2.7 g/cm^3), a melting temperature of 660 °C and a modulus of 70 GPa, as well as good corrosion resistance and machinability, Al was the choice material for the engine in the Wright brothers first airplane of 1903. Since the mass refinement of aluminum by the Pittsburg Reduction Company, now known as the Aluminum Company of America or Alcoa, in 1890, Al has been used as a lightweight structural material.

Common Al alloys include the addition of one or more of the following: copper, silicon, magnesium, manganese, zinc or lithium. The properties of Al alloys have been

well characterized [6]. These elemental additions have the tendency to increase the tensile strength of the material (Figure 1) while retaining a relatively low density; however, they do not necessarily address the relatively low hardness of Al or significantly increase the compressive strength. One method to overcome these limitations is to fabricate Al matrix composites. Among different reinforcement materials, ceramic reinforcements are commonly used in Al composites. Common ceramic reinforcements include: Al_2O_3, SiC [7], B_4C [8], TiC [9], and TiB_2 [10].

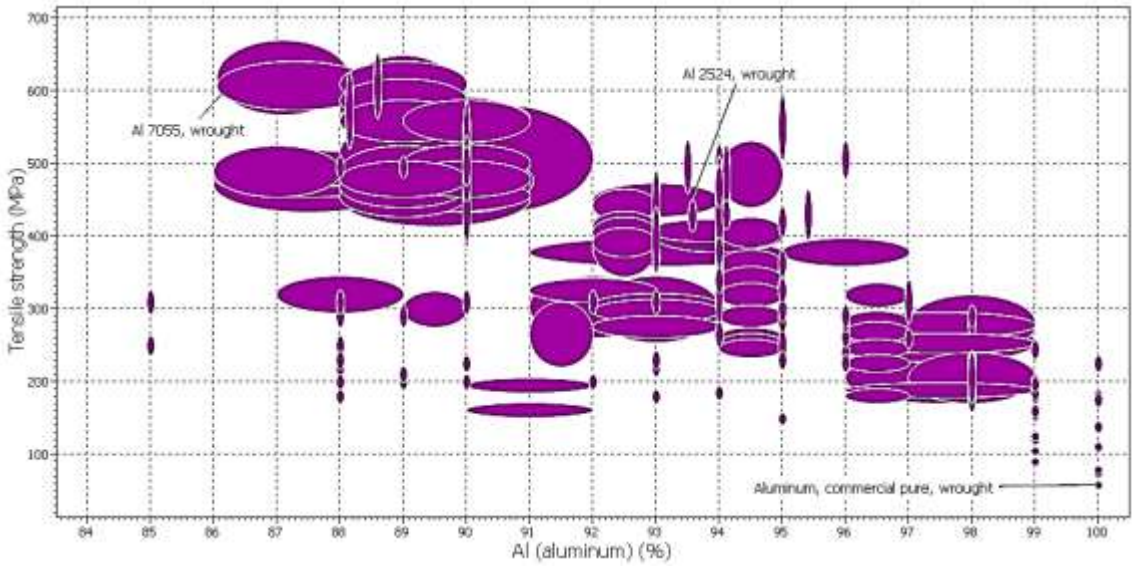

Figure 1. An Ashby plot demonstrating the general increase in tensile strength with increased amount of alloying elements in aluminum alloys.

Recent attempts to use Ti_2AlC, a MAX phase, to reinforce Al/Al-alloys have been undertaken, with limited success [11, 12]. Herein, we investigate possible methods of synthesizing near-net shape Al-MAX composites, using Ti_2AlC and V_2AlC, and to assess thermodynamic and/or kinetic factors that allow or prevent their fabrication.

Chapter 2.
Background

2.1. Introduction

Metal matrix composites, MMCs, attempt to combine the advantageous properties of both metals and ceramics. Wear resistance, fatigue and fracture resistance, and reduced coefficient of thermal expansion (compared to the metal matrix) are attractive reasons to incorporate ceramic reinforcements into metal matrices, while retaining the good thermal and electrical conductivities, and machinability of metals [13]. Mixing of a metal, or alloy, with a reinforcement phase may be achieved through a variety of processes, such as stir casting, melt infiltration, powder metallurgy, among others [13]. Common ceramic reinforcements include: Al_2O_3, SiC [7], B_4C [8], TiC [9], and TiB_2 [10]. A more thorough review of MMCs and their properties may be found elsewhere [13, 14].

2.2. Aluminum matrix composites

Reinforcements in Al matrix composites, as with other MMCs, may be particles, short fibers or whiskers – each having their advantages. The earliest attempts to reinforce aluminum alloys were based on the incorporation of particles such as graphite powder, but only low volume fractions of particles have been incorporated (< 10%). Higher volume fractions of reinforcement have been achieved for various kinds of ceramic particles (oxide, carbide, nitride); however, while particles lead to a favorable effect on properties such as hardness, wear resistance and compression strength, fibers are expected to have more influence on rigidity and tensile strength [15]. A comparison of the

mechanical properties for some Al matrix composites with various reinforcements is presented in Table 1.

Table 1. Comparison between various factors influencing the strength of discontinuously reinforced Al MMCs [15].

Composite Nature	Volume fraction of reinforcement (%)	E (GPa)	YS (MPa)	UTS (MPa) at 20 °C	UTS (MPa) at 350 °C
Al 1Mg 0.6Si Al_2O_3 PM	29	91-96	390	385	120
Al 1Mg 0.6Si Al_2O_3 Squeeze Cast	20	92	260	360	120
Al 12Si Cu Ni SiC whiskers Squeeze Cast	12	95	266	359	124
	20	11	298	384	181
Al 12Si Cu Ni Al_2O_3 Squeeze Cast	12	83	251	273	74
	20	95	281	313	113
Al 1Mg 0.6Si SiC whiskers PM	15	91		306	
Al 4Cu 1Mg SiC whiskers PM	15	90		406	
Al 1Mg 0.6Si SiC powder PM	30	126	380	450	
Al 1Mg 0.6Si SiC whiskers PM	18	98	420	450	
Al 4.5Cu Al_2O_3 LPS	10	74	221	305	144
Al 4.5Cu SiC LPS	10	46	201	217	145

* PM and LPS stand for powder metallurgy and liquid phase stirring, respectively.

Al-matrix composites reinforced with silicon carbide, SiC, titanium carbide, TiC, and/or boron carbide, B_4C, have been targeted as families of lightweight materials with the potential to operate at temperatures above those of Al and its alloys. The high hardness typical of boride and carbide-containing composites also makes them attractive

for high wear applications. Their chemical stability and neutron absorption properties render them appealing in nuclear and other demanding industrial settings [16, 17].

2.3. Mg-MAX composites

Since 2009, magnesium matrix composites reinforced with Ti_2AlC – a member of the MAX phases - have been developed [18-21]. The MAX are a family of nanolayered, machinable, ternary carbides and nitrides, having the general formula $M_{n+1}AX_n$ – where n = 1, 2, 3; M is an early transition metal; A is an A-group element (mostly groups 13 and 14); and X is C and/or N [22]. The MAX phases combine some of the best properties of metals and ceramics. Like metals they are machinable, electrically and thermally conductive [23, 24], damage tolerant and not susceptible to thermal shock [25]. Like ceramics, some of them are lightweight (≈ 4 Mg/m^3) and elastically rigid (Young's moduli > 300 GPa). Ti_2AlC is also creep, fatigue and oxidation resistant [22, 26-28].

The aforementioned Mg and Mg alloys-MAX composites were manufactured by spontaneous melt infiltration, MI, at relatively low processing temperatures (750 °C) yielding composites with attractive mechanical properties. For example, the Young's modulus and ultimate compressive strengths, UCSs, of a Mg alloy (AZ61) matrix composite reinforced with 50 vol. % Ti_2AlC particles were measured to be 136±6 GPa and 760±9 MPa, respectively [20]. In addition to the excellent mechanical properties, these composites can also dissipate almost 25 % of the applied mechanical energy at high stresses [20, 29]. Additionally, Mg composites with the MAX phases Ti_3SiC_2 and Cr_2AlC have been successfully synthesized and have been compared to Mg-Ti_2AlC composites (Fig. 2) [21]. The resulting composites were also most readily machinable, since each

constituent is machinable. These promising results spurred interest in developing Al-MAX composites with comparable or better properties.

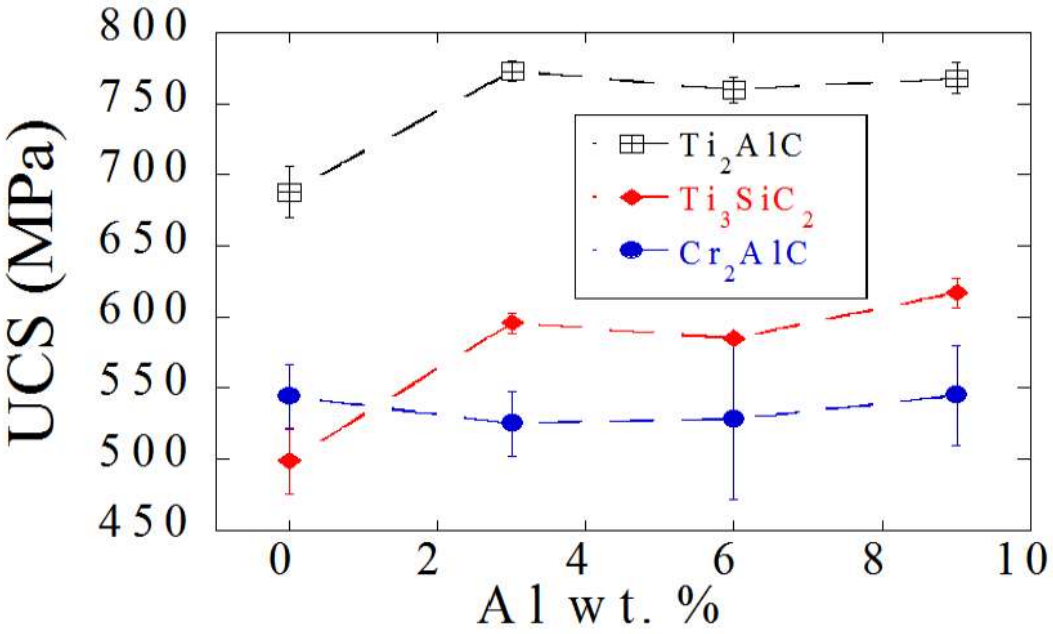

Figure 2. Comparison of UCS testing results vs. Al wt. % content for several Mg-MAX composites [21].

2.4. Al-MAX composites

Fabricating Al-matrix MAX reinforced composites is complicated by the fact that Al is not in equilibrium with most MAX phases [22]. For example, Wang et al. [11] attempted to fabricate Ti_3AlC_2 composites at elevated temperatures and found that above 950 °C, Ti_3AlC_2 reacted with Al to form TiC and $TiAl_3$. To circumvent this problem Wang et al. [11] hot pressed Al and Ti_3AlC_2 powders at a temperature (550 °C) at which the reaction kinetics were slow. More recently, Hu et al. [12] used current-activated, pressure-assisted infiltration to fabricate Al-Ti_2AlC composites. In this method, the processing and densification occur too rapidly for extensive reactions to occur. Their

nearly full dense composites were lightweight with UCS's of the order of 500 MPa. At 160 MPa cm^3/g, their specific strengths were approximately 4 times higher than those of pure Al [12]. These solutions to the problem, however, do not lend themselves to rapid, near-net shape, inexpensive manufacturing.

One goal of this work was to fabricate Al-Ti_2AlC composites via MI. However, preliminary results obtained herein showed that porous Ti_2AlC preforms were not easily wet by molten Al even at 1000 °C. At higher temperatures, the reaction was quite intense and did not result in a usable material. To avoid reaction with Al, one MAX phase that has been reported to be in equilibrium with liquid Al at 1000 °C is V_2AlC [30]. However, the extent of its thermodynamic stability and its use as a reinforcement phase in Al MMCs has been uninvestigated.

2.5. Wetting of Al on carbide ceramics

Poor wetting by Al is not unique to Ti_2AlC, but is also encountered when fabricating MMCs with other carbides, such as TiC, B_4C and SiC [31]. Typically temperatures greater than 1000 °C are necessary for Al to wet TiC and/or B_4C preforms in MI experiments [8, 9]. It has been previously reported that Ti additions to B_4C porous preforms enhance the infiltration kinetics of Al into the latter [8], which coincides with the finding that Ti-B interactions aid in the reactive wetting of Al on ceramic surfaces [32], though the reaction mechanisms and phase equilibria remain largely un-investigated [8]. Nevertheless, this interest in manufacturing Al matrix composites with both borides and carbides [33] would be greatly aided by an understanding of the reaction mechanisms and especially the equilibrium phase relations of these systems.

2.6. Scope of this work

This work sought to enhance the infiltration kinetics of Al into Ti_2AlC at lower temperatures by incorporating B_4C in the preforms, in an attempt to reduce or eliminate the high temperature reactions observed between Ti_2AlC and Al. When it was found that in all cases, a reaction occurred, the focus of the work shifted to understanding the equilibrium phase relations in the Al-Ti-B-C quaternary system at 1000 °C.

Additionally, we sought to synthesize an Al-V_2AlC composite and to characterize the thermodynamic stability between the MAX phase and Al in the temperature range typical for manufacturing these composites. Before doing so, it is important to review the following phase diagrams.

Chapter 3.
Phase Diagrams

3.1. Al-B system

Currently, only the binary phases AlB_2 and AlB_{12} have been shown to be pure Al-borides [34]. AlB_2 is stable to at least 956±5 °C. Above that temperature it peritectically transforms according to [35]

$$AlB_2 \leftrightarrow AlB_{12} + Al\ (liquid) \quad (1)$$

Others reported that the transformation temperature may be as high as 972±5 °C [36]. AlB_{12} is stable to ≈ 2000 °C. The solubility of B in liquid Al at 1100 °C is about 7 at.%.

3.2. Al-C system

The only binary phase in the Al-C system is Al_4C_3. And while this phase has been reported to be stable to above 2100 °C [37], when in contact with $TiAl_3$ will react to form TiC and Al at ≈ 877 °C [38]. The solubility of C in Al is negligible in the temperature range used herein [37].

3.3. Al-Ti system

A multitude of binary intermetallic phases exist between Al and Ti, that include Ti_3Al, TiAl, Ti_3Al_5, $TiAl_2$, Ti_2Al_5, Ti_5Al_{11}, and $TiAl_3$ [39]. At 1000 °C, the stable phases are: α-Ti, β-Ti, $TiAl_3$, TiAl, $TiAl_2$, Ti_2Al_5, and $TiAl_3$ [39, 40].

3.4. Al-V system

The latest review of the Al-V phase diagram has been compiled by Okamoto

(2012) [41]. Here it can be clearly seen that Al_3V and Al_8V_5 are equilibrium phases at 1000 °C, while the Al-rich phases – $Al_{23}V_4$, $Al_{45}V_7$ and $Al_{21}V_2$ – only exist below 734 °C, when Al_3V falls out of equilibrium with liquid Al. The V-rich side of the phase diagram is primarily a V-Al solid solution above ≈50-60 at.% V. The ordered phase AlV_3 is shown to exist; however, discrepancies between studies have been noted [42].

3.5. Ti-B system

Initial investigations of the Ti-B system suggested the existence of the binary phases Ti_2B and Ti_2B_5 [43], however the existence of these phases has since been refuted. The current Ti-B phase diagram, shows only the binary phases TiB, Ti_3B_4 and TiB_2, all of which are stable to ≈ 2000 °C [44].

3.6. Ti-C system

Non-stoichiometric TiC_y ($0.47 < y < 1.00$) is the only Ti-C binary phase in the Ti-C system. The existence of various ordered phases such as Ti_2C, Ti_6C_5, and Ti_3C_2 have sometimes been reported, however [45].

3.7. V-C system

V_2C, VC_{1-x}, V_6C_5, and V_8C_7 are stable phases at 1000 °C and have been well characterized [46, 47]. The only other phase known to exist in this system is V_4C_{3-y} at temperatures between 1260 and 1870 °C. Okamoto (2010) [47] has provided the most current assessment of the V-C phase diagram.

3.8. B-C system

Within the B-C system, the only known binary phase is B_4C, with B-rich (carbon deficient) variations of the form B_4C_{1-z} ($0 < z < 0.55$) [43, 45]. This phase is thermally stable to nearly 2500 °C. An extensive review of the history, processing, and properties of B_4C can be found in the literature [48].

3.9. Al-B-C system

Figure 3 re-plots the Al-B-C ternary phase diagram used herein [49]. Some confusion has been associated with the phases reported in the Al-B and Al-B-C systems [49]. For example, the existence of stoichiometric AlB_{10} was first reported [50], but was later shown, by Matkovich et al. [51], to contain carbon such that its chemistry was better described by $AlB_{24}C_4$ [51].

More than forty phases are known to exist in the Al-B-C system [49]. Isothermal experiments carried out at 900, 1000, and 1400 °C have been used to tentatively draw conclusions about equilibrium relations [49]. The stable phases reported at 900 °C – including Al_4C_3, Al_3BC, Al_3BC_3, $Al_3B_{48}C_2$ and B_4C– remain stable at 1000 °C (Fig. 1a). Since this work deals with the Al rich-corner of the quaternary phase diagram, the only relevant phase is Al_3BC. The latter is reported to be stable to ≈ 1100°C, after which it reacts with AlB_{12} to form $Al_3B_{48}C_2$ and liquid Al [49].

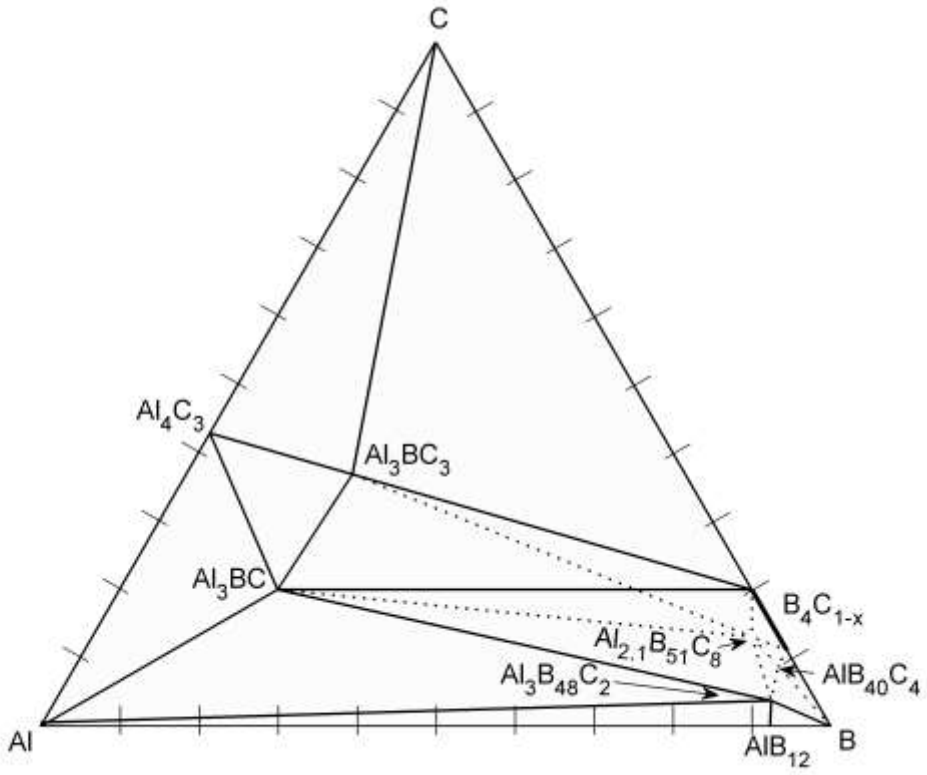

Figure 3. Isothermal ternary diagram at 1000°C of the Al-B-C system as presented by Grytsiv (2009) [49].

3.10. Al-Ti-C system

Isothermal sections of the Al-Ti-C system have been extensively investigated over the 727 °C to 1300 °C temperature range, with reproducibility between studies [40]. Of the three ternary phases known to exist, two - Ti_3AlC_2 and Ti_2AlC - belong to the MAX phase family [22]; the third, Ti_3AlC, has a perovskite-type crystal structure [39].

Both Ti_2AlC and Ti_3AlC can be found in the ternary system at every temperature between 750 °C and 1300 °C. However, according to Pietzka and Schuster [39], Ti_3AlC_2 is not an equilibrium phase at, or below, 1000 °C. The equilibrium relations at 1000 °C

(Fig. 4) and 1300 °C have become the standard for this system [39]. For simplicity, this study considers TiC_y to be stoichiometric TiC (see below) and is demonstrated as such in the ternary phase diagram.

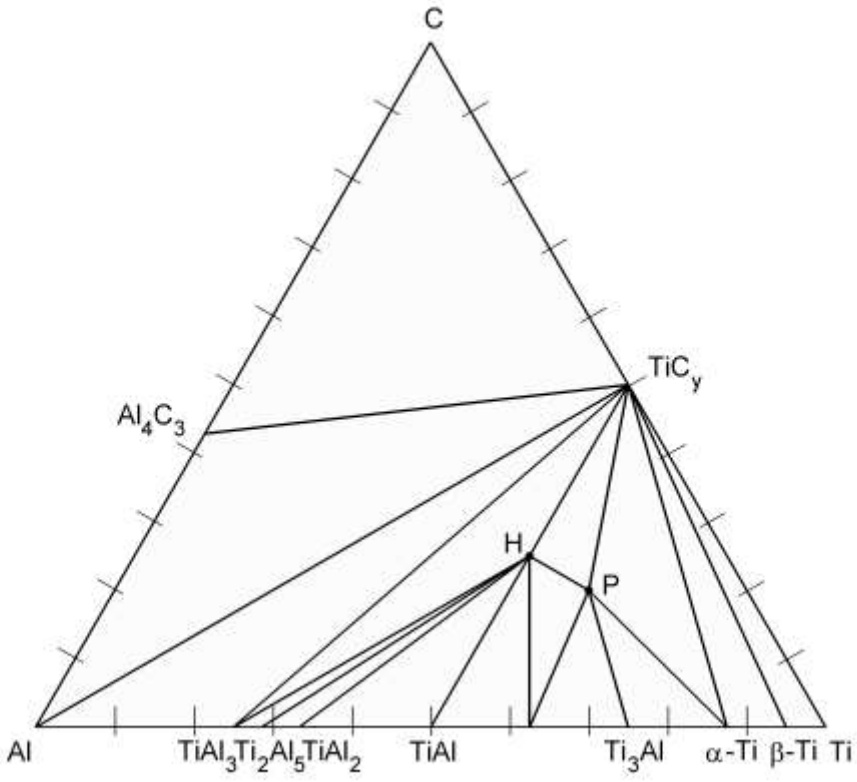

Figure 4. Isothermal ternary diagram at 1000°C of the Al-Ti-C system as presented by Pietzka and Schuster (1994), where H and P represent the Ti_2AlC and Ti_3AlC phases, respectively [39].

3.11. Ti-B-C system

There are no ternary compounds in this system. The phase relations between the binary phases have been well established (Fig. 5) [45].

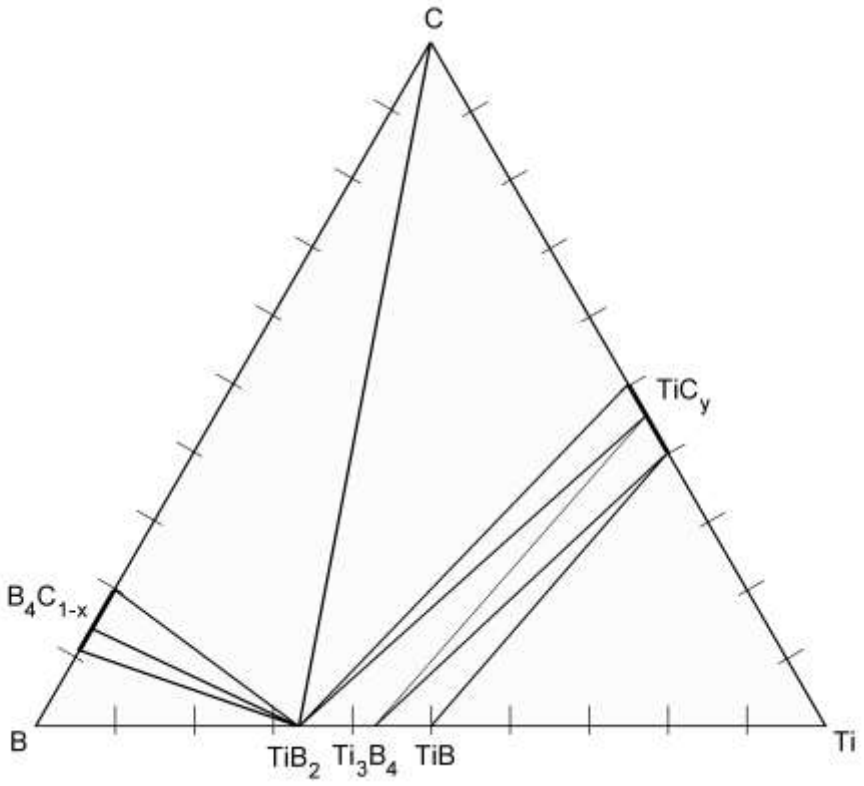

Figure 5. Isothermal ternary diagram at 1000°C of the Ti-B-C system as presented by Gusev (1997) [45].

3.12. Al-Ti-B system

No ternary phases exist in this system either. Isothermal sections at 800, 1000, 1350, and 1550 °C exist and show a dependence of the equilibrium phase relations with temperature. The most notable change in equilibrium relations is that TiB_2 and AlB_2 are in equilibrium at 800 °C, but not at, or above, 1000 °C [52]. This is due to the thermodynamic instability of AlB_2 due to the aforementioned decomposition reaction (Eq. 1), though it should be noted that the transformation rate is slow [35, 53]. The computationally determined Al-Ti-B isotherms generated by Witusiewicz et al. [54] have been confirmed by experimental results and provide reliable equilibrium phase relations

at 1000 °C (Fig. 6). Again, non-stoichiometric phases are demonstrated as point compounds.

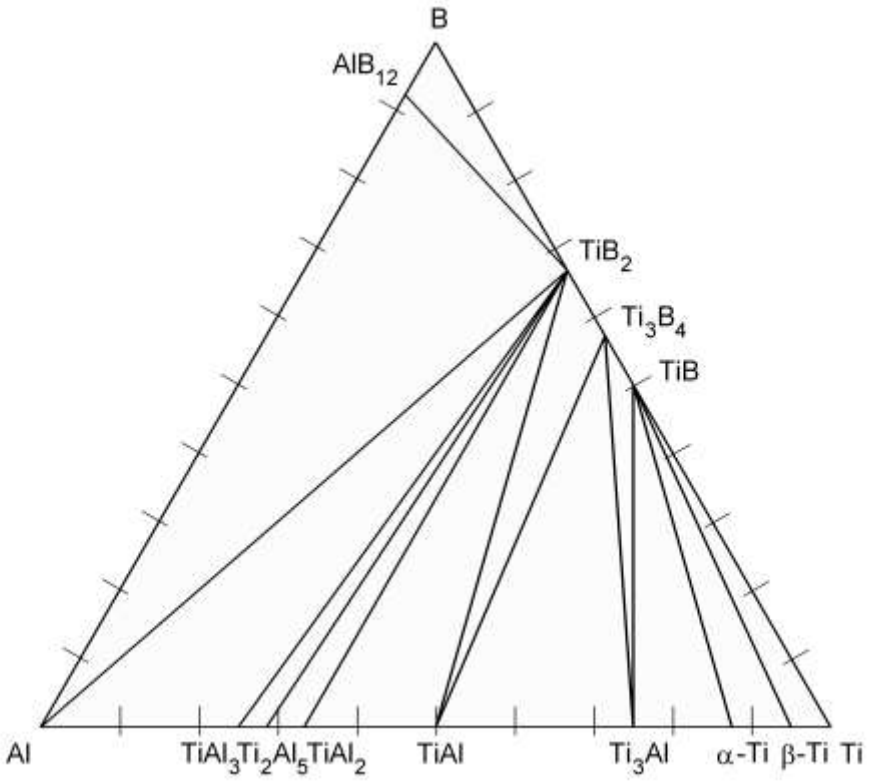

Figure 6. Isothermal ternary diagram at 1000°C of the Al-Ti-B system as presented by Witusiewicz et al. [54].

3.13. Al-V-C system

Schuster, et al. (1980) [30] have investigated the full Al-V-C compositional range at 1000 °C (Fig. 7). Only one ternary phase, V_2AlC, has been demonstrated to exist. The observed binary phases are in agreement with those reported for the binary systems at 1000 °C. V_2AlC is found to exist in equilibrium with liquid Al, the V-Al solid solution and all the binary phases, but not with C.

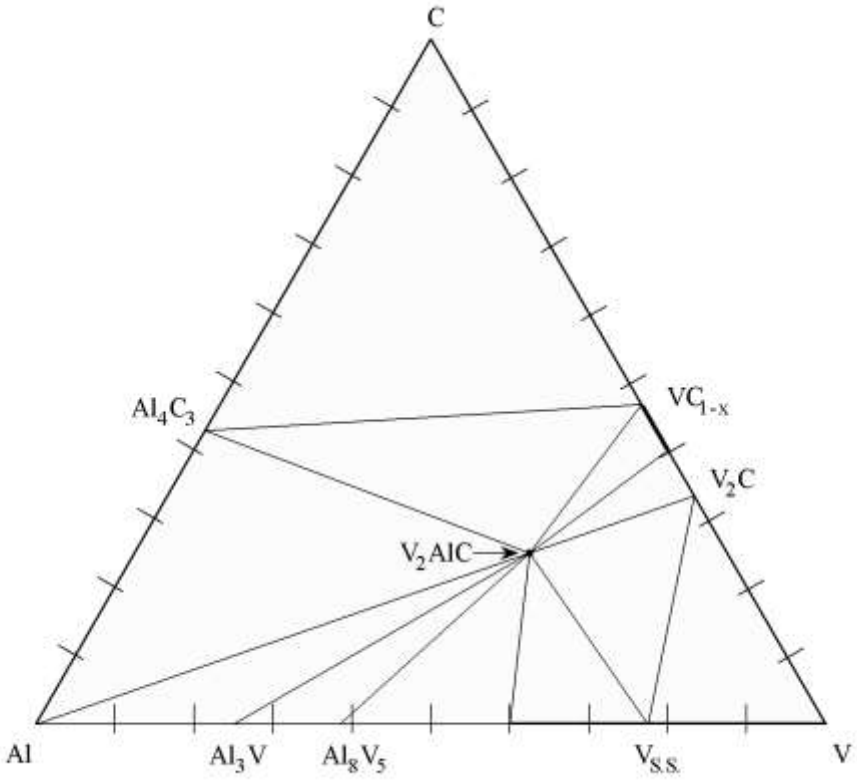

Figure 7. Isothermal ternary diagram at 1000°C of the Al-V-C system as reported by Schuster, et al [30].

Chapter 4.
Materials and Procedures

4.1. Materials

4.1.1. Al-Ti-B-C composites

Pure Al (99+ %, Alfa Aesar, Ward Hill, MA), Al 2024 (Alfa Aesar, Ward Hill, MA) and Al 6061 (Alfa Aesar, Ward Hill, MA) bar stock, and B_4C powder (99+ %, Alfa Aesar, Ward Hill, MA) with an average particle size < 10 μm was used for this work. Table 2 shows the range in chemical composition of each Al alloy as determined by x-ray fluorescence spectroscopy, XRF, (Niton XL3t, Thermo Scientific, USA). Five measurements were made from each alloy and the minimum and maximum values were recorded for each element. Commercial -325 mesh Ti_2AlC powders were obtained (Kanthal, Sweden). It is worth noting here that Ti_3AlC_2 is an impurity phase found in these powders (≈ 17 wt. % from Rietveld analysis).

Table 2. The range in chemical composition of Al alloys as determined by XRF.

Alloy	Element	Composition, % (Mass/Mass)	
		min	max
Pure	Al	99.006	99.692
	Ti	<LOD	0.094
	Cr	0.203	0.276
	Fe	0.043	0.47
	Cu	<LOD	0.016
	Zn	0.016	0.023
6061	Al	96.5	98.249
	Mg	<LOD	1.648
	Si	0.62	0.714
	Fe	0.294	0.408
	Cr	0.235	0.391
	Cu	0.189	0.26
	Ti	0.021	0.113
	Mn	0.053	0.101

Table 2 continued			
	Zn	0.023	0.033
	Sn	0.008	0.013
	Pb	0.003	0.006
2024	Al	80.77	94.27
	Cu	3.64	14.79
	Mg	<LOD	3.02
	Mn	0.7	2.11
	Cr	0.218	0.898
	Fe	0.169	0.583
	Zn	0.133	0.535
	Si	<LOD	0.477
	Ti	0.024	0.098
	V	<LOD	0.08
	Zr	0.005	0.043
	Ni	0.02	0.026
	Pb	<LOD	0.008
	Bi	<LOD	0.005

Range of observed alloy compositions. <LOD signifies below limit of detection.

4.1.2. Al-V-C composites

Pure aluminum (99.5%, -325 mesh, Alfa Aesar, Ward Hill, MA), vanadium (99.5%, -325 mesh, Alfa Aesar, Ward Hill, MA) and carbon (graphite, 99%, -325 mesh, Alfa Aesar, Ward Hill, MA) powders were used in the synthesis of Al-V-C composites.

4.2. Processing of Al-Ti-B-C composites

4.2.1. Preparation of carbide preforms

Two composites were fabricated starting with Al, Ti_2AlC, and B_4C. The first composite, henceforth referred to as BR, was more boron rich, having the Al:Ti:B:C molar ratio, calculated from Rietveld analysis of equilibrated microstructures (Appendix A1), of 3.3:1.1:2.5:0.5. The second composite, henceforth referred to as TiR, was more

Ti-rich and the Al:Ti:B:C molar ratios in this case – again calculated from Rietveld analysis (Appendix A2) – were 3.4:1.1:1.3:0.7.

The Ti_2AlC/B_4C powders were mixed in the molar ratios of 4.5:5 and 7:4 for the BR and TiR composites, respectively. These ratios correspond to roughly 50/50 vol. % and 75/25 vol. % ratios of Ti_2AlC/B_4C for the BR and TiR composites, respectively. The mixed powders were ball milled for 24 h with yttria stabilized zirconia grinding media, cold pressed in a steel mold - to a load corresponding to a stress of 50 MPa - to form rectangular ≈ 47 vol. % porous preforms (Table 3). The preform densities were 1.76 and 1.98 g/cm^3 for the BR and TiR preforms, respectively. Component densities were assumed to be 4.11 g/cm^3 for Ti_2AlC and 2.52 g/cm^3 for B_4C. No impurities or non-stoichiometry were considered.

Table 3. Dimensions of BR and TiR ceramic preforms after cold pressing to 50 MPa.

Composition, vol.% Ti_2AlC/B_4C	Post cold-pressed dimensions				
	width, mm	heigth, mm	length, mm	mass, g	density, %
50/50	12.5	6.6	69.4	10.43	55.27
50/50	12.7	6.1	69.4	9.47	53.12
75/25	12.8	8.1	69.3	13.13	53.4

4.2.2. Pressureless melt infiltration

The preforms were placed in alumina crucibles (AdValue Technology, Tucson, AZ), which were lined with graphite foil to avoid reactions with the crucible. Appropriately sized pieces of the Al alloy (pure, 2024, or 6061) were placed on top of the preform and the assembly was placed in an alumina tube furnace and heated at a rate of

10 °C/min to 900, 950, 1000, or 1050 °C and allowed to soak for 0.5 h before furnace cooling to room temperature, RT (Fig. 8). All experiments were carried out under flowing argon, Ar, gas at atmospheric pressure. The samples infiltrated with pure Al at 1000 °C were cut in half and one half was further annealed at 1000 °C for 10 h, again under flowing Ar.

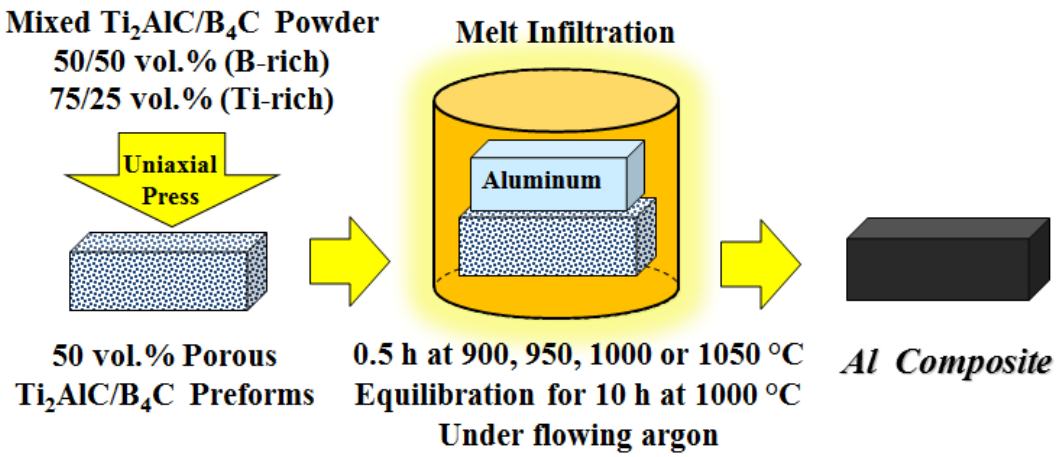

Figure 8. Pressureless melt infiltration technique for synthesizing Al-Ti-B-C composites.

4.2.3. Microstructure characterization

After cross-sectioning, mounting, and polishing (1200 grit) the microstructures were imaged using a SEM (Zeiss Supra 50VP, Germany) equipped with an energy-dispersive spectroscope (EDS) (Oxford Inca X-Sight, Oxfordshire, UK). Image analysis was undertaken using MATLAB (The MathWorks, Inc., Natick, MA) on select backscatter electron SEM micrographs to estimate the volume fractions of the various phases.

Powders for XRD were obtained by drilling the composites with a carbide drill bit and analyzed using a X-ray diffractometer (Rikagu Smartlab, Japan). The angular step was set to 0.02° over the 2θ = 5° – 80° range, with a hold time of 0.5 s and 2 s for 0.5 h infiltration and equilibration experiments, respectively. Scans were made through a 10x10 mm^2 window slit using Cu Kα radiation (40 KV and 30 mA).

To verify the presence of Al_4C_3, additional careful powder XRD was conducted on the equilibrium samples of both compositions. Powder was prepared immediately prior to running the XRD patterns. An angular step of 0.02° was set over the range 2θ = 30° – 33° and 2θ = 39.5° – 40.5°, with a hold time of 7 s. The slit and radiation conditions were the same as above. The hold time was extended here to enhance the intensity of the various peaks.

Rietveld refinements of the XRD patterns of the equilibrated samples were conducted using *FullProf* [55]. Refined parameters were: six background parameters, lattice parameters of all phases, scale factors from which relative phase fractions are evaluated, and *X* profile parameters for peak width.

4.2.4. Microhardness measurements

Vickers microhardness measurements were made using a Vickers hardness indenter (LECO Corp., St. Joseph, MI) under a 4.9 N force with a 10 s dwell period. Ten indentations were made. These measurements were averaged and standard deviations were found for each composite sample.

4.3. Processing of Al-V-C composites

4.2.2. Preparation of Al-MAX composites

Two composites were fabricated starting with elemental powders. The first composite, henceforth referred to as AlR, was more aluminum rich, having a nominal Al:V:C molar ratio of 9.8:2.0:1.0. The second composite, henceforth referred to as VR, was more vanadium rich, having the nominal Al:V:C molar ratio 3.9:2.0:1.0. These compositions were chosen so that *in situ* formation of V_2AlC would produce MMCs having ≈25 vol. % V_2AlC reinforcement and ≈50 vol. % V_2AlC reinforcement in the AlR and VR samples, respectively.

The mixed powders were ball milled for 16 h with yttria stabilized zirconia grinding media; approximately 10 g of each mixture was cold pressed in a steel mold (6.1 x 12.7 mm^2) - to a load corresponding to a stress of 200 MPa - to form rectangular preforms, which were then divided into 5 equal pieces (≈ 2 g each). The preforms were placed in alumina crucibles (AdValue Technology, Tucson, AZ) and heated at a rate of 10 °C/min to 1000 °C and allowed to soak for 0.5, 2.5 or 10 h. One sample of each composition, with a soaking time of 10 h, was allowed to furnace cool to room temperature. Other samples were quenched in a water bath. All experiments were carried out under flowing argon, Ar, gas at atmospheric pressure.

Relative density was measured using the Archimedes method. It was assumed that the volume fractions of V_2AlC and Al were 25/75 vol.% and 50/50 vol.% for the AlR and VR samples, respectively. The constituent densities used were 4.81 g/cm^3 for V_2AlC and 2.70 g/cm^3 for Al. This approximation was validated after Rietveld refinements

(Appendix A3 and A4) provided accurate volume fractions. The change in relative density after accounting for impurities was negligible.

4.3.2. Preparation of a carbon rich sample

In order to confirm the Al-Al_4C_3-V_2AlC equilibrium phase relations of the Al-V-C ternary phase diagram and to emphasize the presence of Al_4C_3 in the XRD spectra, a C-rich stoichiometry was chosen to have the nominal Al:V:C molar ratio 8.0:1.0:3.0. This sample, henceforth referred to as CR, was prepared in an identical manner as the AlR and VR samples. The sample was soaked at 1000 °C for 10 h before being water quenched.

4.3.3. Preparation of samples for differential scanning calorimetry

In order to evaluate the stability of V_2AlC with Al below 1000 °C, two samples were prepared to be analyzed using DSC. The powders were mixed, pressed and heated in the same manner as the other experiments. One sample, henceforth referred to as DSC-FC, was allowed to furnace cool after soaking at 1000 °C for 10 h and the other sample, henceforth referred to as DSC-WQ, was water quenched. The composition was determined from Rietveld analysis after equilibration at 800 (Appendix A5) and 1000 °C (Appendix A6), where it was determined that the Al:V:C molar ratio was between 13.5:3.0:1.0 and 15.3:2.6:1.0. All points within this range are contained within the same equilibrium triangle at both 800 and 1000 °C.

4.3.4. Microstructure characterization

Powders for XRD were obtained by drilling the composites with a carbide drill bit and analyzed using a X-ray diffractometer (Rikagu Smartlab, Japan). The angular step

was set to 0.02° over the 2θ = 5° – 80° range, with a hold time of 0.5 s for the furnace cooled AlR and VR samples, as well as for the CR sample. For the quenched AlR and VR samples the angular step was set to 0.02° over the 2θ = 20° – 50° range, with a hold time of 1.5 s. The DSC-FC and DSC-WQ samples used the same angular step over the 2θ = 20° – 80° range, with a hold time of 1.0 s. Scans were made through a 10x10 mm^2 window slit using Cu Kα radiation (40 KV and 30 mA). Jade XRD pattern recognition software (Materials Data, Inc., Livermore, CA.) was used to analyze the XRD results. Rietveld refinements of some XRD patterns were conducted using *FullProf* [55]. Refined parameters were: six background parameters, lattice parameters of all phases, scale factors from which relative phase fractions are evaluated, and *X* profile parameters for peak width.

After cross-sectioning, mounting, and polishing (1200 grit), the microstructures of some composites were imaged using a SEM (Zeiss Supra 50VP, Germany) equipped with an energy-dispersive spectroscope (EDS) (Oxford Inca X-Sight, Oxfordshire, UK). EDS was carried out at a working distance of 12 mm and an accelerating voltage of 15 kV.

4.3.5. Characterization by differential scanning calorimetry

Approximately 225 mg of the DSC-WQ sample and 228 mg of the DSC-FC sample were analyzed using a DSC (SDT Q600, TA Instruments, New Castle, DE). The heating/cooling rate was 10 °C/min over the temperature range 100 – 1000 °C. Data points were collected every 0.6 s. In parallel to the DSC investigation, approximately 2 g of the DSC-WQ sample was heated under flowing Ar in the tube furnace at a heating rate

of 10 °C/min to 800 °C, allowed to soak for 10 h and was then water quenched. The same procedure was also performed at a soaking temperature of 1000 °C.

Chapter 5.
Characterization of Al-Ti-B-C composites

5.1. Results of equilibration experiments

5.1.1. X-ray diffraction of equilibrated samples

Table 4 summarizes the results obtained in this work. Phase identification, from both XRD and SEM/EDS, revealed that neither Ti_2AlC nor B_4C was an equilibrium phase in either composite. After annealing at 1000 °C for 10 h, the phases present in the BR sample, as determined by XRD were: Al, TiB_2, Al_4C_3 and Al_3BC (Table 4 and Fig. 9a); those present in the TiR sample were: Al, TiB_2, Al_4C_3, and TiC (Table 4 and Fig. 9b). In other words, Al, TiB_2, and Al_4C_3 were equilibrium phases in both compositions. For the BR and TiR compositions, all diffraction peaks were accounted for, with Rietveld χ^2 values of 5.12 and 8.60, respectively.

The presence of Al_4C_3 was not apparent at first. The low intensity of its diffraction peaks were difficult to distinguish from background noise in diffraction patterns acquired with 0.5 s hold times. Further XRD patterns of the equilibration samples, using a 2 s hold time (Fig. 9), provided confidence that Al_4C_3 diffraction peaks were present. XRD patterns obtained with a hold time of 7 s however, confirmed the presence of this phase in the equilibrated samples (insets of Fig. 9).

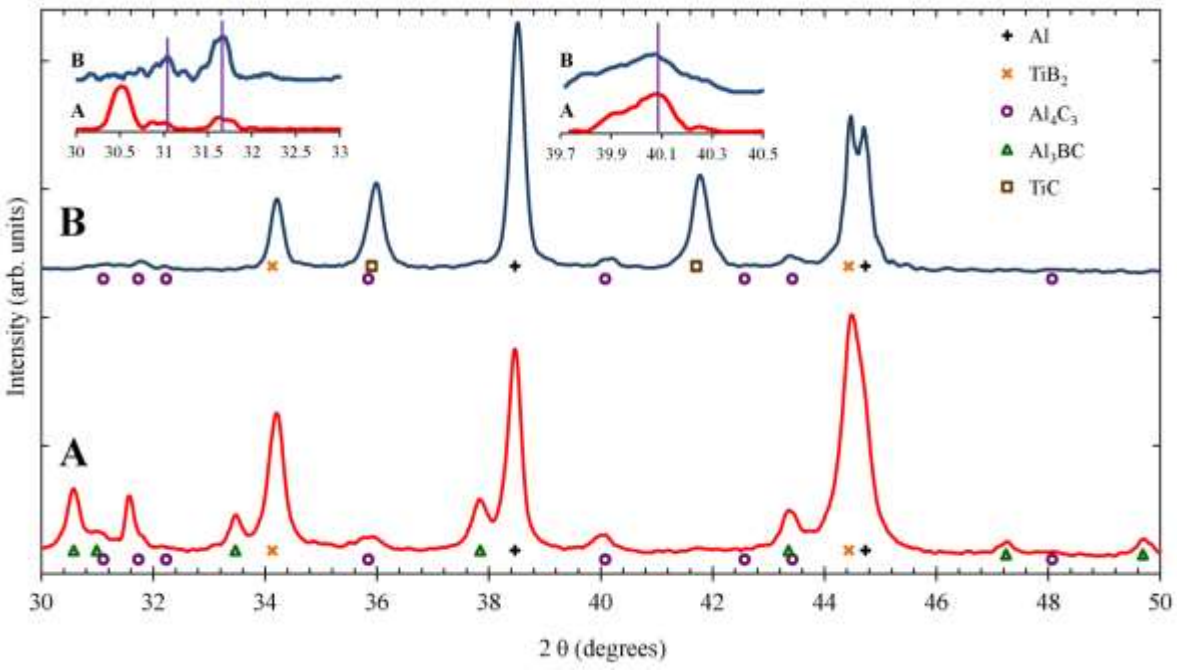

Figure 9. Typical XRD patterns for, A) BR and, B) TiR composites after equilibrating at 1000 °C for 10 h under flowing Ar. In both systems, Al, TiB_2, and Al_4C_3 were equilibrium phases. The presence of Al_4C_3 in both composites was confirmed by additional investigations (marked by vertical lines in the insets).

Table 4 The observed phases from each experiment are reported with their relative increase or decrease in amount noted, if applicable, and calculated volume fractions, if available.

Soaking Time	Composite	Temperature	Major Phases (Relative increase ↑ / Decrease ↓)				Minor Phases (Relative increase ↑ / Decrease ↓)		
Results from Image Analysis									
0.5 h	BR	900	Al	TiB_2	Al_3BC	Al_4C_3 (↑)	B_4C (5.4 vol. %)	TiC	AlB_2
		950	Al (↓)	TiB_2 (↑)	Al_3BC (↑)	Al_4C_3 (↑)	B_4C (5.1 vol. %)	TiC (↓)	AlB_2 (↓)
		1050	Al (↓)	TiB_2 (↑)	Al_3BC (↑)	Al_4C_3 (↑)	B_4C (2.1 vol. %)	TiC (↓)	AlB_2 (↓)
	TiR	900	Al	$TiAl_3$	TiC	TiB_2	Al_4C_3	B_4C (9.6 vol. %)	Ti_3AlC_2 (5.3 vol. %)
		950	Al (↑)	Al_3BC	TiB_2 (↑)	TiC (↑)	Al_4C_3 (↑)	B_4C (4.7 vol. %)	$TiAl_3$ (↓)
		1050	Al (↑)	TiB_2 (↑)	TiC (↑)		Al_4C_3 (↑)	B_4C (< 1 vol. %)	
0.5 h	BR	1000	Al	TiB_2	Al_3BC	Al_4C_3	B_4C (2.5 vol. %)	TiC	AlB_2
10 h		1000	Al	TiB_2	Al_3BC	Al_4C_3	B_4C (< 1 vol. %)		
0.5 h	TiR	1000	Al	TiB_2	TiC	Al_4C_3	B_4C (< 1 vol. %)		
10 h		1000	Al	TiB_2	TiC	Al_4C_3	B_4C (< 1 vol. %)		
Results from Rietveld Analysis									
10 h	BR	1000	Al	TiB_2	Al_3BC	Al_4C_3			
			32.8 wt. %	44.6 wt. %	15.9 wt. %	7.1 wt. %			
			39.7 vol. %	32.2 vol. %	18.3 vol. %	9.8 vol. %			
	TiR	1000	Al	TiB_2	TiC	Al_4C_3			
			49.8 wt. %	26.2 wt. %	17.4 wt. %	6.6 wt. %			
			60.4 vol. %	18.9 vol. %	11.5 vol. %	9.1 vol. %			

5.1.2. Microstructures of equilibrated composites

The BR composite soaked at 1000 °C for 0.5 h seemed to exhibit a homogeneous microstructure, with relatively large B_4C grains (black areas in Fig. 10a) remaining. Image analysis estimated the unreacted B_4C fraction to be ≈ 2.5 vol. %. In addition to the equilibrium phases present in the BR composite, traces of AlB_2 and TiC could be found within the Al matrix when viewed at high magnification in the SEM (Fig. 10b). When the microstructure of the sample infiltrated for 0.5 h at 1000°C was compared with the one held for 10 h at the same temperature (compare Fig. 10a and c, respectively) it is clear that:

i) Al-containing phases, primarily Al_3BC, replaces the B_4C; ii) the volume fraction of the Al/TiB_2 regions (light grey contrast in Figs. 10a and c) increased at the expense of the Al/Al_3BC regions (mid grey contrast) as the system tended towards equilibrium. The B_4C volume fraction after the 10 h anneal was estimated to be < 1 vol. %. Aside from the remaining B_4C, no other non-equilibrium phases could be identified from microscopy (Fig. 10d); iii) the TiB_2 grains in the Al matrix were observed to notably coarsen with the prolonged annealing, growing from an estimated average diameter of < 200 nm to > 500 nm (Figs. 10b and d); iv) TiB_2 grains are found in the Al matrix, but not in the same regions as the Al_4C_3 or Al_3BC phases (Fig. 10d).

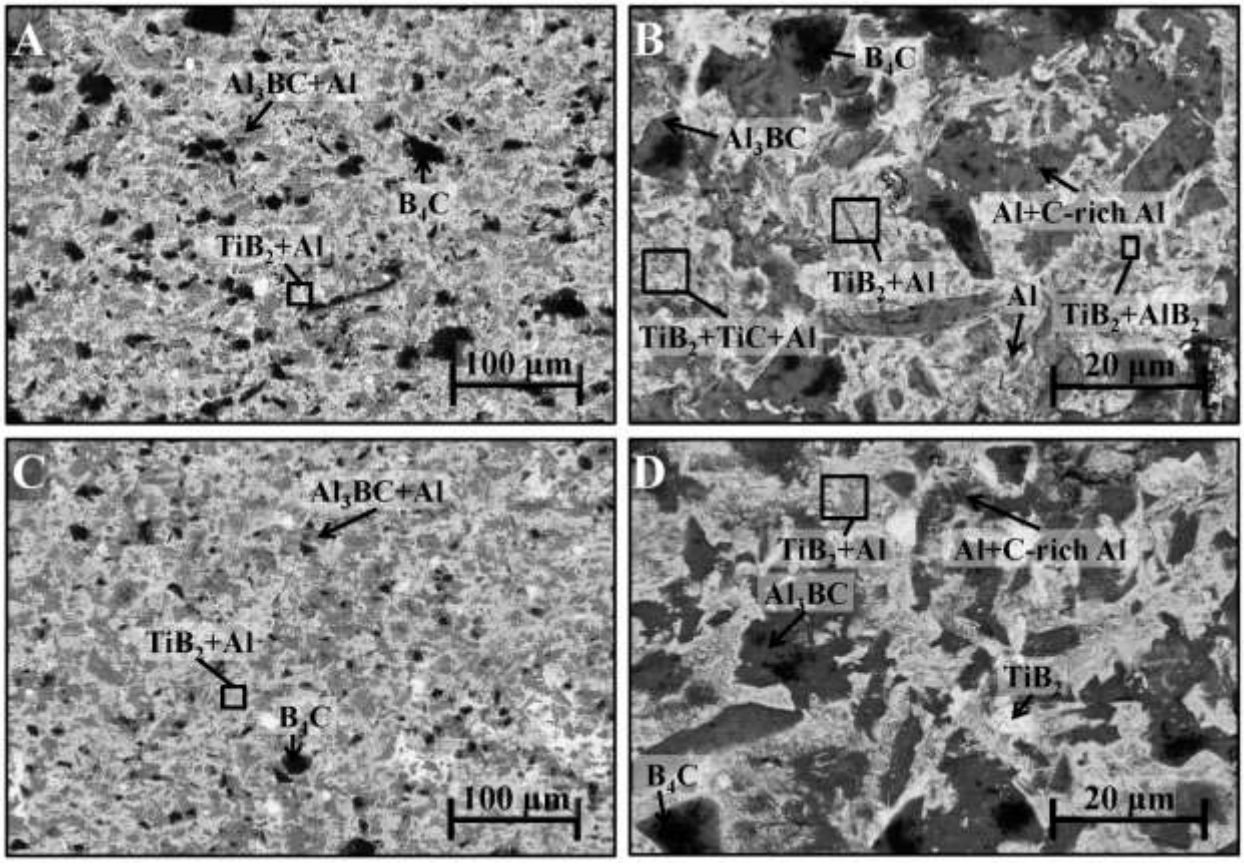

Figure 10. Backscattered electrons SEM images of BR samples fabricated at 1000 °C. A) Low magnification image of sample annealed for 0.5 h. Large unreacted B_4C grains (black) can be found amongst Al_3BC/Al (mid grey) and TiB_2/Al (light grey) regions. B) Higher magnification image of A demonstrating the presence of two distinct regions. Note the small grains of TiB_2 dispersed in Al, whereas Al_3BC grains tend to be much larger. C) Low magnification image of sample annealed for 10 h. The decreased fraction of remaining B_4C grains (black) corresponds to an increase in the TiB_2/Al (light grey) regions. D) Higher magnification image of C demonstrating the increased grain size of TiB_2 grains in the Al matrix.

The presence of Al_4C_3 was not directly observed in the SEM in any of the investigated samples. However, since Al_4C_3 is hygroscopic and dissolves in water at room temperature [56] it is reasonable to assume that it dissolved during the water-based polishing procedure. Note that EDS analysis of cross-sectional SEM micrographs clearly show that some Al-rich regions were comprised of pure Al; others were found to contain

substantial amounts of C with Al/C ratios that varied between 1.0 and 1.9. It is hereby acknowledged that there are several explanations for why C may be detected in some Al regions and not others, including, the presence of C-containing phases below the surface, but within the excitation volume of the EDS. Nevertheless, since Al_4C_3 peaks were observed – and twice confirmed – in the XRD patterns (insets in Fig. 9), there is proof that it exists in the microstructures. Another possibility is that the Al_4C_3 phase for some reason dissociated into C-rich Al regions. Therefore, the C-rich Al regions are tentatively labeled as Al_4C_3 in the micrographs. These comments notwithstanding, more work is needed to understand what happens to the Al_4C_3 phase.

A relatively homogeneous microstructure was also obtained for the TiR composite after soaking at 1000 °C for 0.5 h (Fig. 11a). Larger TiC grains were found surrounded by an Al matrix; small grains of TiB_2 and TiC were distributed throughout. With the exception of a few remaining B_4C grains – accounting for approximately < 1 vol. % – and the possible formation of Al_3BC at the B_4C/Al interfaces, the only phases identified were – Al, TiC, TiB_2 and C-rich Al areas (Fig. 11b). After annealing for 10 h, the microstructure remained largely unchanged (Fig. 11c). Trace amounts of B_4C (< 0.5 vol. %) were still present after the 10 h anneal (Fig. 11d). In this case, no significant grain coarsening was observed for the small (< 1 μm) TiB_2 and TiC grains.

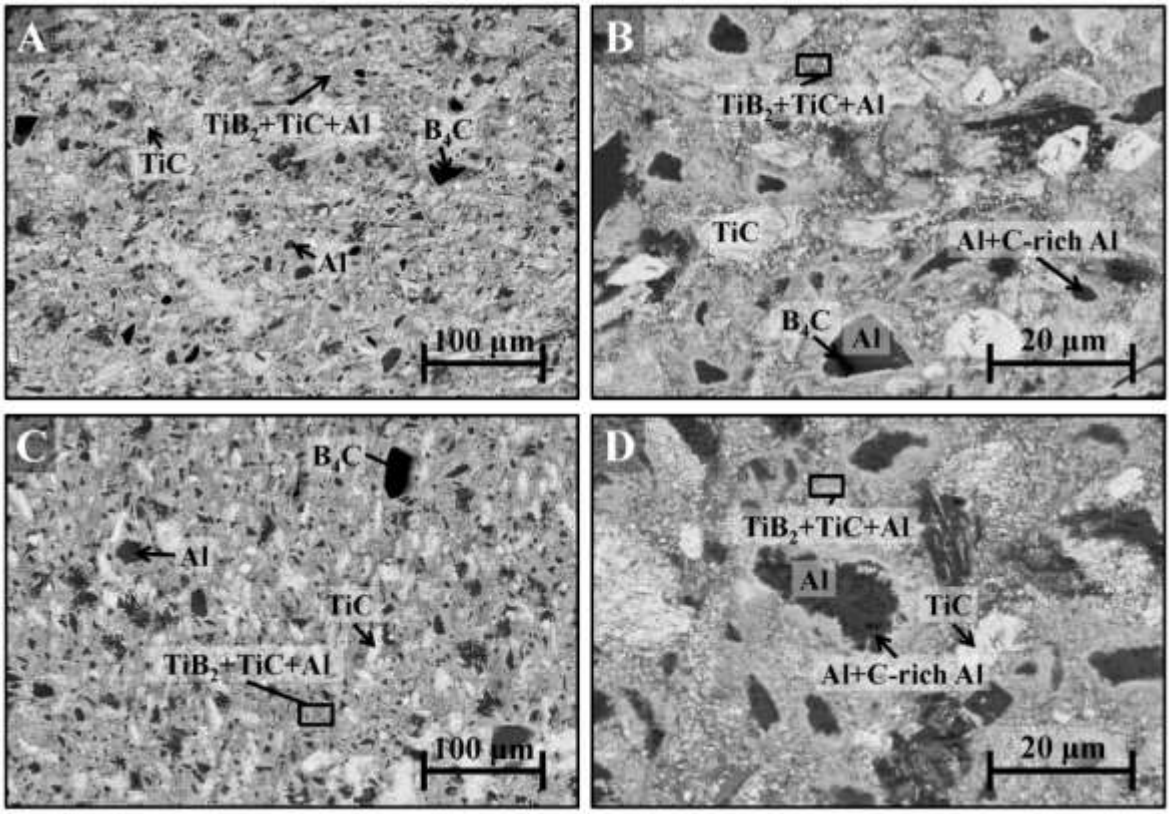

Figure 11. Backscattered electrons SEM images of TiR sample annealed at 1000 °C. A) Low magnification image demonstrating homogeneous microstructure after 0.5 h anneal time. Some grains of B_4C (black) can be found remaining. B) Higher magnification image of A showing small TiC/TiB_2 grains dispersed in the Al matrix. C) Low magnification image of sample annealed for 10 h. D) Higher magnification image of C demonstrating similar grain dispersion to B.

5.2. Results of samples melt infiltrated for 0.5 h.

5.2.1. X-ray diffraction of reaction products

Complete infiltration of both BR and TiR composite preforms was observed after 0.5 h over the 900-1050 °C temperature range. The most intense XRD peaks corresponded to those belonging to Al, Al_3BC and TiB_2 (Fig. 12). Peaks associated with Al_4C_3, were weak at all temperatures (Fig. 12). At 900 °C (Fig. 12a) peaks belonging to

B_4C at 2θ = 34.96°, were observed. At 950 °C and higher temperatures, no B_4C peaks were observed (Figs. 5b and c).

Additionally, the TiC peak intensities decreased with increasing infiltration temperatures (see peak at 2θ = 41.71° in Fig. 12). As AlB_2 shares its dominant XRD peaks with other phases, its presence was better ascertained by microscopy. The shoulder in the TiB_2 peak, at 2θ = 34.41°, may be the best diffraction evidence that the quantity of AlB_2 decreases with MI temperature, as this shoulder is no longer observed after MI at 1050 °C (Fig. 12c).

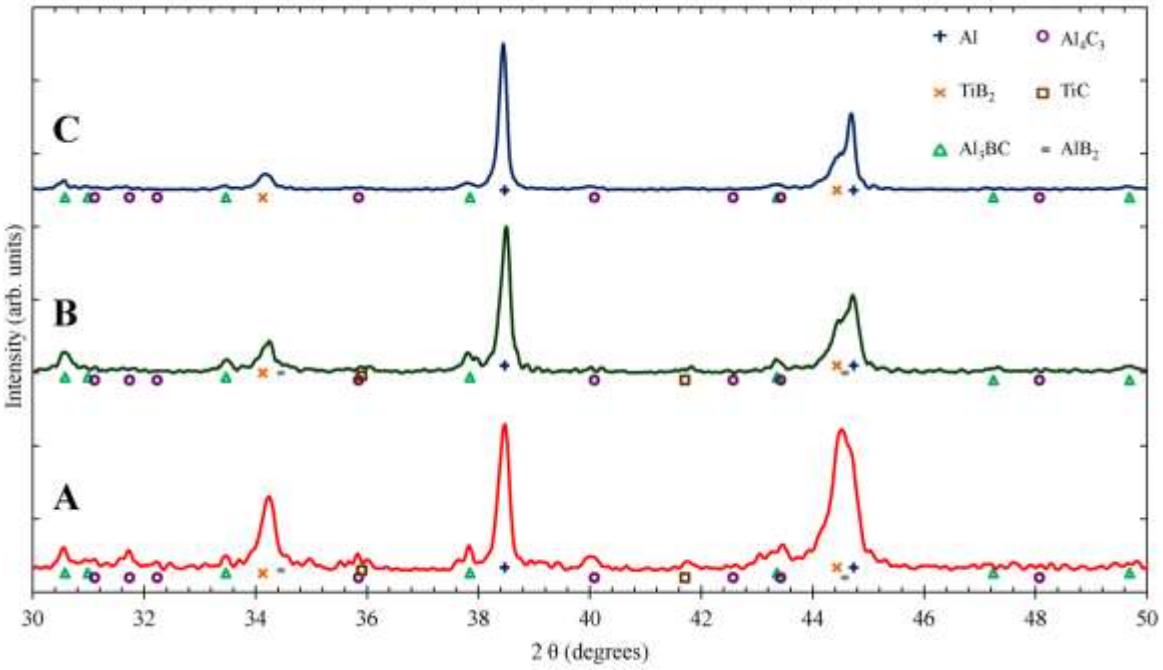

Figure 12. X-ray diffraction patterns for BR samples infiltrated and held at, A) 900, B) 950 and, C) 1050°C for 0.5 h.

For the TiR composite fabricated at 900 °C (Fig. 13a), prominent XRD peaks for Ti_3AlC_2 were found along with those for $TiAl_3$, TiC, and Al. However, by 950 °C peaks

associated with Ti_3AlC_2 disappeared, and the peak intensities associated with $TiAl_3$ were significantly decreased, while those of TiB_2 and Al_3BC were seen to emerge (Fig. 13b). At 1050 °C, the XRD patterns (Fig. 13c) clearly showed that the phases present were the same as those observed after 10 h at 1000 °C (Fig. 9b), viz. Al, TiB_2, TiC and Al_4C_3.

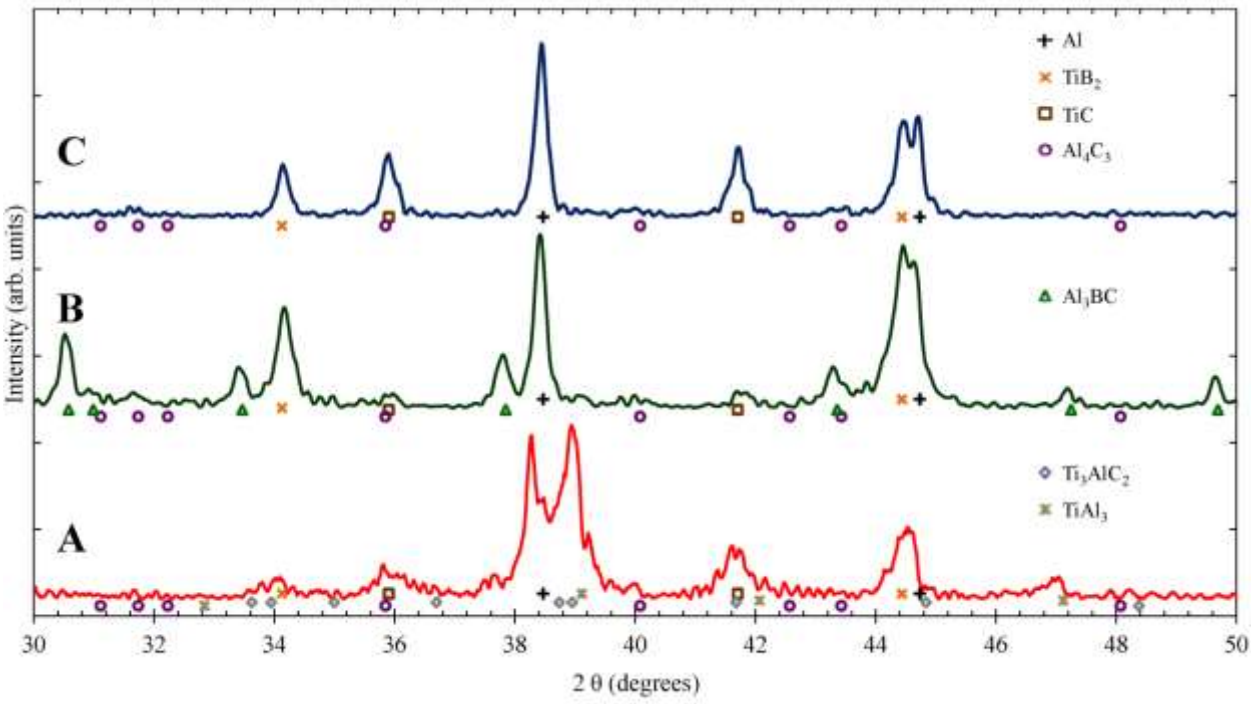

Figure 13. X-ray diffraction patterns for TiR samples infiltrated and held at, A) 900, B) 950 and, C) 1050°C for 0.5 h.

5.2.2. Microstructures of composites

Not surprisingly, the BR composite sample fabricated at 900 °C was the farthest from equilibrium, since it contained the largest content of the non-equilibrium phases, TiC and AlB_2 and B_4C (Table 4). Aside from the presence of these non-equilibrium phases, the BR composites infiltrated at 900 °C (Fig. 14a), 950 °C (Fig. 14c), and 1050 °C (Fig. 14e) were relatively homogeneous, with two distinct regions: The first consisted

of Al_3BC and the second TiB_2/TiC both in Al matrices (Figs. 14a, c and e). The differences between the two regions are best seen at higher magnification of the sample infiltrated at 1050 °C (Fig. 15). Note that C-rich Al regions were also found alongside Al_3BC in the Al matrix, but not in regions containing the Ti phases. The TiB_2/TiC regions also contained AlB_2 (Fig. 15). Because of their small grain size (< 1 μm diameter) it was not possible to estimate the volume fractions of these phases from image analysis. Note that, for similar reasons, it was difficult to precisely identify the composition of individual grains from EDS.

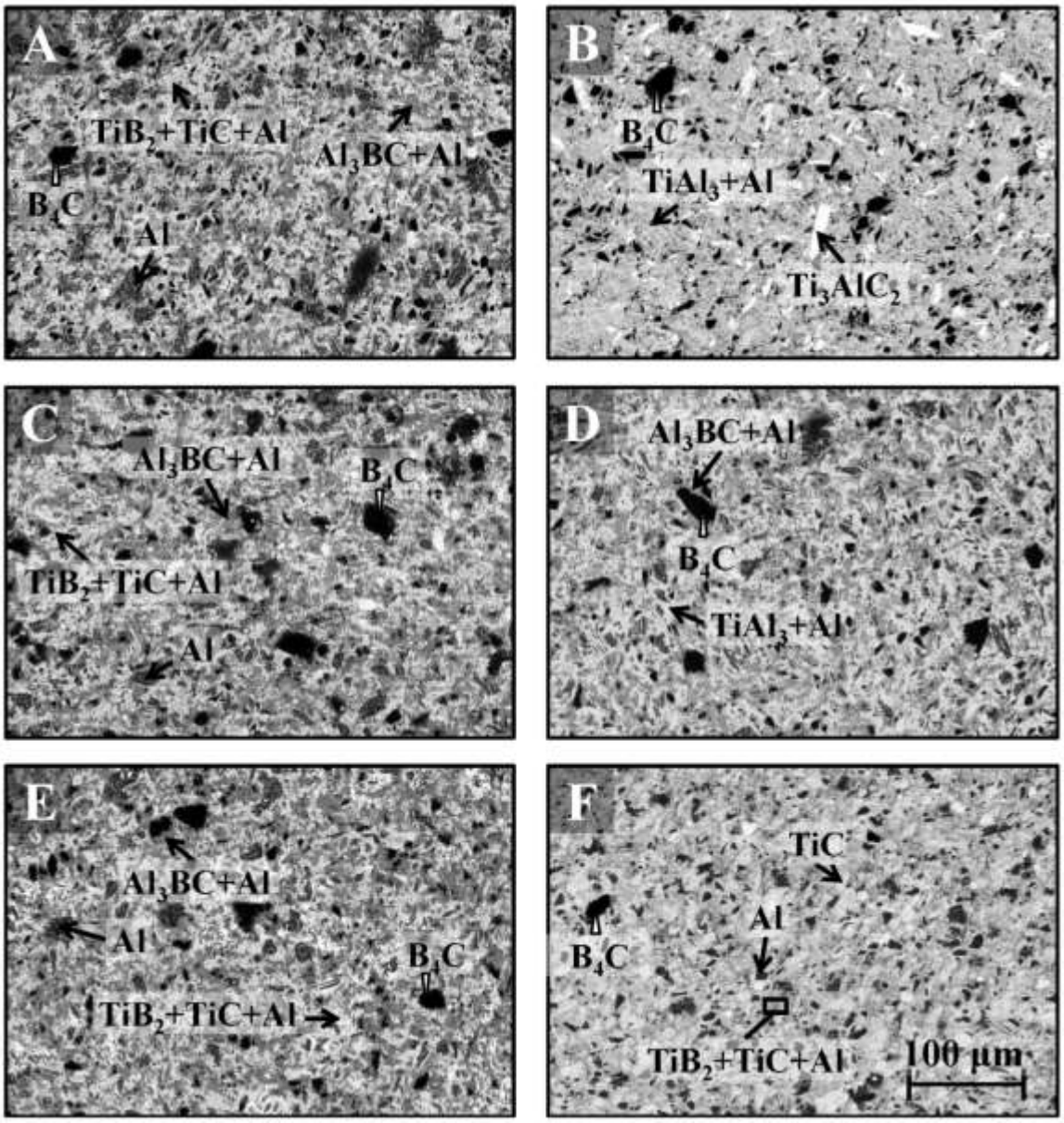

Figure 14. Backscattered electrons SEM images of BR (left) and TiR (right) infiltration experiments annealed for 0.5 h. A) BR sample processed at 900 °C demonstrating the highest fraction of unreacted B_4C (black). B) TiR sample processed at 900 °C demonstrating the presence of Ti_3AlC_2, with needle-like grain morphology, dispersed in a $TiAl_3$/Al matrix. C) BR sample processed at 950 °C. D) TiR sample processed at 950 °C. Ti_3AlC_2 disappears and Al_3BC appears as B_4C and $TiAl_3$ are consumed. E) BR sample processed at 1050 °C demonstrating no distinguishable microstructural changes from A. F) TiR sample processed at 1050 °C demonstrating a change in microstructure that is similar to the equilibrated sample (Fig. 11c).

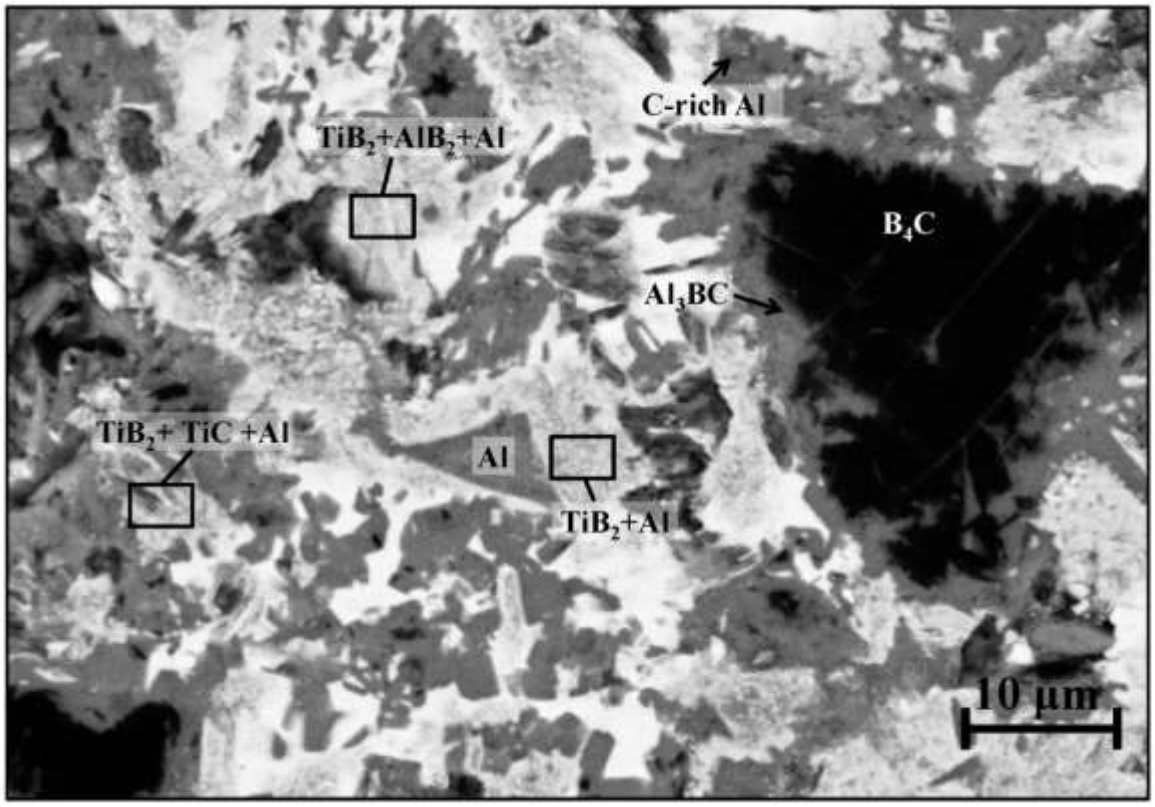

Figure 15. Backscattered electrons SEM image of BR sample infiltrated and held at 1050°C for 0.5 h.

After MI at 900 °C, needle-like grains of Ti_3AlC_2 could be seen dispersed throughout an $Al/TiAl_3$ matrix (Fig. 14b). From image analysis the Ti_3AlC_2 volume fraction was estimated to be ≈ 5.3 vol. %. This infiltration temperature also resulted in the largest volume fraction of unreacted B_4C (Table 4). Higher magnification SEM micrographs revealed that this composite was primarily (≈ 85 vol. %) $TiAl_3$, in equilibrium with Al and that little reaction had occurred with the B_4C phase (Fig. 9a).

Raising the infiltration temperature to 950 °C resulted in the disappearance of the Ti_3AlC_2 phase from both the XRD and SEM results (Fig. 13b and 7d). The microstructure at this temperature consisted of fine grains of TiB_2 and TiC contained in an $Al/TiAl_3$

matrix, with some unreacted B_4C grains remaining (Fig. 14d). The latter were surrounded by Al_3BC. The C-rich Al-containing regions were not found in regions of Ti-containing phases, but were only found in the vicinity of the Al and Al_3BC phases (Fig. 9b). After the 1050 °C infiltration, there was no trace of $TiAl_3$; the only phases remaining were TiC, TiB_2, Al and C-rich Al-containing regions, with trace amounts of B_4C (Fig. 14f).

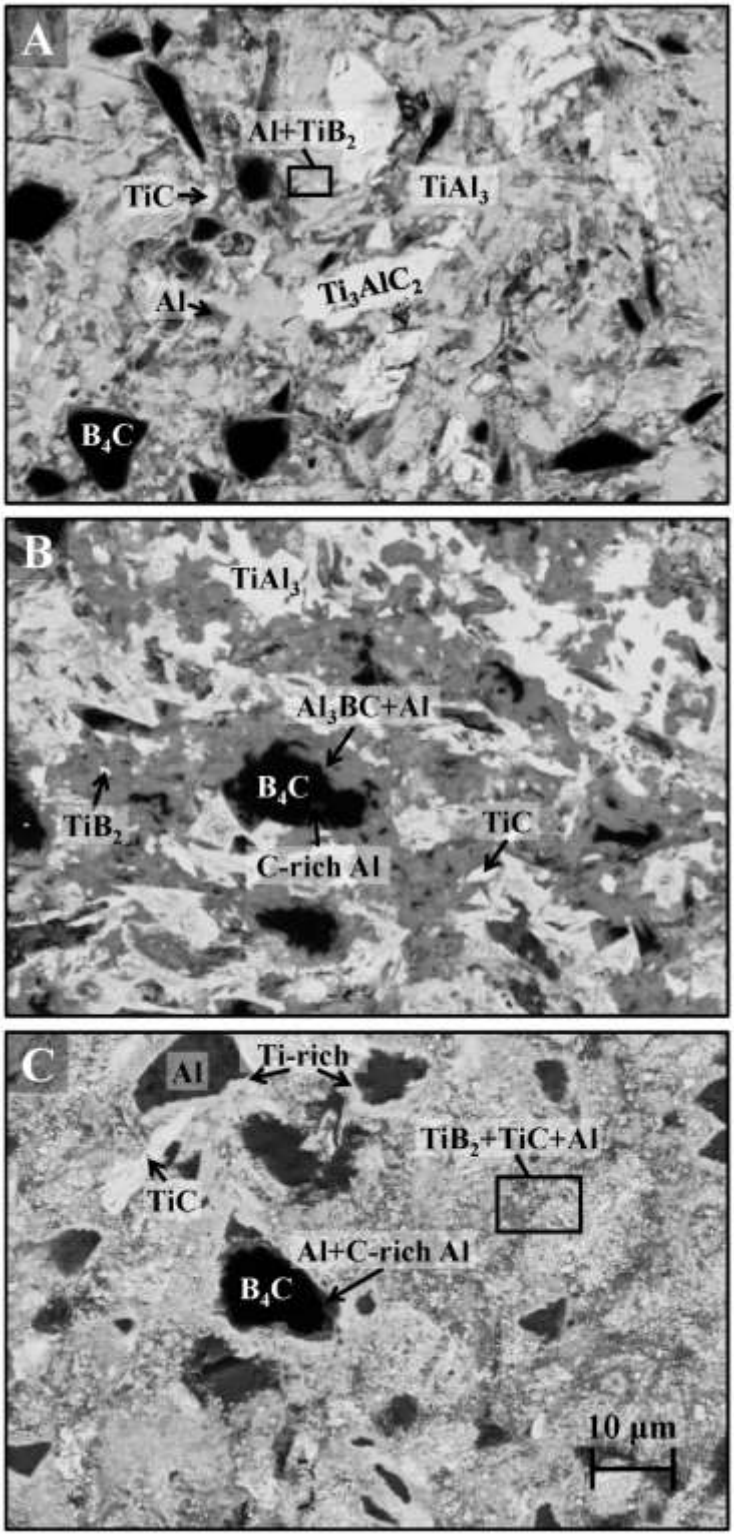

Figure 16. Backscattered electrons SEM image of Ti-rich infiltration experiment at (A) 900 °C, (B) 950 °C, and (C) 1050 °C for 0.5 h. Scale bar applies to all panels.

In contrast to the microstructures seen after MI at 900 °C (Fig. 16a) and 950 °C (Fig. 16b), the ones MI at 1000 °C (Fig. 11b) and 1050 °C (Fig. 16c) showed regions with evenly dispersed grains of TiC and TiB_2 in an Al matrix. The ternary Al_3BC was not found above 950 °C and the large B_4C grains were replaced by some C-containing Al matrix regions, surrounded by a ≈ 0.5 μm wide Ti-rich layer (Fig. 16c).

5.2.3. Composites infiltrated with Al alloys.

B-rich, BR, preforms infiltrated with Al 6061 and Al 2024 demonstrated similarities to the composites fabricated from pure Al. Complete infiltration was observed for each composite system at each temperature. For the BR-6061 system, the most intense XRD peaks corresponded to those belonging to Al, Al_3BC and TiB_2 (Fig. 17). Peaks associated with Al_4C_3, were weak at all temperatures (Fig. 17). At 900 °C (Fig. 17a) peaks belonging to B_4C were observed. At 950 °C and higher temperatures, no B_4C peaks were observed (Figs. 17b and c). The relative intensity of the TiB_2 peaks was seen to increase with increasing temperature (Fig. 17).

BR preforms infiltrated by Al 2024 alloy also demonstrated notable B_4C peaks in the XRD spectra at 900 °C (Fig. 18a). Again, no B_4C peaks were observed after infiltration at 950 or 1050 °C (Fig. 18b and c, respectively). It is also interesting to note the distinguished presence of AlB_2 at 900 °C, which is well reduced by 950 °C and undiscernible by 1050 °C (Fig. 18c). The Al_3BC and Al_4C_3 peaks at 1050 °C are not well distinguished from the background noise in the XRD pattern. No copper containing phases were apparent at any temperature.

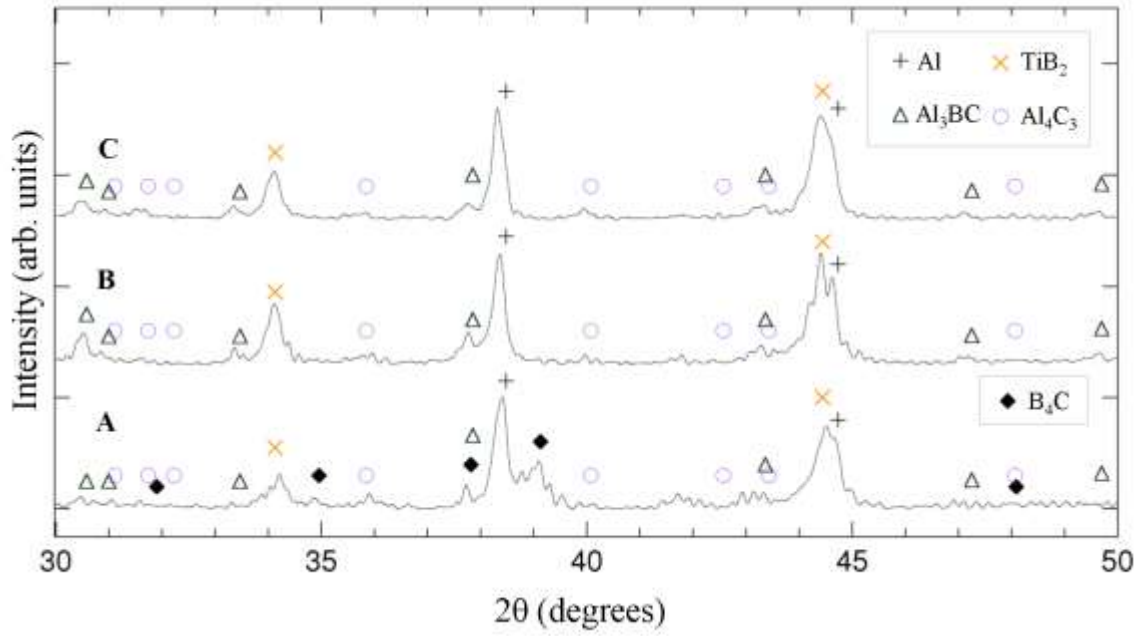

Figure 17. X-ray diffraction patterns for AlR samples infiltrated with Al-6061 and held at, A) 900, B) 950 and, C) 1050°C for 0.5 h.

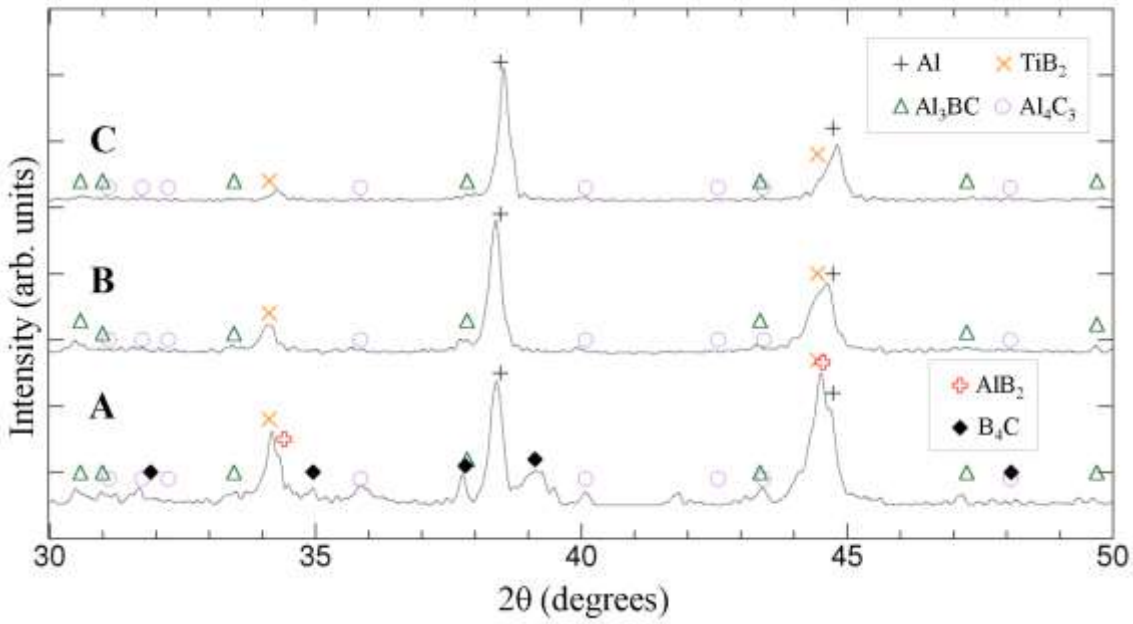

Figure 18. X-ray diffraction patterns for AlR samples infiltrated with Al-2024 and held at, A) 900, B) 950 and, C) 1050°C for 0.5 h.

The microstructures of the BR composites infiltrated with alloy 6061 (Figs. 19, 20 and 21) and 2024 (Figs. 22, 23 and 24) were visually similar, at their respective infiltration temperatures, to those observed for the composites fabricated with pure Al (Fig. 14a, c and e). In all cases B_4C grains (black contrast in Figures) were observed at each temperature, but decreased in number and size with increasing infiltration temperature. Again, two distinct regions were observed: Al with Al_3BC and Al with TiB_2 and TiC. The Al_3BC phase was found to be in the same vicinity as pure Al, and next to B_4C grains, but was not found with TiB_2 or TiC grains.

EDS investigations of the Al 6061 MMCs confirmed the XRD results. At 900 °C the composition was furthest from equilibrium (Fig. 17a and 19b), having the most B_4C and AlB_2 grains. At higher temperatures, Al, Al_3BC, and TiB_2 were identified as the primary phases, with some TiC (Fig. 20b and 21b). Similar conclusions were drawn from EDS investigations of the composites infiltrated with Al 2024. At 900 °C (Fig. 22) and 950 °C (Fig. 23) this composite was found to contain the non-equilibrium phases B_4C and AlB_2 that were identified from XRD. In this case, however, EDS demonstrated the presence of Al_3BC at 1050 °C (Fig. 24), even though the peak intensity was minimal in the XRD spectra (Fig. 18c). Lastly, while Al 2024 contains $\approx$ 5 wt. % Cu, and some Cu was detected using EDS, no specific Cu-rich grains could be identified.

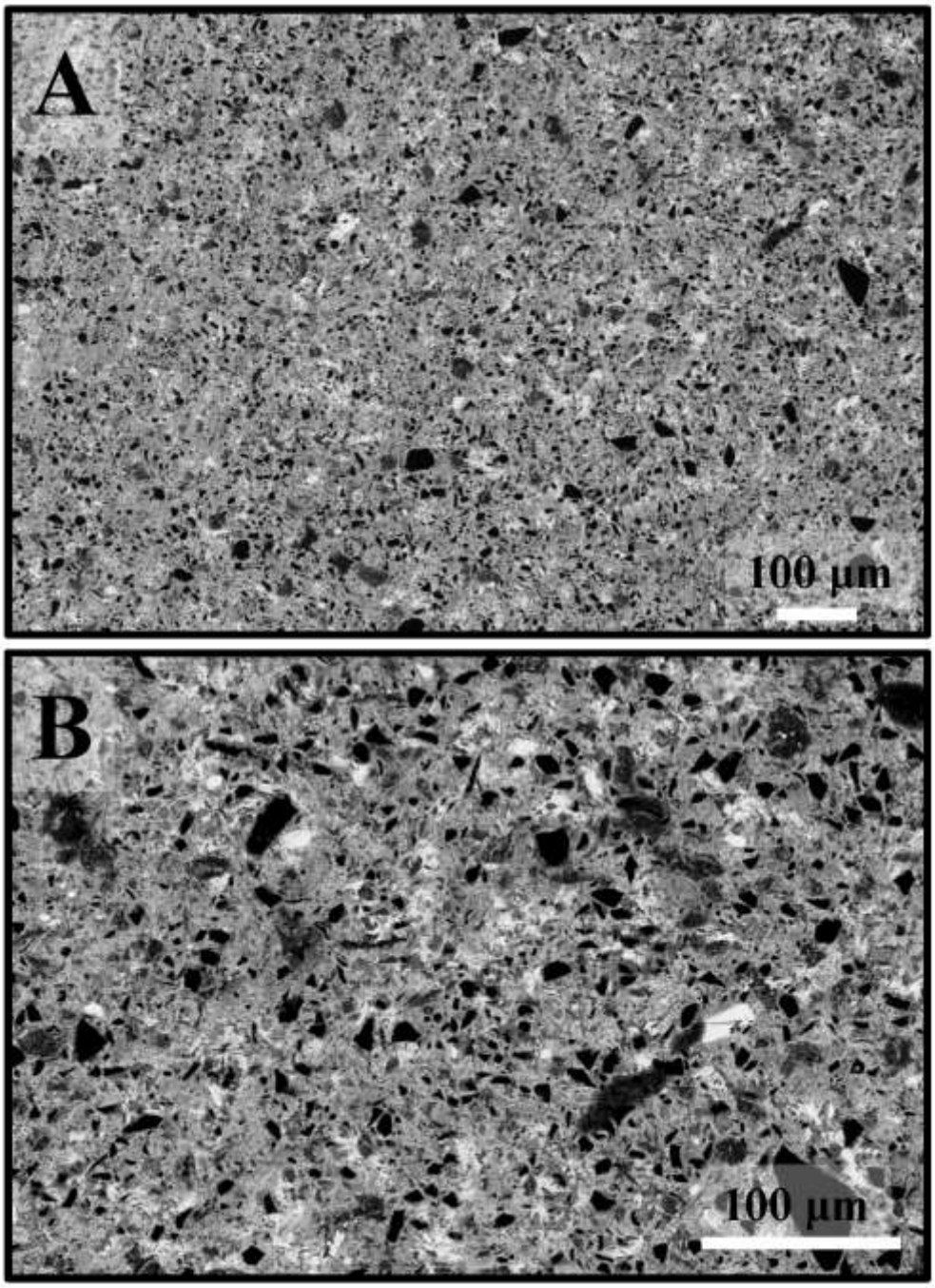

Figure 19. A) Low magnification and, B) higher magnification backscattered electrons SEM images of BR composite fabricated with Al 6061 at 900 °C.

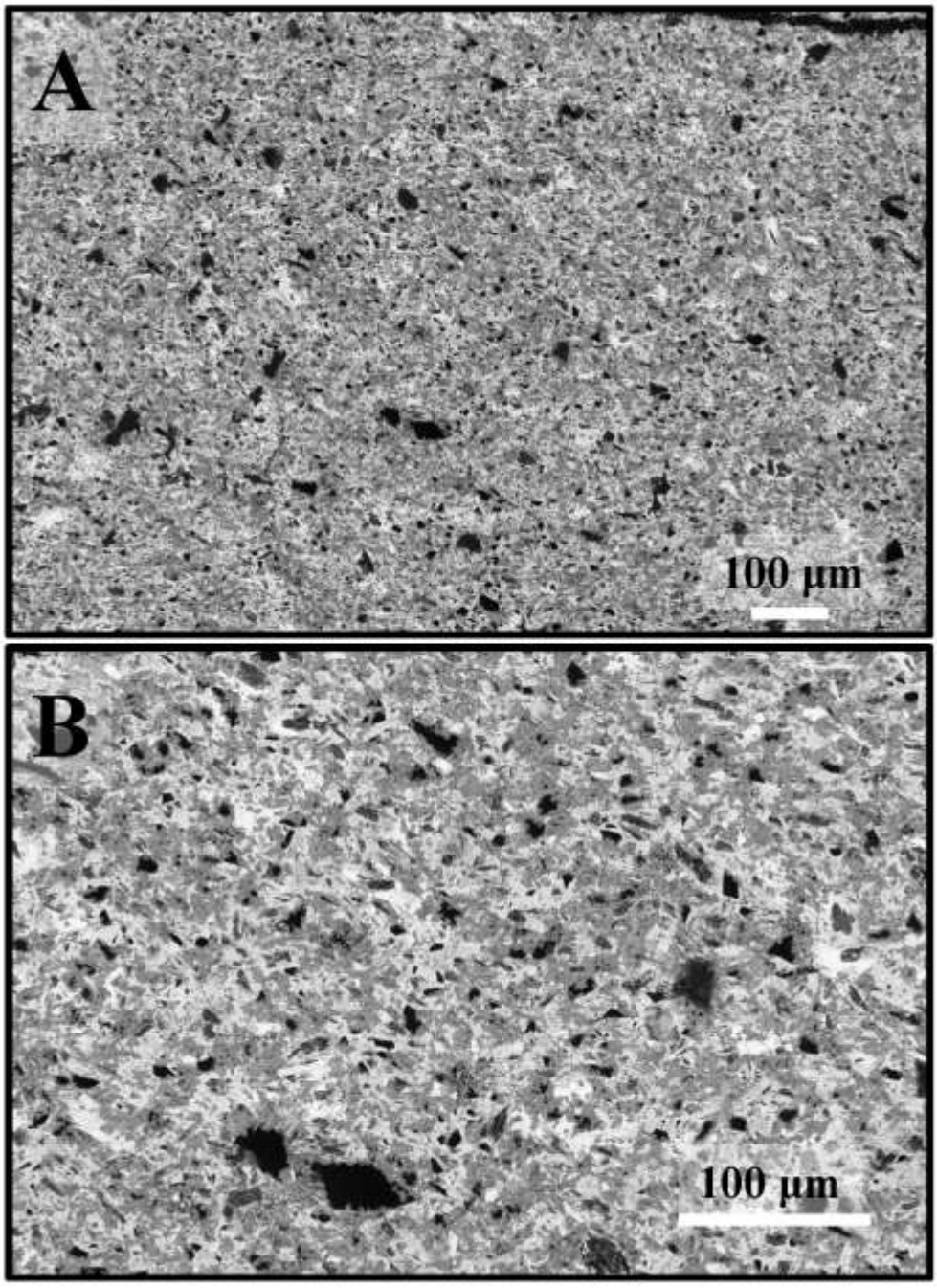

Figure 20. A) Low magnification and, B) higher magnification backscattered electrons SEM images of BR composite fabricated with Al 6061 at 950 °C.

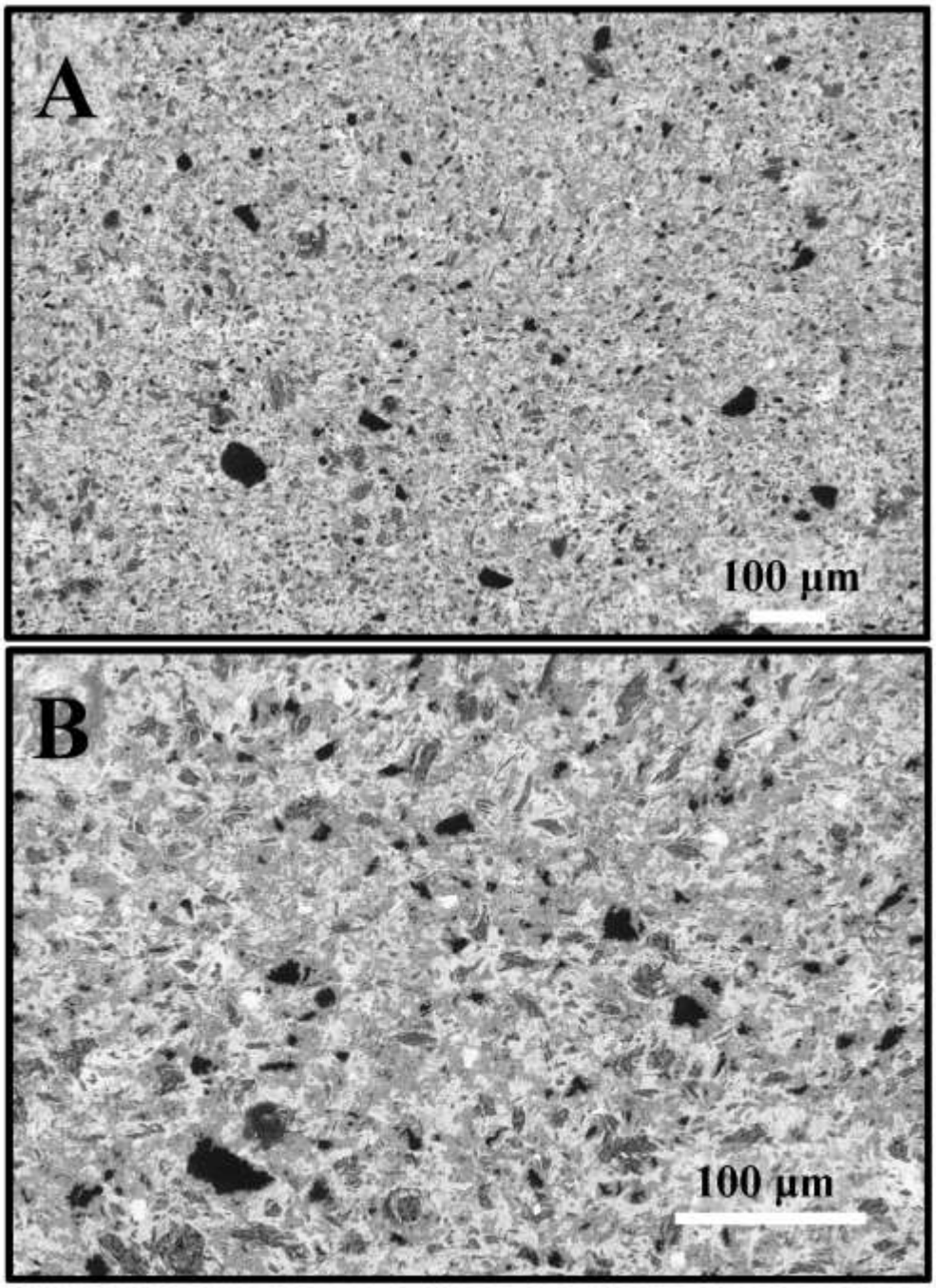

Figure 21. A) Low magnification and, B) higher magnification backscattered electrons SEM images of BR composite fabricated with Al 6061 at 1050 °C.

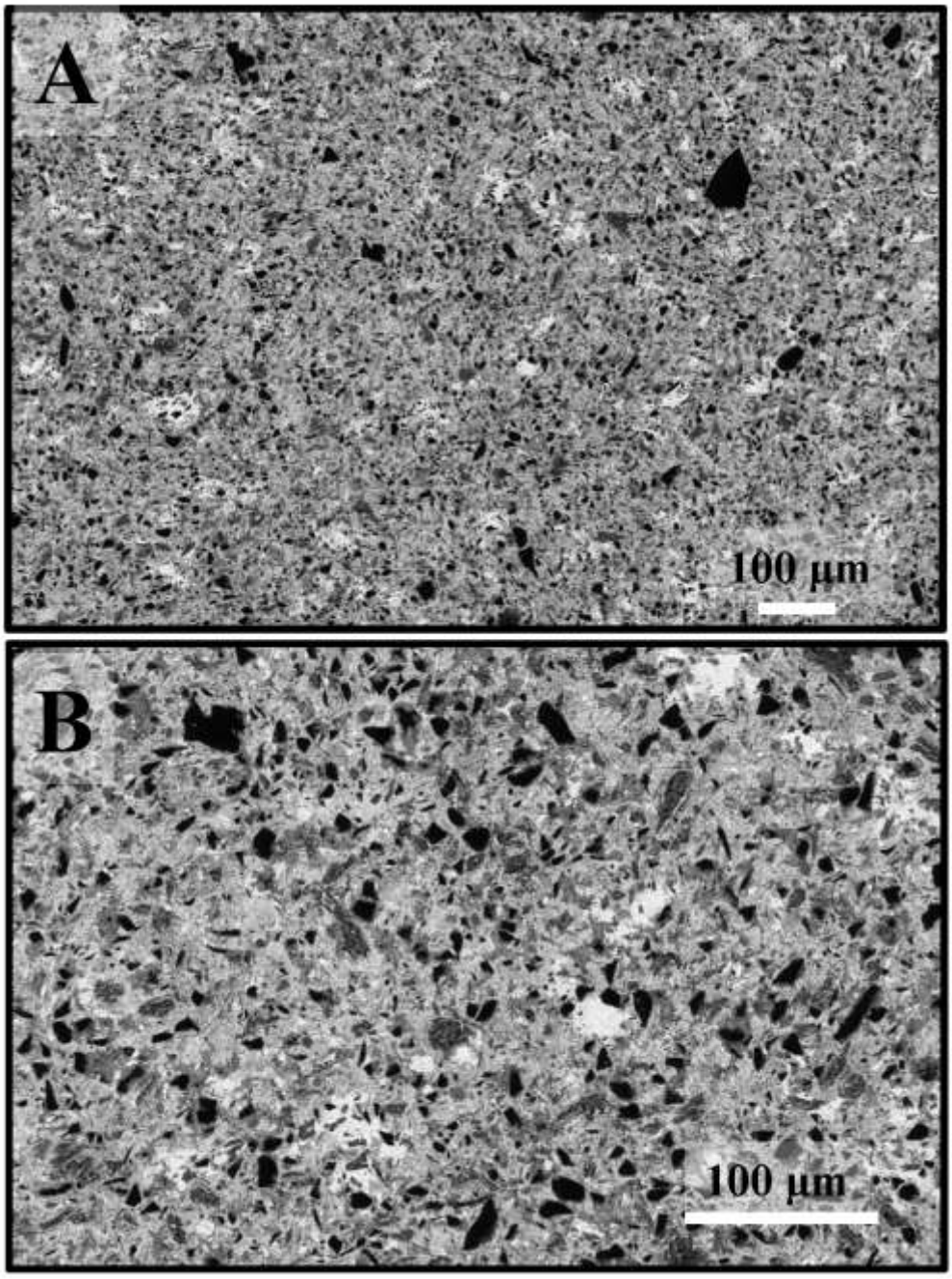

Figure 22. A) Low magnification and, B) higher magnification backscattered electrons SEM images of BR composite fabricated with Al 2024 at 900 °C.

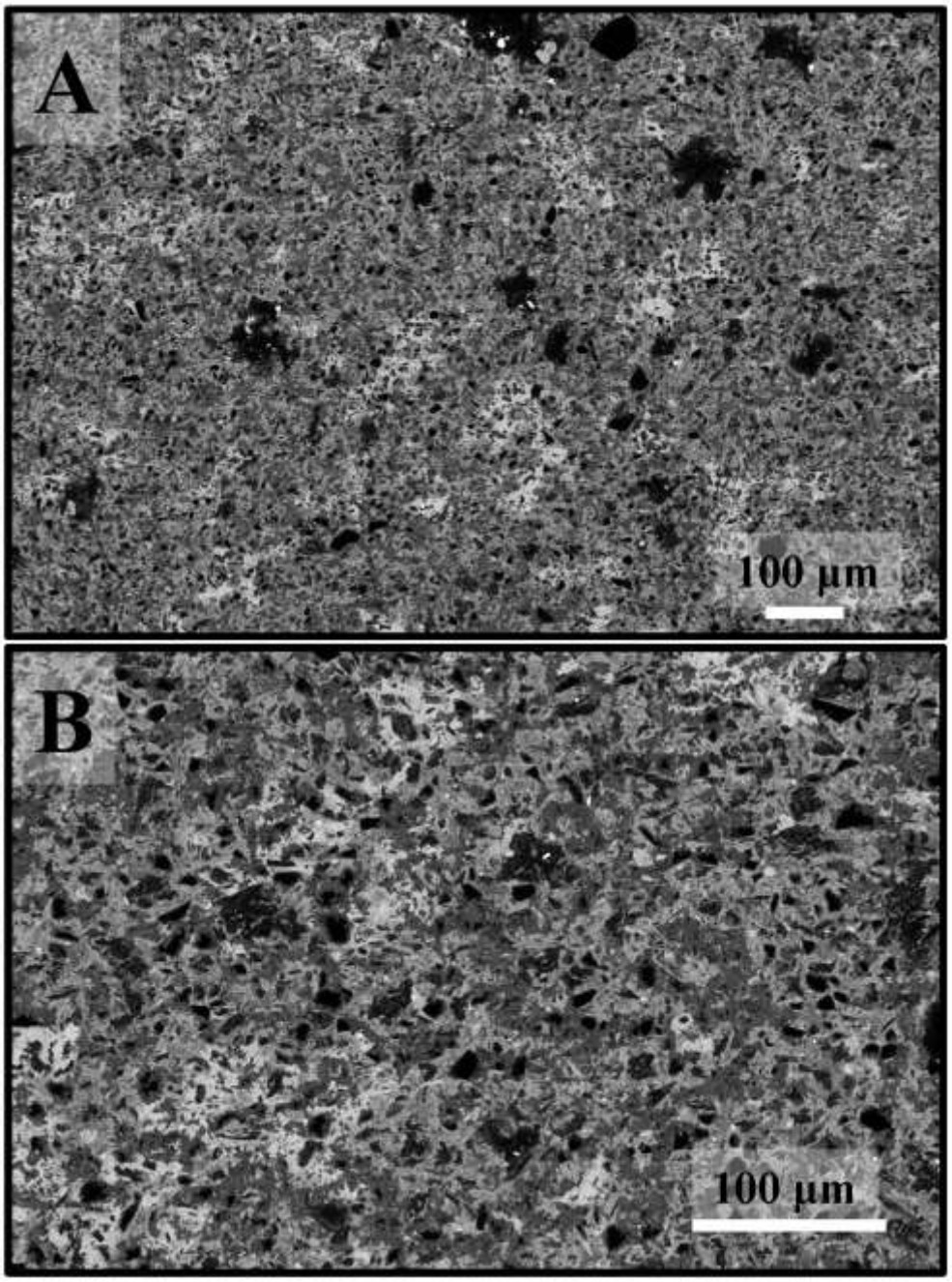

Figure 23. A) Low magnification and, B) higher magnification backscattered electrons SEM images of BR composite fabricated with Al 2024 at 950 °C.

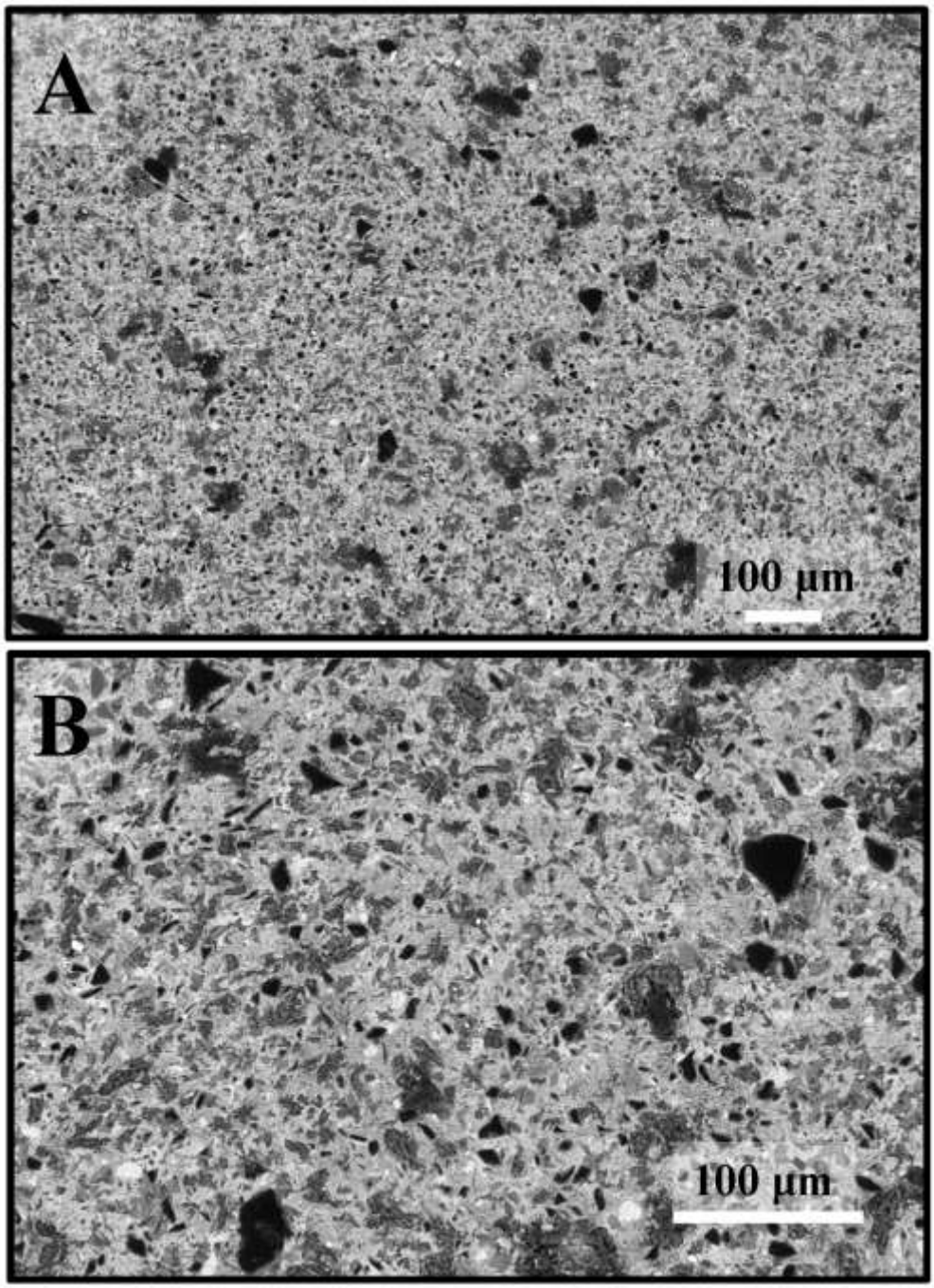

Figure 24. A) Low magnification and, B) higher magnification backscattered electrons SEM images of BR composite fabricated with Al 2024 at 1050 °C.

5.2.4. Microhardness of composites

The results of Vickers microhardness investigations are shown in Fig. 25. BR composites infiltrated with pure Al (blue points in Fig. 25) demonstrated a nearly linear increase in hardness with infiltration temperature. The average hardness ± standard deviation was found to be 5.2 ±0.2, 6.0±0.3 and 7.6±0.3 GPa after infiltration at 900, 950 and 1050 °C, respectively.

In both the BR composites infiltrated with Al alloys (6061 or 2024) the maximum hardness occurred after infiltration at 950 °C. When Al 6061 (red points in Fig. 25) was used as the matrix, the hardness after infiltration at 900 °C was 5.4±0.4 GPa. This value increased to 7.4±0.3 GPa before decreasing slightly to 7.0±0.3 GPa at 1050 °C. In a similar fashion, the BR composite with Al 2024 (green points in Fig. 25) demonstrated its lowest hardness, 6.5±0.2 GPa, after infiltration at 900°C. The hardness at 950 °C, 7.3±0.3 GPa, was comparable to that of the 6061 composite at the same temperature. Again, a slight drop to 6.8±0.2 GPa was observed when infiltrated at the highest temperature.

The TiR composite was demonstrated to have the lowest hardness at each temperature (black points in Fig. 25). The hardness after infiltration at 900 °C was 3.5±0.2 GPa. At 950 °C the hardness was more similar to that of the BR composites, having the value 5.9±0.1 GPa. After infiltration at 1050 °C, however, the hardness of the TiR composite dropped to its lowest value of 2.3±0.1 GPa.

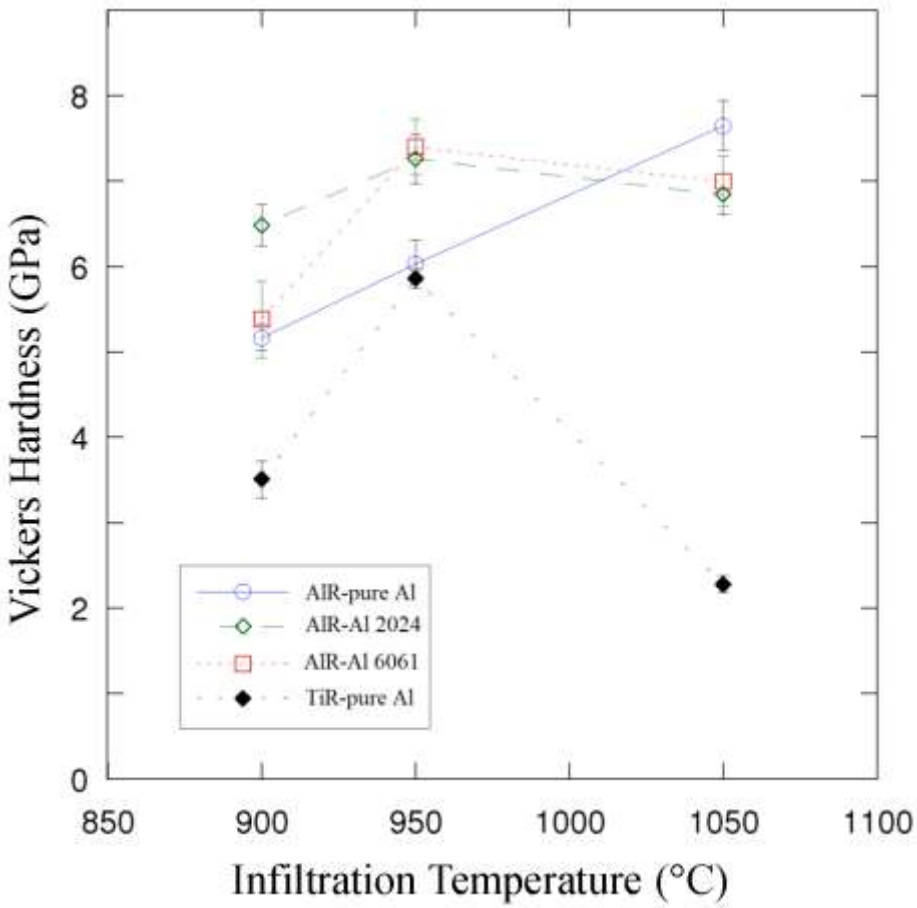

Figure 25. Vickers microhardness of Al-Ti-B-C composites as a function of infiltration temperature, soaking was held constant at 0.5 h. AlR composites were infiltrated with pure Al (blue), Al 2024 (green) and Al 6061 (red) alloys. TiR composites were infiltrated with pure Al (black).

5.3. Discussion

5.3.1. Equilibrium tetrahedra

5.3.1a. Phase equilibria in the B-rich composite

Based on the totality of the XRD and SEM results on the equilibrated BR composition it is reasonable to conclude that the 4 apexes of this equilibrium tetrahedron

are: Al, Al_3BC, TiB_2, and Al_4C_3 (pink tetrahedron in Fig. 26a, c and Supplementary Information). The starting molar composition (blue circle in Fig. 26a), clearly falls within this equilibrium tetrahedron. Note that the size of this tetrahedron is relatively small – only occupying 2.86 vol. % of the phase diagram.

To examine the robustness of our conclusions, the position of the initial composition was re-calculated assuming: the stoichiometry of B_4C to be $B_4C_{0.5}$, with all else remaining the same. When plotted, this composition point shifted by a negligible amount. We also carried out a calculation incorporating the presence of 20 wt. % Ti_3AlC_2 in the starting composition. In that case the initial Al:Ti:B:C molar ratio is 3.8:0.9:3.0:1.2. The resulting location point was nearly indiscernible from the location of the blue circle shown in Fig. 26a.

Based on these findings, it can be concluded that neither the B_4C stoichiometry nor the presence of ≈ 20 wt. % Ti_3AlC_2 in the initial powder affects the location of the initial composition in the conjectured equilibrium tetrahedron.

Based on the Rietveld refinements, the final Al:Ti:B:C molar ratio was calculated to be 3.8:1.3:2.9:0.6 (pink point in Fig. 26a) with corresponding high volume fractions of Al and TiB_2 (Table 4). The discrepancy between the initial (3.8:0.9:3.0:1.2) and final molar compositions in this system is discussed below. However, as both compositions lie within the *same* equilibrium tetrahedron, this discrepancy in no way affects the conclusions of this study.

5.3.1b. Phase equilibria in the Ti-rich composite

Based on the totality of our XRD and SEM results on the equilibrated TiR composition it is reasonable to conclude that the 4 apexes of this equilibrium tetrahedron are: Al, TiB_2, Al_4C_3, and TiC (tan tetrahedron in Figs. 26b-c and Supplementary Information). The latter occupies a larger volume of the phase diagram (14.29 vol. %) than the B-rich composition and was also found to be unaffected by non-stoichiometries in the B_4C and/or the presence of Ti_3AlC_2. In this case, the starting composition (blue circle in Fig. 26b) was in excellent agreement with the composition calculated from Rietveld refinement of the XRD results (pink point in Fig. 26b) after equilibration, with both compositions well within the boundaries of the equilibrium tetrahedron.

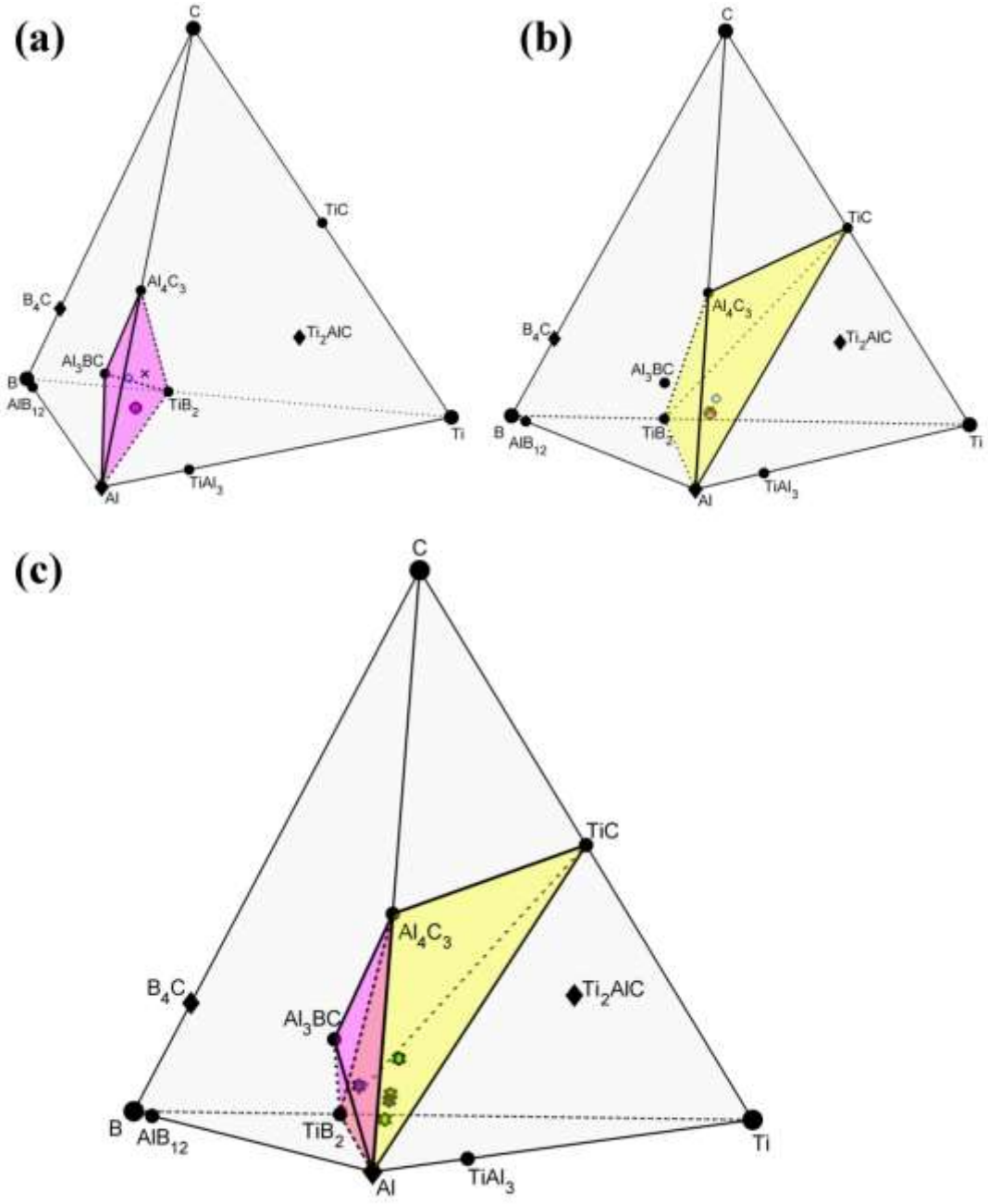

Figure 26. Equilibrium tetrahedron as determined from, A) B-rich composition. Blue circle represents the starting composition as calculated from starting powder weights, black x represents the composition as determined from the left hand side of Eq. 7; pink point represents the final molar composition as determined from Rietveld analysis of equilibrated samples. B) Ti-rich composition. Blue circle represents the starting composition as calculated from starting powder weights, black x represents the

Figure 26 continued. composition as determined from the left hand side of Eq. 14; pink point represents the final molar composition as determined from Rietveld analysis of equilibrated samples. C) Constituent Al-Ti-B-C phase diagram at 1000 °C. Green points represent 10, 40, and 60 wt. % Al compositions from Zou, et al. [24] and blue points are the nominal compositions reported by Zhang, et al. [48].

5.3.2. Constituent phase diagram at 1000 °C

An interactive quaternary phase diagram can be found in Supplementary Materials. Note that this phase diagram assumes all phases to be line compounds (Fig. 26c). That this is an oversimplification is obvious for the simple reason that TiC exists over a wide Ti:C molar ratio. However, since this is the first report of this quaternary phase diagram, and for the sake of simplicity, we chose to assume TiC and all other compounds to be line compounds. Understanding how the non-stoichiometry of TiC affects the diagram is important and should be mapped out, but is beyond the scope of this work.

5.3.3. Reaction mechanisms

5.3.3a. B-rich composites

Based on the results summarized in Table 4, together with the reaction-path-superimposed quaternary phase diagram (Fig. 27) – where dashed lines represent reacting phases, solid lines represent reaction products, and bold lines outline the equilibrium phase relations – the following reactions are surmised to occur in the BR composition:

$$5/2\ (\ 9\ Al + 2\ B_4C \rightarrow 2\ Al_3BC + 3\ AlB_2\ ) \quad (2)$$

$$9/2\ (\ 2\ Al + \ Ti_2AlC \rightarrow TiAl_3 + \ TiC\ ) \quad (3)$$

$$9/2\ (\ TiAl_3 + \ AlB_2 \rightarrow \ TiB_2 + 4\ Al\ ) \quad (4)$$

$$3/2\ (\ TiC + \ 2\ Al_3BC \rightarrow \ TiB_2 + Al_4C_3 + 2\ Al\ ) \quad (5)$$

$$3\ (TiC + \ AlB_2 + Al \rightarrow \ TiB_2 + 1/3\ Al_4C_3\ ) \quad (6)$$

for the overall reaction:

$$4.5\ Ti_2AlC + \ 5\ B_4C + \ Al_{excess} \rightarrow 9\ TiB_2 + 2\ Al_3BC + \ 2.5\ Al_4C_3 + Al_{excess} \quad (7)$$

Upon wetting of the preform by molten Al, the initial reactions would be between Al/B_4C and Al/Ti_2AlC according to Eq. 2 and 3, respectively. AlB_2 and Al_3BC are in equilibrium below the peritectic transformation temperature of AlB_2, and B_4C has been reported to react with Al to form these products in various experiments [53, 57, 58]. Both of these phases were observed herein. The reaction of Ti_2AlC with Al (Eq. 3) at the investigated temperatures is in agreement with the surmised reaction path of Ti_3AlC_2 with Al above 900 °C [22].

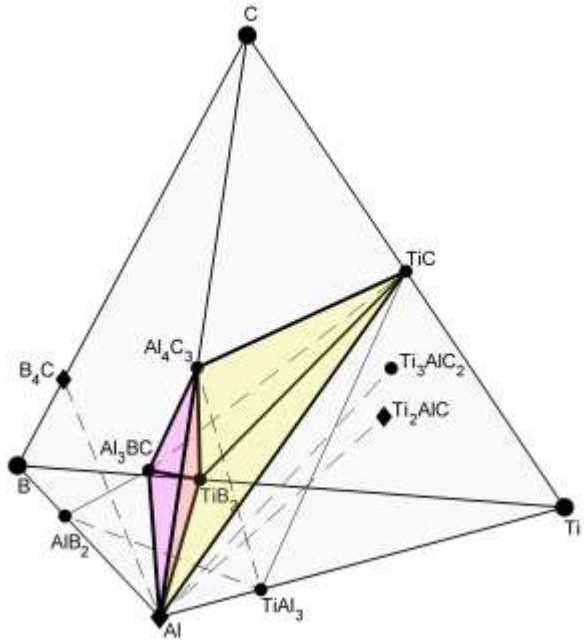

Figure 27. A reaction-path-superimposed quaternary phase diagram visually demonstrating Eqs. 2-6, 12 and 16. Dashed lines represent reacting phases, solid lines represent reaction products, and bold lines outline the equilibrium phase relations. Note that the "hidden" face of the quaternary diagram is the Ti-B-C triangle.

Reaction 3 is also to be expected from an inspection of the ternary phase diagram (Fig. 4) as the TiC/$TiAl_3$ equilibrium line must be crossed in reacting Al with the Ti_2AlC (labeled 'H' in Fig. 4). While $TiAl_3$ was not observed in this system, its production by this reaction is presented clearly in the TiR composite fabricated at 900 °C (see below). Of the four phases produced by these two reactions (Eqs. 2 and 3) only Al_3BC is an equilibrium phase, indicating that the transient phases – AlB_2, $TiAl_3$, and TiC – must at some point react to form equilibrium phases (Eqs. 4 and 5). The formation of TiB_2 by the reaction of $TiAl_3$ with AlB_2 has been previously reported in Al matrix composites, though largely through aluminothermic reactions of KF based salts in an Al melt [59, 60]. Additionally, thermodynamic calculations indicate that the reaction between TiC and AlB_2 (Eq. 6) is favorable in high temperature Al melts [10]. Lastly, the reaction between TiC and Al_3BC (Eq. 5) was inferred by the necessity to balance the overall reaction (Eq. 7) and has not been found in the literature. It is not unreasonable to speculate about the feasibility of this reaction as it keeps in line with the finding that TiC is not stable in some Al-B systems [10]. The continual consumption of TiC in Eqs 5 and 6 is in agreement with the decreasing TiC peak intensities in the XRD spectra acquired for each infiltration temperature (Fig. 12).

Rietveld analysis of the equilibrium microstructure resulted in the overall reaction:

$$4.5\,Ti_2AlC + 5\,B_4C + Al_{excess} \rightarrow 9\,TiB_2 + 2\,Al_3BC + 0.67\,Al_4C_3 + Al_{excess} \quad (8)$$

In general, the agreement between the surmised reaction (Eq. 7) and reaction Eq. 8 is excellent with the only difference being that the Rietveld calculations show less Al_4C_3 that surmised. The cause of this may be rationalized in two ways: i) some amount of

Al_4C_3 may have hydrolyzed and became amorphous prior to the collection of the XRD patterns, which would underrepresent the amount of Al_4C_3 in the Rietveld calculations; and/or ii) non-stoichiometric B_4C and/or impurities in the starting powders may be responsible for the production of less Al_4C_3. As noted above, however, since the molar compositions of both the left and right sides of Eq. 8 clearly fall within the *same* equilibrium tetrahedron (black X and pink point in Fig. 26a, respectively) the unbalanced equation has no effect on the results of this study. It may be for similar reasons that there is a disagreement between molar compositions from Rietveld calculations and the starting powder weights; however, as all molar compositions fall within the *same* equilibrium tetrahedron the results of this study are sound.

Examination of the BR microstructures at each infiltration temperature coincides with the proposed reaction path. No MAX phase is observed in this system, indicating that Eq. 3 must occur rapidly after wetting of the preform. The reaction with B_4C (Eq. 2), however, continues even after equilibration for 10 h (Fig. 10 c). It has been suggested that Al_3BC forms a diffusion barrier and limits the rate at which the B_4C grains are consumed by Al and also the rate at which boron diffuses into the matrix [53]. The results shown herein support this finding. As evidence for $TiAl_3$ was also unobserved by our XRD or SEM investigations, and since more AlB_2 is produced (Eq. 2) than $TiAl_3$ is consumed (Eq. 4) it is probable that this reaction also occurs rapidly following the production of AlB_2. This also explains why AlB_2 could be found in some microstructures (Fig. 10b and 8), as the remaining AlB_2 is proposed to be consumed by TiC (Eq. 5), presumably by a slower reaction since both of these phases were observed.

The higher magnification SEM micrographs of the sample fabricated at 1050 °C (Fig. 15) sheds more light on the reaction path: the un-reacted B_4C is surrounded by an Al_3BC layer (expected from Eq. 2), AlB_2 is found in Ti-containing regions which is necessary if it is to react with TiC, and TiC was also found near the Al_3BC phase, making it feasible that they could react to bring the system to equilibrium (Eq. 6).

5.3.3b. Ti-rich composites

In a similar fashion, the TiR composite system may be analyzed in light of the phase diagram developed herein. The suggested reaction path is:

$$2\ (\ 9\ Al + 2\ B_4C \rightarrow 2\ Al_3BC + 3\ AlB_2\ ) \tag{9}$$

$$7\ (\ 2\ Al + \ Ti_2AlC \rightarrow TiAl_3 + \ TiC\ ) \tag{10}$$

$$6\ (\ TiAl_3 + \ AlB_2 \rightarrow \ TiB_2 + 4\ Al\ ) \tag{11}$$

$$2\ (\ TiC + \ 2\ Al_3BC \rightarrow \ TiB_2 + Al_4C_3 + 2\ Al\ ) \tag{12}$$

$$1/3\ (\ 3\ TiAl_3 + \ Al_4C_3 \rightarrow 3\ TiC + 13\ Al\ ) \tag{13}$$

that sums to the overall reaction:

$$7\ Ti_2AlC + \ 4\ B_4C + \ Al_{excess} \rightarrow 8\ TiB_2 + 6\ TiC + \ 1.66\ Al_4C_3 + Al_{excess} \tag{14}$$

Since Eqs. 9 – 12 are identical to Eqs. 2 – 5, they will not be discussed further. However, in order to consume the remaining $TiAl_3$ and bring the system to equilibrium, Eq. 13 is proposed. This reaction is expected from analysis of the Al-Ti-C ternary diagram (Fig. 4) and has been reported to occur at temperatures above the melting point of Al [40].

Rietveld analysis of the equilibrium microstructure translates to the following overall reaction:

$$7\,Ti_2AlC + 4\,B_4C + Al_{excess} \rightarrow 8\,TiB_2 + 6\,TiC + Al_4C_3 + Al_{excess} \qquad (15)$$

which, with the exception of Al_4C_3, is in excellent agreement with Eq. 14. Here again the major discrepancy between two reactions is the lower amounts of Al_4C_3 in the experimental results (Eq. 15). At this stage there is no reason that some of the reasons invoked to account for this deficiency in the BR composition does not apply here as well. This comment notwithstanding, more work is needed to further understand the discrepancy. However, since the molar compositions of both the left and right sides of Eq. 15 fall within the *same* equilibrium tetrahedron (black X and pink point in Fig. 26b, respectively) the fact that Eq. 15 is unbalanced has no effect on the quaternary diagram.

When the short time MI experiments for the TiR and BR compositions are compared, it becomes obvious that the sequence and rates of some of the reactions are notably different. For example, Ti_2AlC was not observed in the TiR composition, but its reaction products (Eq. 10) were seen in the XRD patterns (Fig. 13a) and SEM micrographs (Fig. 14a). In contrast, the reaction products of B_4C with Al, Al_3BC and AlB_2 (Eq. 9) phases were not observed after processing at 900 °C. This is clear evidence that Ti_2AlC is less stable in excess Al than B_4C. However, at 950 °C a notable shift in reaction products occurs. $TiAl_3$ is consumed and Al_3BC is produced (Eqs. 9 and 11), likely the result of increased reactivity of B_4C with Al (Eq. 9) at the higher temperature. As with the BR system, this indicates that $TiAl_3$ is rapidly consumed upon the production of AlB_2 (Eq. 11), as AlB_2 was not identified from XRD and the $TiAl_3$ peaks almost

disappear (Fig. 13b). Al_3BC is clearly a primary phase at 950 °C, which argues in favor of a slower reaction between TiC and Al_3BC (Eq. 12) than the rate at which Al_3BC is produced. It may also be that Eq. 12 is responsible for the change in microstructure between 950 and 1050 °C (Fig. 14b and c, respectively). The consumption of Al_3BC (Eq. 12) and remnant $TiAl_3$ (Eq. 13) is necessary to bring the system to equilibrium.

5.3.3c. Reaction with Ti_3AlC_2

The aforementioned reaction mechanisms coincide well with the observations in both BR and TiR systems. However, it is important to recognize the potential for other reactions to occur in this quaternary system. Ti_3AlC_2 exists in the starting powder and was the only MAX phase to be observed in any of the composites (TiR at 900 °C, Fig.7b); however, it was left out in the overall reaction scheme for simplicity. In both systems the likely reaction is:

$$2\,Al + Ti_3AlC_2 \rightarrow TiAl_3 + 2\,TiC \qquad (16)$$

as detailed in the literature [22]. However, given that the fraction of this phase in the starting powder is small, it is reasonable to assume that it would not have a significant impact on the overall reactions (Eq. 8 or 14).

5.3.4. Comparison with literature results

The reaction products after melt infiltration at 1000 °C established in this work agree with the products reported by other researchers using similar compositions, but different reaction methods. For example, Zou et al. (2007) [33] produced TiC-TiB_2-Al composites between 10 and 60 wt. % Al using self-propagating high-temperature

synthesis. The maximum temperature of their reaction decreased from 2900 °C and approached the investigated temperature range of this work as the Al wt. % increased. Calculations show that their Al:Ti:B:C ratio ranges from 0.8:3.0:4.0:1.0 with 10 wt. % Al, to 11.1:3.0:4.0:1.0 with 60 wt. % Al. These compositions lie on the Al-TiB_2-TiC face of the quaternary phase diagram (green points represent 10, 40, and 60 wt. % Al in Fig. 26c). In addition to these phases, they also reported that Al_4C_3 and $TiAl_3$ were also present in small amounts as a consequence of the fact that their system was not allowed to reach equilibrium.

Zhang, et al. (2014) [61] utilized quick spontaneous infiltration to make composites from Ti-B_4C-Al powder preforms (55–60 % dense) dipped in molten Al at 920 °C. The nominal composition of two of their composites, with Al:Ti:B:C molar ratios of 6:3:6:1.5 and 6:3:4:1, fall on the Al-Al_4C_3-TiB_2 and Al-TiB_2-TiC faces of the quaternary phase diagram, respectively (blue points in Fig. 26c). In both composites, Al, TiB_2, and TiC were the primary phases found. In the B-rich composite, some $TiAl_3$ was also detected. Neither Al_4C_3 nor Al_3BC was observed by XRD after infiltration or differential thermal analysis (DTA) of both composites. Consequently, they computationally determined that the likely equilibrium products of the more B-rich composite were Al_3BC, TiB_2, and $TiAl_3$. Our findings show that $TiAl_3$ is not an equilibrium product of this composition.

However, the equilibrium phases present in the B-poor composition – Al, TiB_2, and TiC – are in full agreement with our results [61]. Their conclusion that B_4C is also in equilibrium with TiB_2 and TiC is at odds with our results. The most likely source of these discrepancies is the fact that Zhang et al. (2014) [61] did not allow their samples to reach equilibrium.

5.3.5. Discussion of microhardness measurements

The microhardness of the composites may be evaluated with respect to the microstructure and aforementioned reaction mechanisms. In the BR system, low temperature infiltration was found to have the highest amount of AlB_2 and TiC, and the least amount of TiB_2 (Table 4). As AlB_2 has a lower hardness than both Al_3BC and TiB_2 (Table 5), it is likely that the presence of this phase and the lesser relative amounts of Al_3BC and TiB_2 contributes to the lowest observed hardness for each composite in this system. As the temperature increased to 950 °C, more Al_3BC may be produced by further reaction between Al and B_4C. Similarly, more TiB_2 is produced as the reaction is allowed to progress. For the BR composite fabricated with pure Al, the hardness continued to increase after infiltration at 1050 °C. This may be the result of the system tending towards equilibrium, where Al, TiB_2, Al_3BC and Al_4C_3 are the only remaining phases. As the morphology of the microstructure is similar between each infiltration temperature, the composite hardness is likely only dependent on the relative volume fractions of its constituent phases. For BR composites fabricated with Al alloys 6061 or 2024 the hardness had a similar behavior to the pure Al composite. The higher initial hardness at 900 and 950 °C may be a direct or indirect result of the alloying elements. The hardness of the Al matrix may be inherently higher than that of pure Al, or the alloying elements slow down the reaction between Al and B_4C, and more B_4C reinforcement would also increase the hardness of the composite at lower temperatures. Unlike the hardness of the pure Al composites, the hardness of the Al alloy composites remains constant or drops slightly after infiltration at 1050 °C, this may be attributed to the system tending towards equilibrium. Further investigation is necessary to assess the influence of the volume

fraction of reinforcement phases on the microhardness of each composite, but is beyond the scope of this work.

The microhardness of the TiR composite may also be considered with respect to the microstructural analysis. At 900 °C $TiAl_3$ is a predominant phase and the corresponding microhardness was substantially less than the BR composites. This may be expected as the hardness of $TiAl_3$ is approximately 75 % softer than TiB_2, which was not a major phase in this composite (Table 4). Following the reaction model, at 950 °C the TiR composite exhibits similar reaction products to that of the BR composite system – primarily Al_3BC and TiB_2. Consequently, the hardness of this TiR composite was very similar to that of the corresponding BR composite. The drop in hardness of the TiR composite at 1050 °C is not expected if the volume fraction of TiB_2 and TiC continues to increase as the composite tends towards equilibrium. However, this is the only composite to exhibit a significant change in microstructure and it may be that the small dispersed particles of TiB_2 and TiC interact with the Al matrix in a different manner that the other composite systems. Again, the effects of reaction products and microstructure on mechanical properties require further investigation, but are beyond the scope of this work.

A comparison of hardness values for BR and TiR composites was made with composites reported in the literature (Table 5). The BR composite was found to be similar to the B_4C-TiB_2-Al composite fabricated by Lu, et al (2010) [62], who demonstrated the primary reinforcement phases TiB_2, Al_3BC and B_4C after vacuum infiltration at 1100 °C. Furthermore, they reported a nominal composition of TiB_2

between 10 and 40 wt. %, which is similar to the composition of the BR composite – which demonstrated 44.6 wt. % TiB_2 after equilibration.

As discussed above, the hardness of the TiR composite notably changed with the observed microstructure at each infiltration temperature. Having $TiAl_3$ as a primary reinforcement phase at 900 °C, a comparison was made to the Al-$TiAl_3$ composites reported by Hsu, et al (2007) [63]. The TiR composite hardness (3.5 GPa) was found to be within the range reported for MMCs with between 7 and 24 vol. % $TiAl_3$ (3.1 – 4.5 GPa). At 950 °C, the hardness is similar to that of the BR composite and between the hardness values for the $TiAl_3$ and B_4C-TiB_2-Al composite, which corresponds with the observed production of Al_3BC and TiB_2 in the TiR composite at this temperature. The decrease in hardness at 1050 °C is likely to be associated with the change in microstructure at this temperature. This possibility was evaluated with respect to observations made by Albiter, et al (2000) [9] and Pacheco, et al (2008) [64], who made TiC and TiB_2 reinforced (50 vol. %) composites with similar particle size (< 10 μm), respectively. While the TiR composite demonstrated a lower hardness than either of the reported composites, there was a trend for these composites to be softer than Al_3BC containing composites. While further investigation is required to understand the relationship between microstructure and hardness in the BR and TiR composites, this work demonstrated the similarity in hardness of the composites fabricated herein to those reported in the literature with similar reaction products.

Table 5. Hardness values for various materials and composites taken from the literature for comparison with the Al-Ti-B-C composites of this study.

Constituent Phases	Hardness (GPa)
Pure Al	1.2 GPa[65]
$TiAl_3$	5.9 GPa [66]
AlB_2	10.3 GPa[65]
Al_4C_3	12.3 GPa[65]
Al_3BC	13.7 GPa[65]
TiC	11.8-25.7 [67]
TiB_2	25 GPa [68]
B_4C	31.6 GPa[65]
Composites from the Literature	**Hardness (GPa)**
Al 2024 with 52-55 vol.% TiC	2.6 GPa [9]
53 vol.% Al-TiB_2, 95% dense	3.78 GPa [64]
Al with 7-24 vol. % $TiAl_3$	3.1 – 4.5 GPa [63]
Al-Al_3BC-TiB_2-B_4C	6.6 – 7.3 GPa [62]
BR composite	5.2 – 7.3 GPa (this study)
TiR composite	2.3 – 5.9 GPa (this study)

*5.4. **Summary of findings***

- The 1000 °C Al-Ti-B-C quaternary phase diagram in the Al-rich corner was determined. The final Al:Ti:B:C ratios in the equilibrated microstructures were 3.8:1.3:2.9:0.6 (B-rich) and 3.4:1.1:1.3:0.7 (Ti-rich).
- And while both compositions were located near the center of quaternary phase diagram, they belonged to two separate equilibrium tetrahedra. For the B-rich composition the equilibrium phases were Al, Al_3BC, TiB_2 and Al_4C_3. In the Ti-rich case, the equilibrium phases were Al, TiC, TiB_2 and Al_4C_3.
- A reaction mechanism was proposed for both compositions to explain the observed reaction products after 0.5 h MI experiments and equilibrium conditions.
- Hardness data for all BR and TiR composites was presented and compared to the hardness reported for current Al matrix composites in the literature.

Chapter 6.
Characterization of Al-V-C composites

6.1. Results

6.1.1. Synthesis of Al-V_2AlC Composites

No fully dense samples were fabricated after reacting the powder preforms at 1000°C even after soaking for 10 h. The density of the water quenched AlR samples was ≈ 90 % theoretical density with no apparent relation between soaking time and densification. The VR samples ranged in density from 30 – 60 %, no trends with soaking time were observed in this system either. Due to their low relative density, the VR samples could be easily crushed by hand and were unable to be polished.

The predominantly two phase nature of both the AlR and VR composites, after quenching from 1000 °C, was demonstrated by XRD (Fig.28) and SEM (Figs. 29 and 30) investigations. Rietveld analysis of the XRD spectra for water quenched AlR composites (Fig. 28a) gave the volume fractions Al = 71.6, V_2AlC = 22.6 and Al_3V = 5.8. The same analysis of the XRD spectra for the water quenched VR composites (Fig. 28b) gave the volume fractions Al = 49.6 vol. % (35.6 wt.%) and V_2AlC = 50.4 vol. % (64.4 wt.%). The χ^2 value of the Rietveld refinement of the XRD patterns for the AlR and VR composites was 3.40 and 1.34, respectively.

EDS of the water quenched AlR sample confirmed that the microstructure consists of V_2AlC and some Al_3V grains dispersed throughout an Al matrix (Fig. 29). Large pores can be seen at low magnification (Fig 29a) and Al particles that did not break

their oxide shell can be seen at high magnification (Fig 29b). SEM of the water quenched VR composite clearly demonstrates its porous structure (Fig. 30a). V_2AlC was clearly identified from EDS and was found dispersed among the Al.

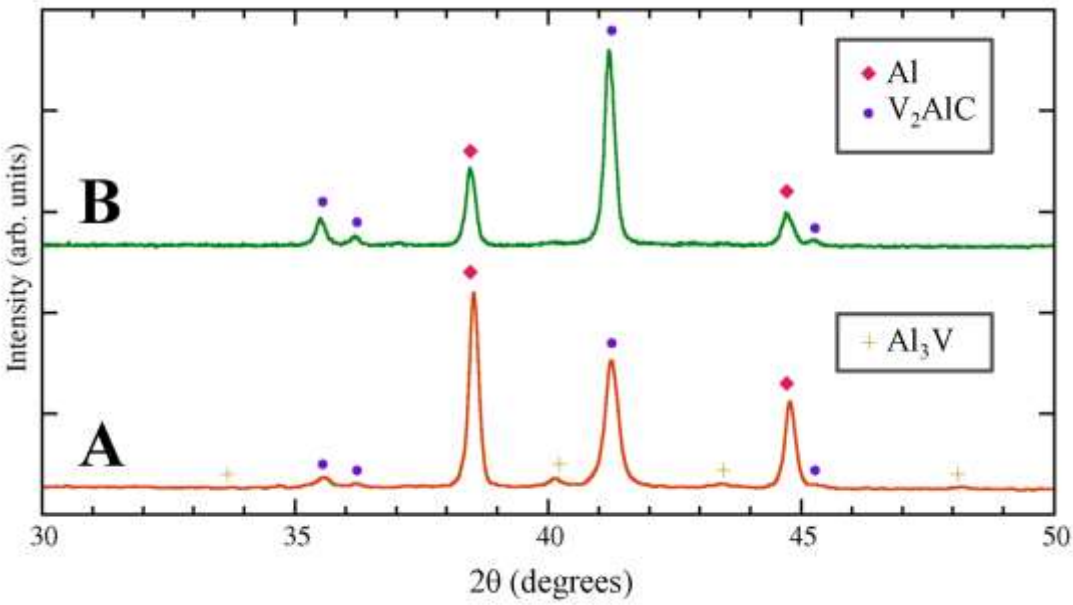

Figure 28. Typical XRD spectra of water quenched, a) AlR and, b) VR composites after soaking at 1000 °C and water quenched.

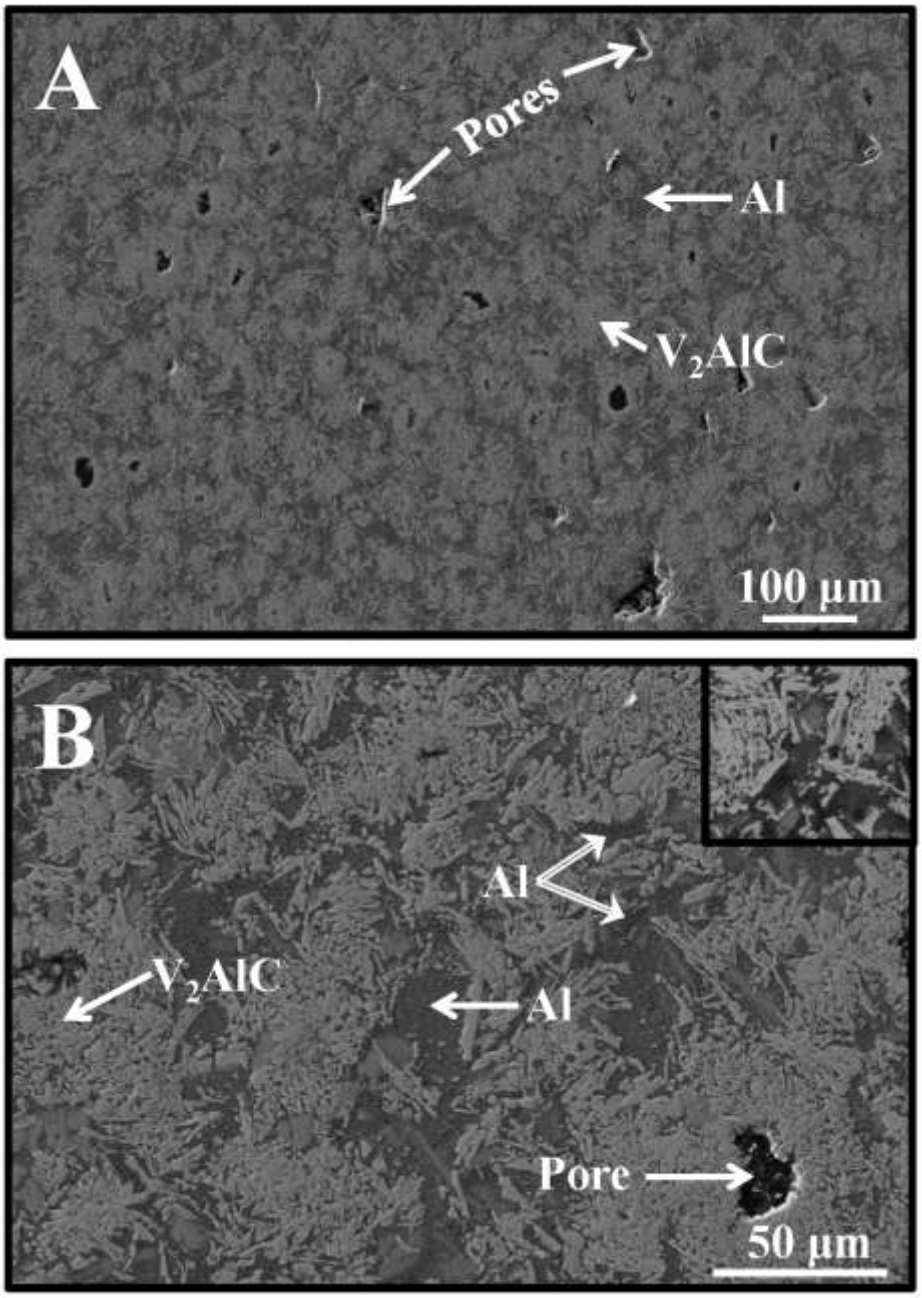

Figure 29. Secondary electrons SEM image of a water quenched AlR composite after soaking at 1000 °C for 2.5 h. (a) Imaging at low magnification demonstrates homogeneity of the composite, with some large pores throughout. (b) Higher magnification imaging demonstrates V_2AlC grains dispersed among Al particles that densified and those that did not break their oxide shell, verified by backscattered electrons image (inset).

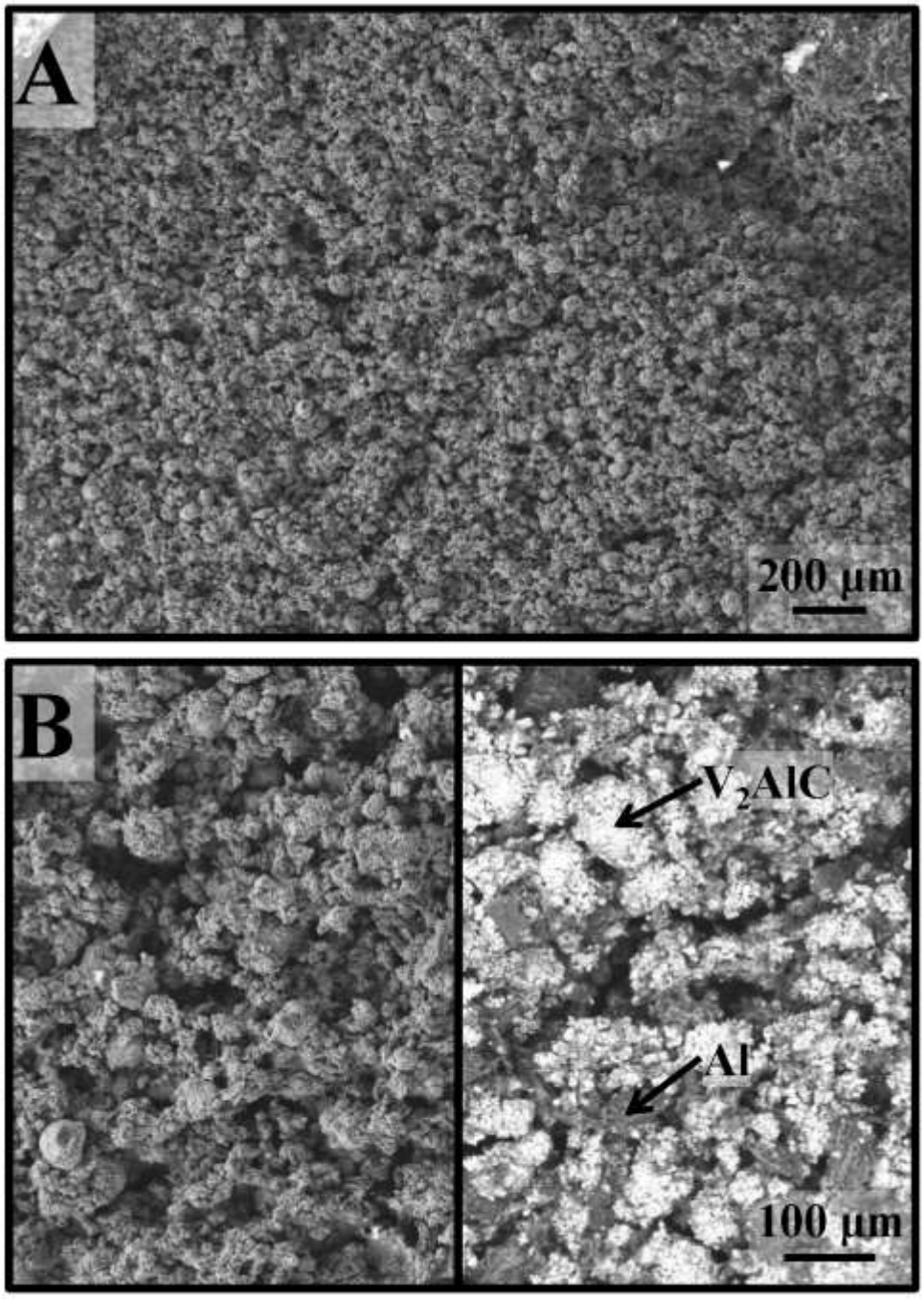

Figure 30. Secondary electrons SEM image of a water quenched VR composite after soaking at 1000 °C for 2.5 h. (a) Imaging at low magnification demonstrates the porosity of the sample. (b) Higher magnification imaging demonstrates clumps of V2AlC grains held together by Al particles, verified by backscattered electron image (right).

Somewhat surprisingly, the AlR and VR samples allowed to furnace cool after 10 h at 1000 °C were not found to contain V_2AlC in an Al matrix (Fig. 31). Rather, the AlR sample was primarily Al_3V and Al-rich intermetallics ($Al_{23}V_4$, $Al_{45}V_7$ and $Al_{21}V_2$), with trace amounts of Al_4C_3 (Fig. 31a). The latter, was comprised of V_2AlC, Al_3V and some Al_4C_3 (Fig. 31b).

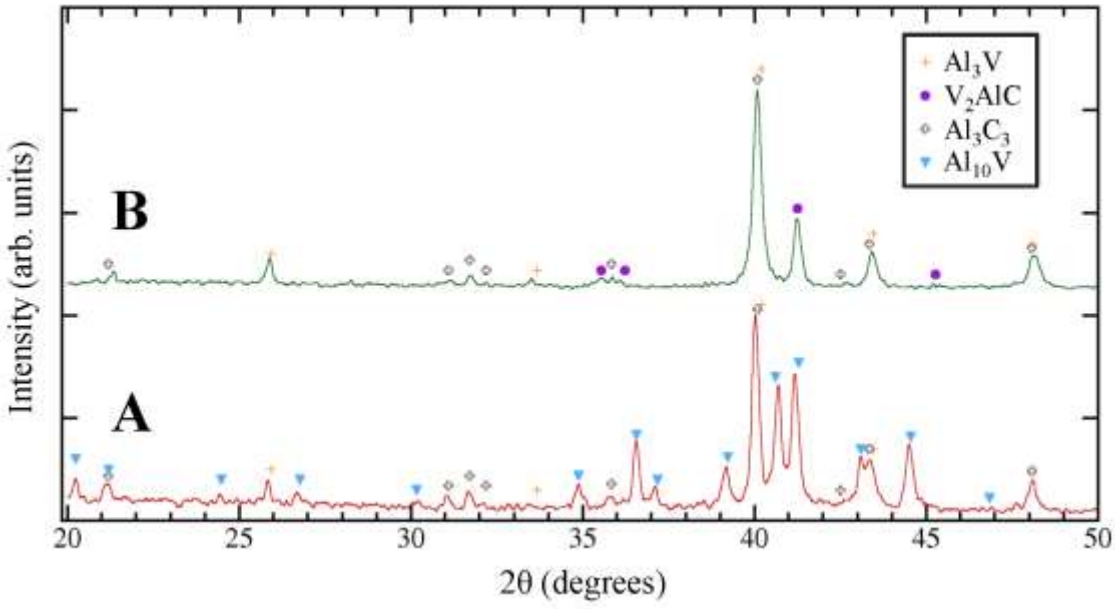

Figure 31. Typical x-ray diffraction spectra for furnace cooled, a) AlR and, b) VR composites that no longer demonstrate the coexistence of V_2AlC with Al.

6.1.2. Differential scanning calorimetry

The DSC results for the DSC-WQ sample (Fig. 32) demonstrated 2 distinct exothermic peaks (labeled in Fig. 32a as P1 and P2, respectively) and 1 endothermic peak (labeled P3 in Fig. 32a) during heating; and 1 exothermic peak during cooling (labeled P4 in Fig. 32b). Additionally, a possible endothermic peak (labeled P5 in Fig. 32a) was identified at the leading edge of P1 at T = 659 °C (Fig. 32a). The maximum of P1

occurred at T = 685 °C. The second exothermic peak, P2, had an onset temperature of approximately 731 °C and reached a maximum at 739 °C. The endothermic peak, P3, began when T ≈ 940 °C and ended by T ≈ 970 °C. The only peak observed during cooling, P4, began when T ≈ 924 °C and ended at T ≈ 894 °C. Note the similar magnitudes and ranges of P3 and P4. Their areas were calculated to be the same within 10 %.

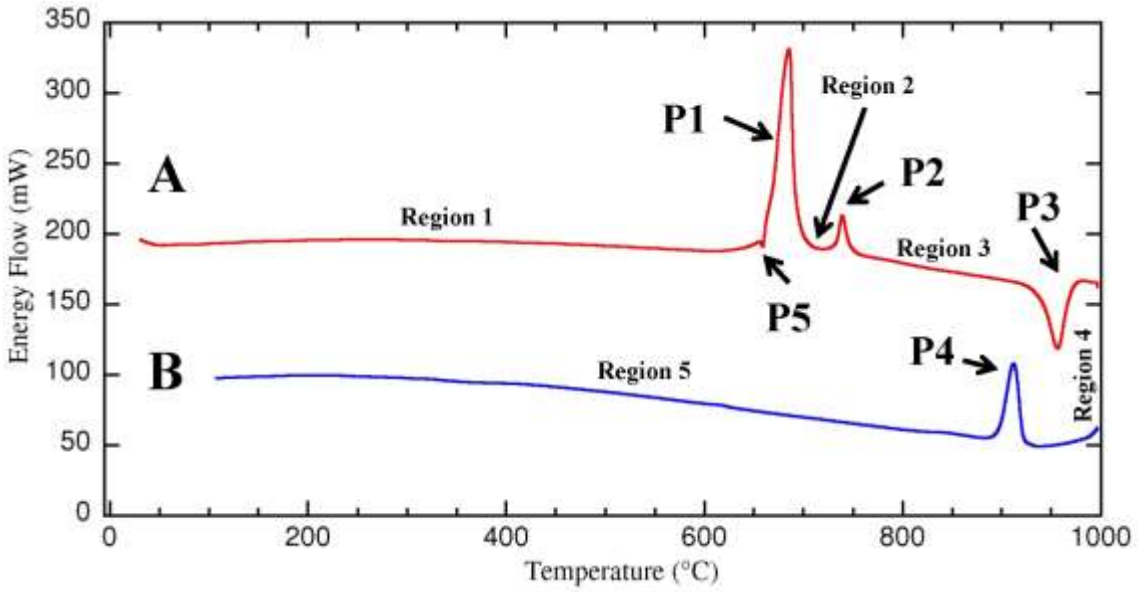

Figure 32. DSC curve for the DSC-WQ sample demonstrating two exothermic peaks and one endothermic peak during heating (a) and one exothermic peak during cooling (b). The heating and cooling curves were separated for clarity. The linear offset from 0 is +200 and +100 for the heating and cooling curve, respectively.

The DSC curve for the furnace cooled sample, DSC-FC, exhibited three small endothermic peaks (labeled as π1, π2 and π3, respectively, in Fig. 33a), one sharp exothermic peak (labeled π4 in Fig. 33a) and a larger endothermic peak (labeled π5 in Fig. 33a) during heating. During cooling, two exothermic peaks were identified (π6 and

π7 in Fig. 33b). The minimum of π1 occurred at T = 660 °C and spanned T ≈ 657 – 666 °C. The onset temperature of π2 was T ≈ 686 °C and spanned to T ≈ 695 °C. π3 was found to be broader than π1 or π2, spanning from T ≈ 710–740 °C, with the minimum occurring at T = 727 °C. The exothermic peak, π4, had a maximum at T = 814 °C, having the range T = 798 – 829 °C. The larger endothermic peak, π5, began at T = 943 and ended by 995 °C, the minimum occurred at T = 968 °C. This peak was similar in magnitude to the exothermic peak, π6, that began during cooling at T = 935 °C and continued to T = 887 °C. Again, note the similar magnitudes between the exothermic peak, π5, and endothermic peak, π6. Their areas were calculated to be the same within 10 %. A second small exothermic peak observed during cooling, π7, began at T = 657 °C, climaxed at T = 651 °C and had finished by T = 636 °C.

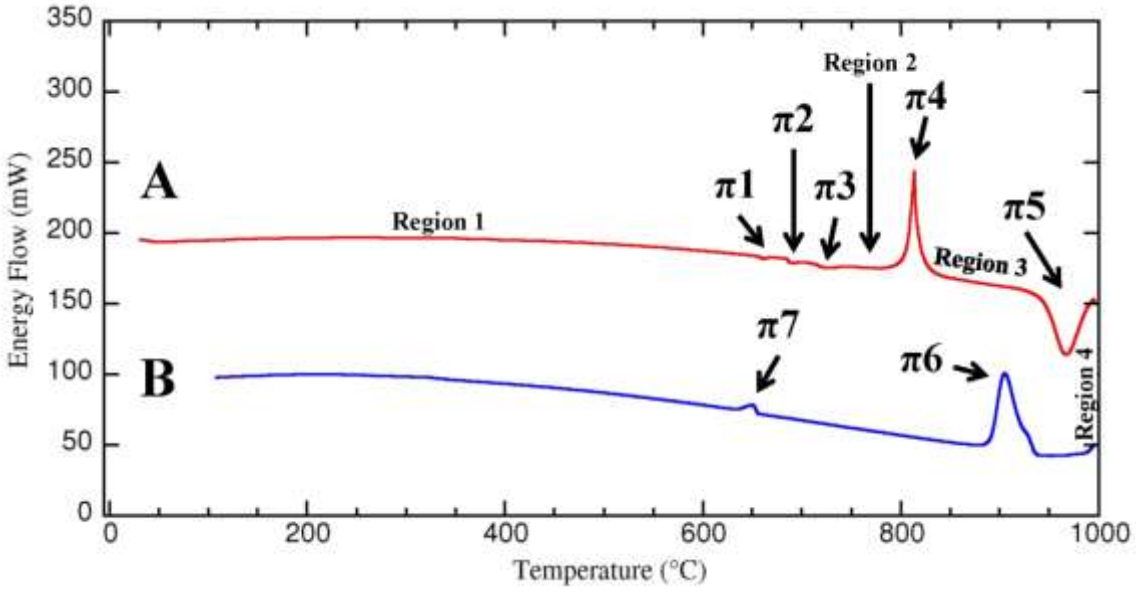

Figure 33. DSC curve for the DSC-FC sample demonstrating one exothermic peak and one endothermic peak during heating (a) and two exothermic peaks during cooling (b). The heating and cooling curves were separated for clarity. The linear offset from 0 is +200 and +100 for the heating and cooling curve, respectively.

6.1.3. Equilibration experiments

After equilibration of the DSC-WQ sample at 800 and 1000 °C, XRD was used to confirm the phase relations (Fig. 34). At 800 °C the equilibrium phases were Al, Al_3V and Al_4C_3 (Fig. 34a). At 1000 °C, the equilibrium phase relations – Al, Al_3V and V_2AlC (Fig. 34b) – replicated those reported by Schuster, et al [30]. Furthermore, it was found that transitioning between these equilibria was fully reversible after cyclic heating between 800 and 1000 °C.

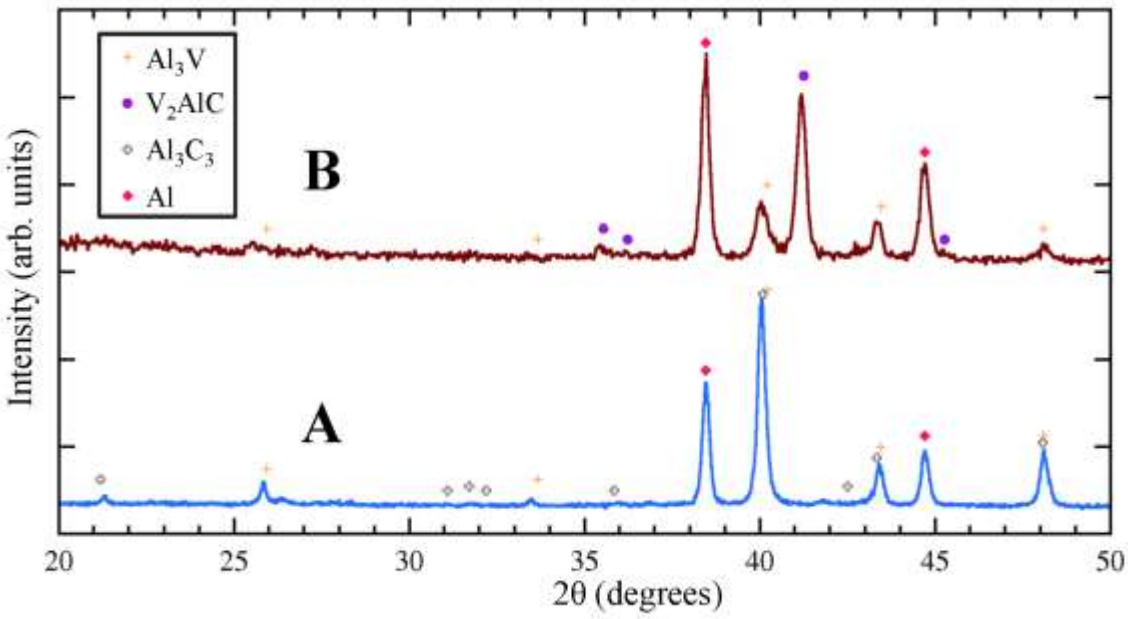

Figure 34. Typical diffraction patterns of DSC-WQ sample after equilibration at, a) 800 °C and, b) 1000 °C.

6.2. Discussion

6.2.1. Al-MAX Composites

MMCs attempt to combine the best properties of the matrix and reinforcement phase. Strong, lightweight, fracture resistant materials are desirable to various industries, and some MMCs may exhibit better mechanical and thermal properties than conventional materials. Additionally, having a readily machinable, near net-shape MMC component would be more easily incorporated into current industrial technologies.

The attractive mechanical properties of Mg-MAX composites [20, 29] spurred interest in Al-MAX composites. While V_2AlC was reported to be in thermodynamic equilibrium with Al at 1000 °C [30], no investigation of synthesizing two phase Al-V_2AlC composites was found in the literature. The phase stability of V_2AlC with Al was also unreported. Herein, we investigated the fabrication of Al-V_2AlC composites, as well as their equilibrium relations below 1000 °C.

V_2AlC was successfully formed *in situ* in the Al matrix. The volume fractions of the quenched AlR and VR composites, as determined from Rietveld analysis, were similar to those expected from their nominal compositions. The low relative density of the AlR (< 90 % dense) and VR (< 60 % dense) composites may be the result of several factors. 1) There is a positive volume change associated with the formation of V_2AlC (see below); 2) many Al particles do not break their oxide shells to form a molten matrix; and, 3) any grain coarsening process would also increase pore size. The absence of a continuous liquid phase throughout the sample (Fig. 29) cannot promote liquid phase sintering after the formation of the MAX phase, and any pores that form as a result of the

volume expansion may not be filled by liquid Al. It is well known that Al powders are not easily sintered and that reducing agents (Mg, Sn, Zn) are necessary to disrupt the aluminum oxide layer [69]. Our results suggest that the presence of carbide phases or Al-V intermetallics do not significantly increase the wetting of Al. Poor wetting by Al is also encountered when fabricating MMCs with other carbides, such as TiC, B_4C and SiC [31]. Increasing the density of Al-V_2AlC composites is requisite for maximizing mechanical properties and may be achieved by disrupting the oxide layer of the Al particles, but is beyond the scope of this study.

6.2.2. Phase stability and reaction

The stability of V_2AlC with Al was assessed using DSC (Figs. 32 and 33). Based on these results, together with knowledge of the Al-V binary system and the Al-V-C ternary phase diagram (Fig. 7), the following reaction paths for the DSC-WQ and DSC-FC samples were surmised.

The starting phases of the DSC-WQ sample were V_2AlC, Al, and Al_3V; these are the phases present in region 1 (Fig. 32). The exothermic peak, P1, may first seem surprising if Al is expected to melt; however, it is more likely that this is the decomposition of V_2AlC into Al_4C_3 and Al-rich intermetallics. Note that some Al may melt, suggested by the presence of P5, but this endothermic process may be masked by the large exothermic reaction between V_2AlC and Al. The temperatures that P1 span (660 – 700 °C) agree with the temperatures reported for the existence of $Al_{21}V_2$, $Al_{45}V_7$ and $Al_{23}V_4$ [41]. As our system is more V-rich, $Al_{23}V_4$ is expected to be the equilibrium phase, making the most likely reactions:

$$6\,V_2AlC + 48\,Al\,(liquid) \rightarrow 2\,Al_4C_3 + 3\,Al_{23}V_4 \quad (17)$$

$$3\,V_2AlC + 19\,Al\,(liquid) \rightarrow Al_4C_3 + 6\,Al_3V \quad (18)$$

Following the decomposition of the MAX phase, region 2 likely contains the phases Al_4C_3, Al_3V and $Al_{23}V_4$. The melting of the Al-rich intermetallic to form liquid Al and Al_3V (T = 734 °C) may be clearly identified as P2, and proceeds according to the reaction:

$$Al_{23}V_4 \rightarrow 11\,Al\,(liquid) + \,4\,Al_3V \quad (19)$$

Region 3 then contains Al_4C_3, Al_3V and liquid Al. These phases remain stable until P3 (T ≈ 940 °C), at which point Al_4C_3 and Al_3V react to form V_2AlC and liquid Al, according to:

$$Al_4C_3 + 6\,Al_3V \rightarrow 3\,V_2AlC + 19\,Al\,(liquid) \quad (20)$$

Region 4 is then in agreement with the reported ternary phase diagram at 1000 °C (Fig. 7) [30].

The associated volume change, ΔV, with Eq. 4 is +41.4 Å^3, as determined by:

$$\Delta V = \sum_{products} n_p V_p F_p^{-1} - \sum_{reactants} n_r V_r F_r^{-1} \quad (21)$$

Where *n* is the number of moles (formula units, #), *V* is the volume per unit cell (Å^3/unit cell), and *F* is the number of formula units per unit cell (#/unit cell). The subscript *p* and *r* stand for *product* and *reactant*, respectively. The constituent values are listed in Table 6.

Table 6. Parameters used in determining the volume change of in situ forming V_2AlC.

Component	n (#)	V (Å^3/unit cell)	F (#/unit cell)
Al_4C_3	1	241.6 [70]	3 [70]
Al_3V	6	119.9 [71]	2 [71]
V_2AlC	3	111.8 [72]	2 [22]
Al	19	66.1	4

Upon cooling, P4 is indicative of Eq. 20 proceeding in the reverse direction at T = 924 °C. Region 5 then has the same stable phases as region 3. The observed hysteresis (different temperature ranges between P3 and P4) may be attributed to an activation energy necessary to initiate the reaction. The lack of any other peaks during cooling, especially below 800 °C, is unexpected, as liquid Al must solidify or react at some point, presumably by 660 °C. It is possible that the Al slowly oxidized during testing and that no liquid Al existed during cooling. This hypothesis was corroborated by the observed increase in mass (1.2 wt. %) and XRD of the sample after testing, which demonstrated notable Al_2O_3 peaks.

The starting phases of the DSC-FC sample were Al_4C_3, Al_3V and Al-rich intermetallics (predominantly $Al_{23}V_4$); these are the phases present in region 1 (Fig. 33a). The small endothermic peaks, π1-π3, agree well with the melting temperatures of Al/$Al_{21}V_2$ (T = 660/664 °C), $Al_{45}V_7$ (T = 687 °C) and $Al_{23}V_4$ (T = 721 °C), respectively, and have the following reactions:

$$Al_{21}V_2 \rightarrow Al\ (liquid) + Al_{21}V_2 \quad (22)$$

$$Al_{21}V_2 \rightarrow Al\ (liquid) + Al_{45}V_7 \quad (23)$$

$$Al_{45}V_7 \rightarrow Al\ (liquid) + Al_{23}V_4 \quad (24)$$

Therefore, the phases in region 2 (Fig. 33a) are Al_4C_3, Al_3V, $Al_{23}V_4$, and trace amounts of liquid Al. The sharp exothermic peak, π4, must then be the same reaction as Eq. 3. The reason that this peak is shifted to a higher temperature than in the DSC measurements of the DSC-WQ sample is unknown; however, it seems likely that there would be less of a driving force for reaction during heating in the DSC-FC system because it was closer to equilibrium at lower temperatures (due to re-equilibration during furnace cooling). Thus, a larger activation energy may have been needed before the reaction (Eq. 3) could proceed. π5 (Fig. 33) is clearly the same as P3 in Fig. 32, with the onset temperature T ≈ 940 °C, and is indicative of reaction 4. The first peak observed during cooling, π6, was similar to P4 in Fig. 32 and confirmed the reversibility of Eq. 4 in this sample. Lastly, π7 shows that the liquid Al did solidify below T = 660 °C. The change in mass of this sample was < 0.3 wt. %, indicating that oxidation may not have been as severe.

6.2.3. Phase equilibria

Based on the totality of our XRD (Fig. 34a), SEM and DSC (Fig. 32) results of the equilibrated DSC-WQ composition at 800 °C, it is reasonable to conclude that the 3 apexes of this equilibrium triangle are: Al, Al_3V and Al_4C_3. An isothermal section of the Al-V-C phase diagram in the Al-rich corner has been constructed for 800 °C (Fig. 35). The starting molar composition (purple and orange points in Fig. 35), clearly falls within this equilibrium triangle. XRD after equilibration at 1000 °C (Fig. 34b) confirmed the phase relations – Al, Al_3V and V_2AlC – reported by Schuster, et al [30].

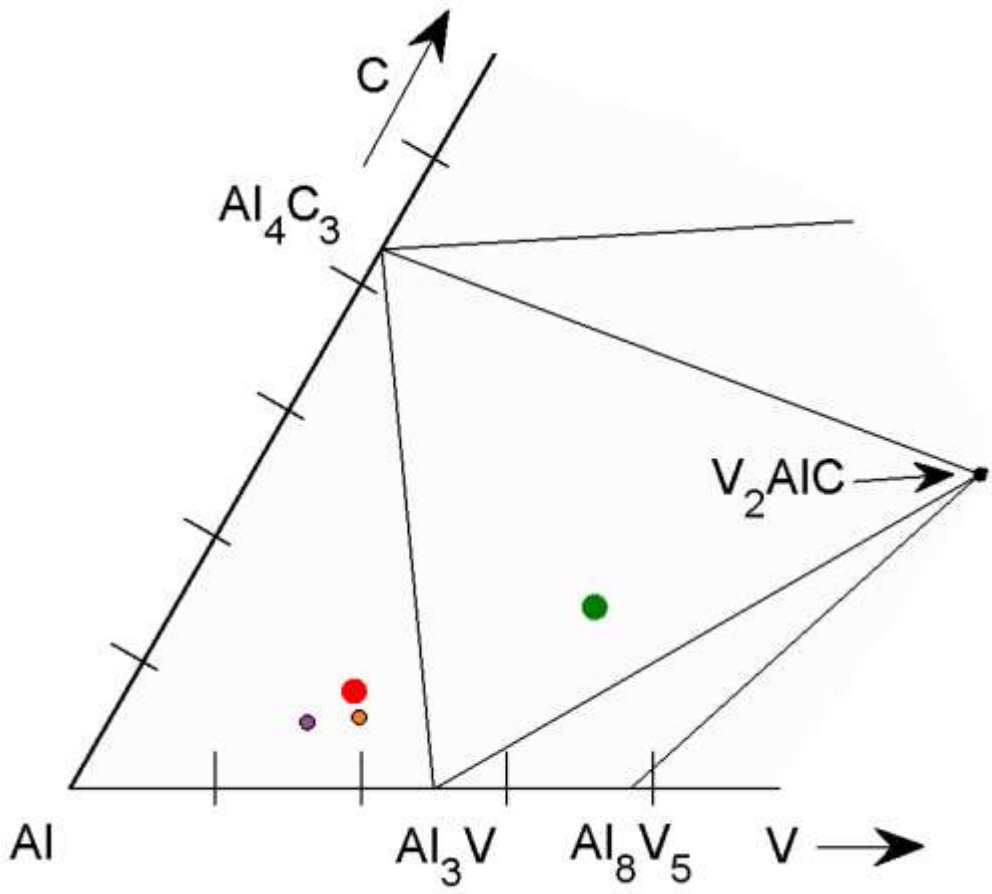

Figure 35. Phase equilibria in the Al-rich corner of the Al-V-C system at 800 °C. The nominal compositions of the AlR and VR composites are red and green points, respectively. Composition of the DSC-WQ sample as determined by Rietveld analysis of both 800 °C (green point) and 1000 °C (orange point) equilibration samples.

The discrepancy between the calculated starting molar composition, as determined by Rietveld analysis of the samples equilibrated at 800 and 1000 °C, may be the result of low intensity aluminum carbide peaks in the diffraction patters acquired after equilibration at 800 °C. This could underestimate the amount of carbon in the system and increase the Al:C ratio. Another possibility is that some Al may have evaporated or may have oxidized during equilibration at 1000 °C, lowering the Al:C ratio. Nevertheless, as

both compositions lie within the *same* equilibrium triangle at 800 and 1000 °C, this discrepancy in no way affects the conclusions of this study.

6.3. Summary of findings

- The synthesis of Al-V_2AlC composites was achieved by quenching from 1000 °C after soaking for 0.5, 2.5 or 10 h. Furnace cooled samples did not produce Al-V_2AlC composites.
- Differential scanning calorimetry demonstrated the instability of V_2AlC with liquid Al below ≈ 950 °C and a reaction mechanism was proposed to explain both DSC and XRD results.
- An isothermal section of the Al-V-C phase diagram in the Al-rich corner has been constructed for 800 °C. Both Al and V_2AlC were found to be in equilibrium with Al_3V and Al_4C_3, but not with each other.

Chapter 7.
Summary and Conclusions

The development of new MMCs is necessary for the progression of aerospace, automotive, power, and other industries. The high hardness typical of boride and carbide-containing composites also makes them attractive for high wear applications. Their chemical stability and neutron absorption properties render them appealing in nuclear and other demanding industrial settings. The attractive properties of MAX phases make them a desirable reinforcement phase in MMCs. Previous work with Mg-MAX composites spurred research in Al-MAX composites.

The development of Al-Ti_2AlC composites has been demonstrated to be unsuccessful using the melt infiltration technique, however, the use of B_4C has been demonstrated to increase the infiltration kinetics in the Ti_2AlC-B_4C-Al system between 900 – 1050 °C. As Ti_2AlC was found to react with Al at each investigated temperature, the characterization of phase equilibria for two compositions and a reaction mechanism were investigated. The results of this study demonstrate the equilibrium of Al-Al_3BC-TiB_2 and Al-TiC-TiB_2 in the quaternary system at 1000 °C, as well as the range in stoichiometries for each of these equilibrium planes (and their tetrahedron, with Al_4C_3 as the fourth apex). This investigation is a requisite step for the development of advanced composites in the Al-Ti-B-C system.

To avoid reactions with Al, V_2AlC was selected because of its reported thermodynamic equilibrium with Al at 1000 °C. *In situ* formed, two phase composites

were successfully developed in this system by quenching from 1000 °C; however, full density was not achieved. Furnace cooled samples did not demonstrate the Al-V_2AlC phase equilibrium. DSC results demonstrated the instability of V_2AlC with liquid Al below ≈ 950 °C. An isothermal section of the Al-rich corner of the Al-V-C phase diagram was characterized at 800 °C. The results of this study are necessary to selecting the processing conditions required for fabricating Al-V_2AlC composites.

Chapter 8.

Appendix A

A1. Rietveld refinement of BR composite

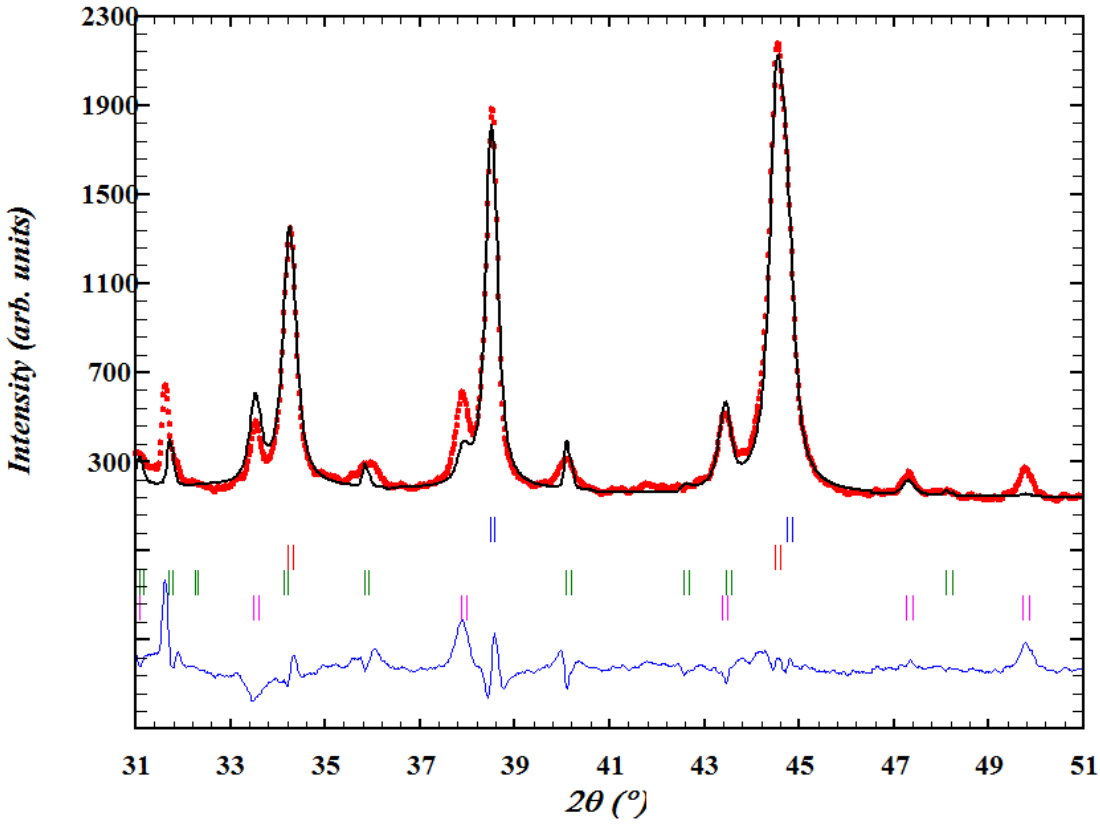

Figure A1. Rietveld refinement of the BR composite (black) compared to the diffraction pattern (red). The difference pattern is shown in blue.

A2. Rietveld refinement of TiR composite

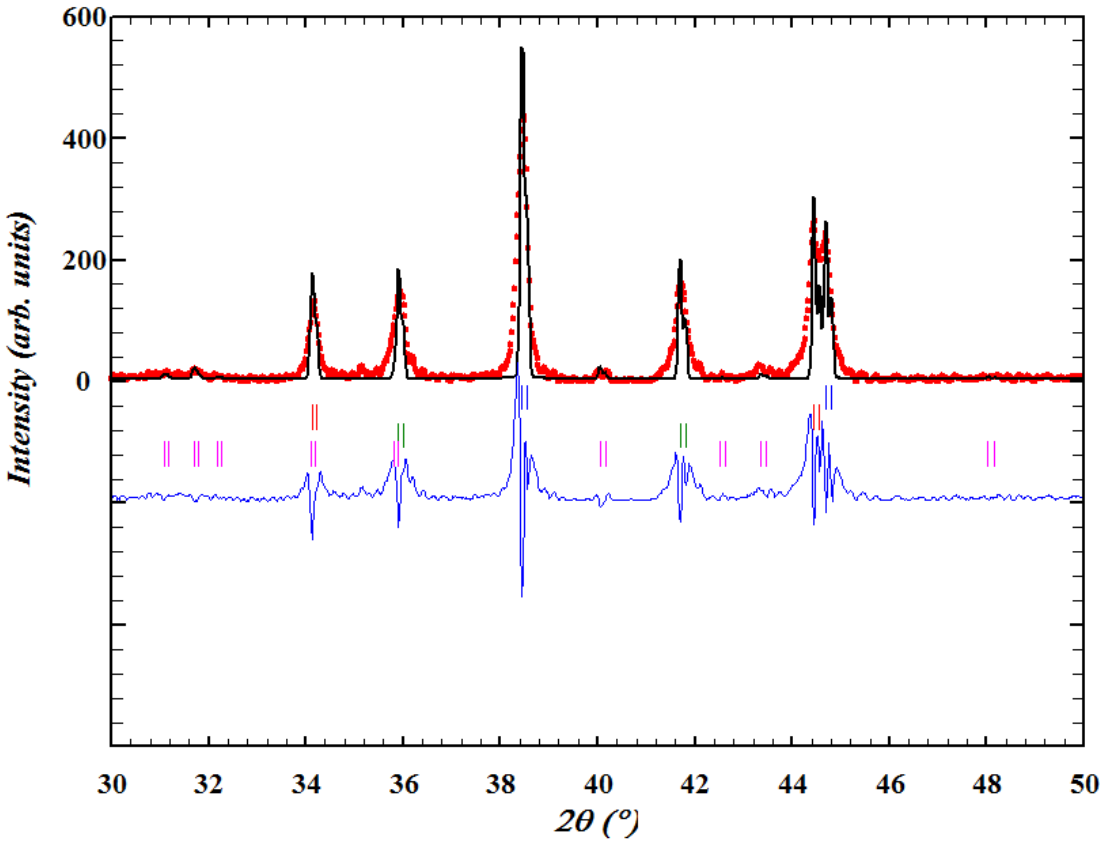

Figure A2. Rietveld refinement of the TiR composite (black) compared to the diffraction pattern (red). The difference pattern is shown in blue.

A3. Rietveld refinement of AlR composite

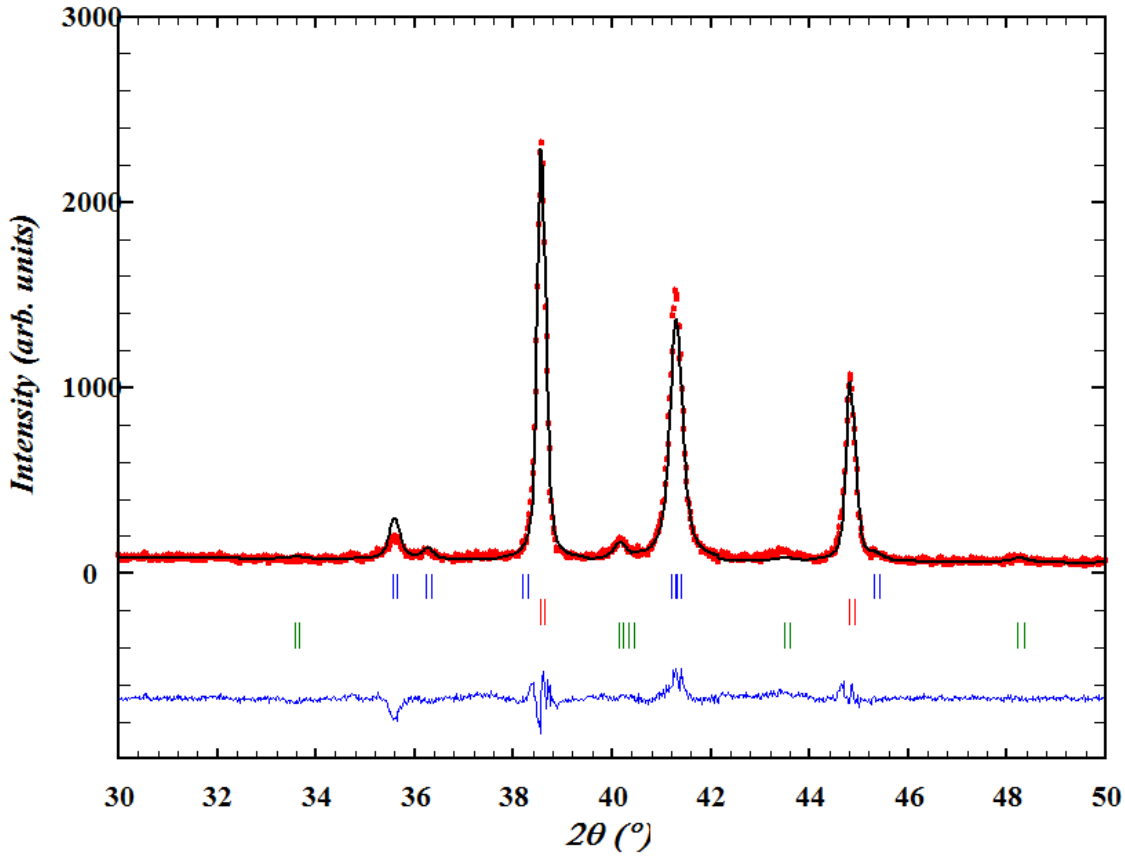

Figure A3. Rietveld refinement of the AlR composite (black) compared to the diffraction pattern (red). The residual difference is shown in blue.

A4. Rietveld refinement of VR composite

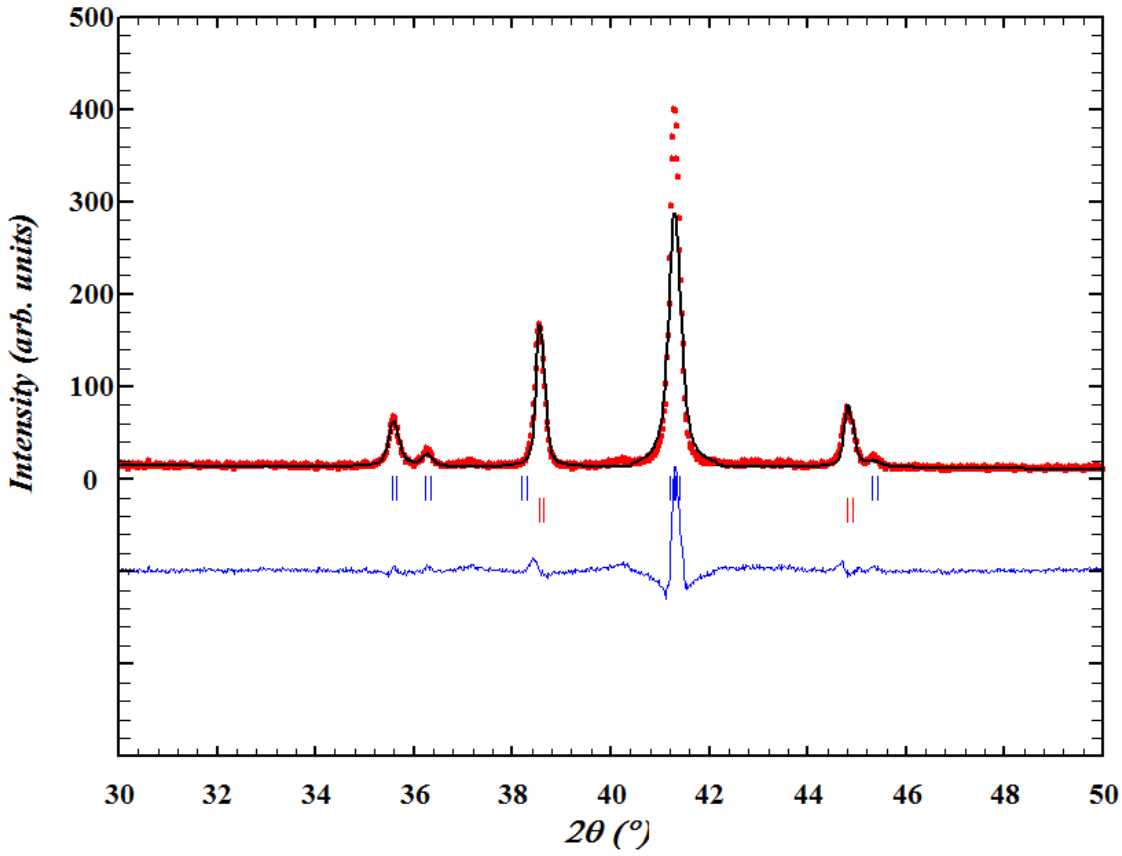

Figure A4. Rietveld refinement of the VR composite (black) compared to the diffraction pattern (red). The difference pattern is shown in blue.

A5. Rietveld refinement of DSC-WQ composite equilibrated at 800 °C

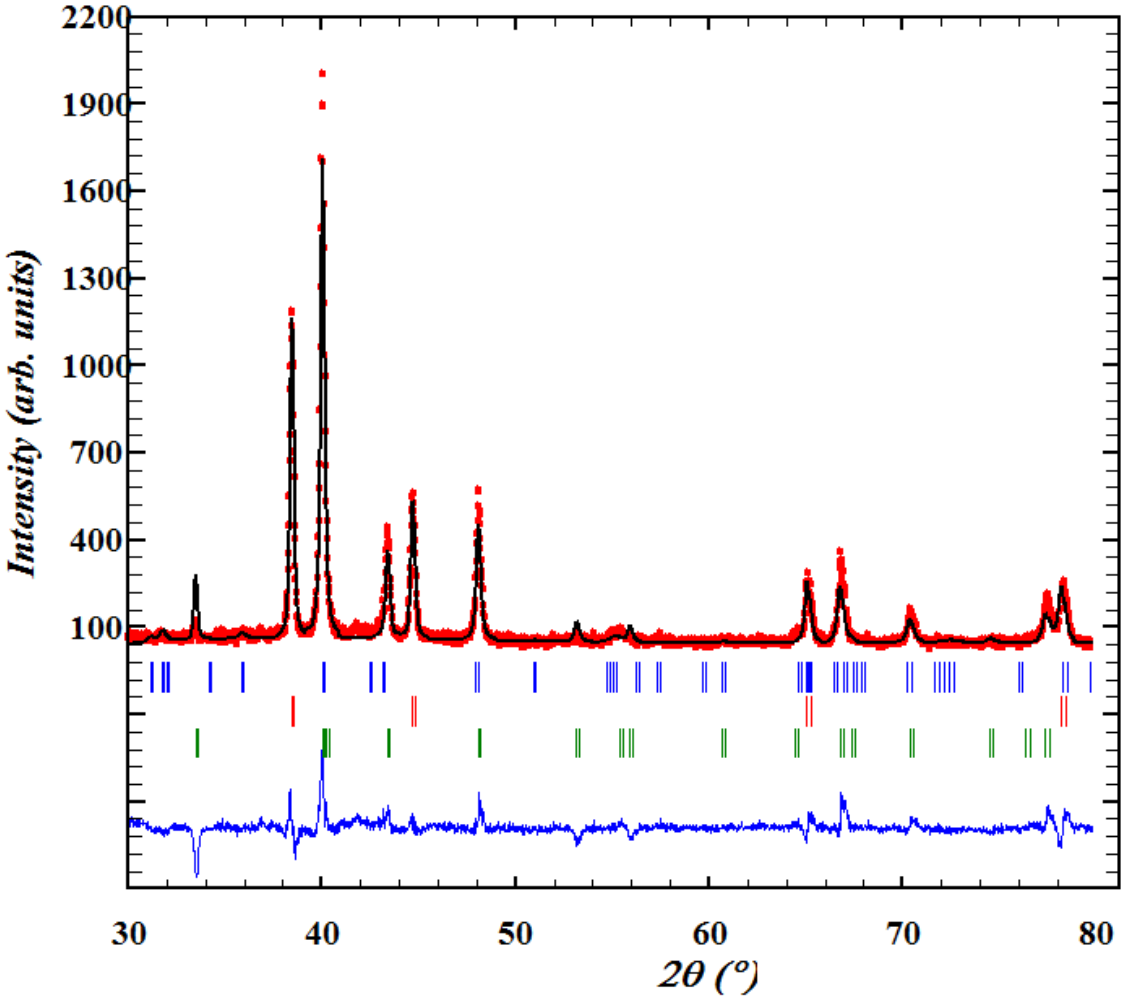

Figure A5. Rietveld refinement of the DSC-WQ composite (black) equilibrated at 800 °C compared to the diffraction pattern (red). The difference pattern is shown in blue.

A6. Rietveld refinement of DSC-WQ composite equilibrated at 1000 °C

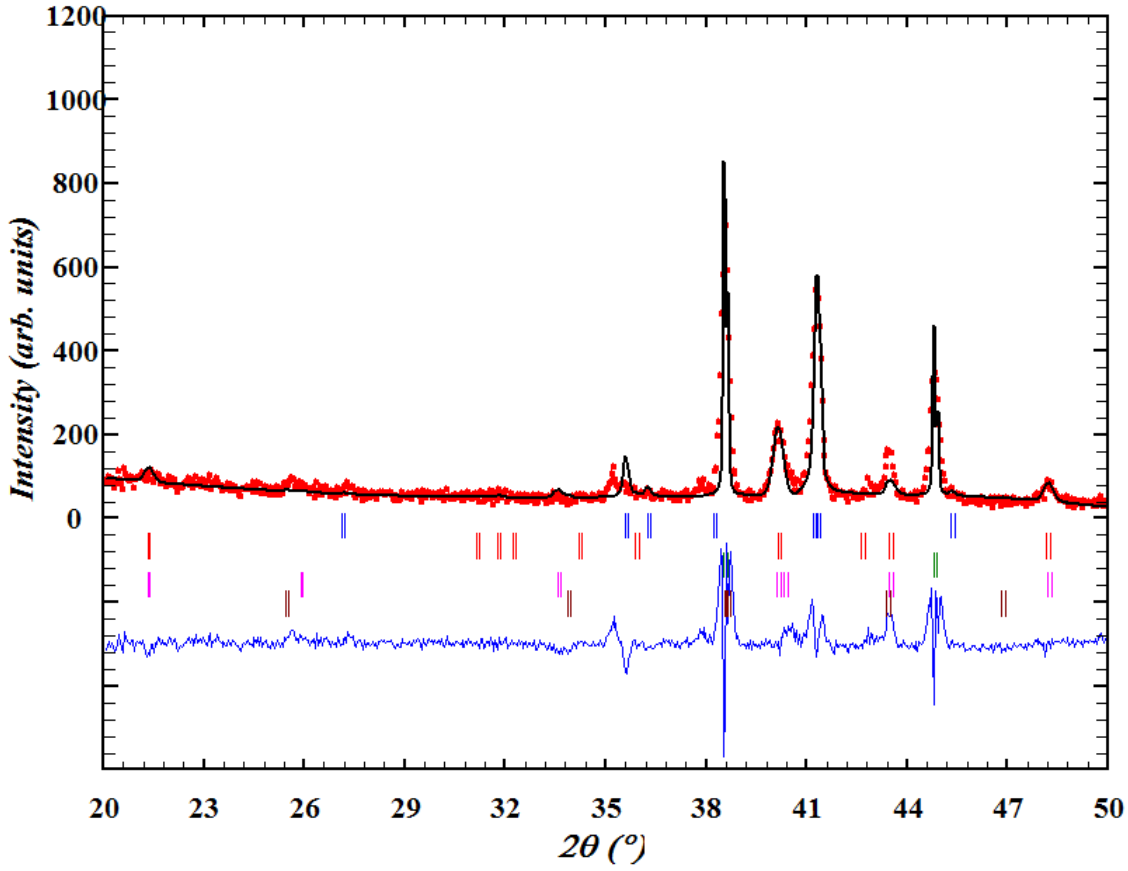

Figure A6. Rietveld refinement of the DSC-WQ composite (black) equilibrated at 1000 °C compared to the diffraction pattern (red). The difference pattern is shown in blue.

Chapter 9.

References

1. K.K. Chawla, Composite materials: science and engineering, Springer Science & Business Media, 2012.

2. D. Hou, G. Zhou and M. Zheng, Conch shell structure and its effect on mechanical behaviors, *Biomaterials*, 2004, **25**, p 751-756.

3. S.A. Wainwright, Mechanical design in organisms, Princeton University Press, 1982.

4. H. Binici, O. Aksogan and T. Shah, Investigation of fibre reinforced mud brick as a building material, *Construction and Building Materials*, 2005, **19**, p 313-318.

5. T. Clyne and P. Withers, An introduction to metal matrix composites, 1993.

6. L.F. Mondolfo, Aluminum alloys: structure and properties, Elsevier, 2013.

7. M.D. Sacks, H.W. LEE and O.E. Rojas, Suspension Processing of Al2O3/SiC Whisker Composites, *Journal of the American Ceramic Society*, 1988, **71**, p 370-379.

8. B.S. Lee and S. Kang, Low-temperature Processing of B4C–Al Composites via Infiltration Technique, *Materials Chemistry and Physics*, 2001, **67**, p 249-255.

9. A. Albiter, C.A. León, R.A.L. Drew and E. Bedolla, Microstructure and Heat-treatment Response of Al-2024/TiC Composites, *Materials Science and Engineering: A*, 2000, **289**, p 109-115.

10. H. Ding, X. Liu and J. Nie, Study of Preparation of TiB2 by TiC in Al Melts, *Materials Characterization*, 2012, **63**, p 56-62.

11. W.J. Wang, V. Gauthier-Brunet, G.P. Bei, G. Laplanche, J. Bonneville, A. Joulain and S. Dubois, Powder Metallurgy Processing and Compressive Properties of Ti3AlC2/Al Composites, *Materials Science and Engineering: A*, 2011, **530**, p 168-173.

12. L. Hu, A. Kothalkar, M. O'Neil, I. Karaman and M. Radovic, Current-Activated, Pressure-Assisted Infiltration: A Novel, Versatile Route for Producing Interpenetrating Ceramic–Metal Composites, *Materials Research Letters*, 2014, p 1-7.

13. D.B. Miracle, Metal Matrix Composites – From Science to Technological Significance, *Composites Science and Technology*, 2005, **65**, p 2526-2540.

14. I. Ibrahim, F. Mohamed and E. Lavernia, Particulate reinforced metal matrix composites—a review, *J Mater Sci*, 1991, **26**, p 1137-1156.

15. F.A. Girot, J. Quenisset and R. Naslain, Discontinuously-reinforced aluminum matrix composites, *Composites science and technology*, 1987, **30**, p 155-184.

16. Z. Zhang, K. Fortin, A. Charette and X. Chen, Effect of Titanium on Microstructure and Fluidity of Al–B4C Composites, *J Mater Sci*, 2011, **46**, p 3176-3185.

17. J. Salem and E. Fuller, Corrosion, Wear, Fatigue, and Reliability of Ceramics, John Wiley & Sons, 2009.

18. S. Amini, C. Ni and M.W. Barsoum, Processing, Microstructural Characterization and Mechanical Properties of a Ti2AlC/Nanocrystalline Mg-matrix Composite, *Composites Science and Technology*, 2009, **69**, p 414-420.

19. B. Anasori, S. Amini, V. Presser and M.W. Barsoum, Nanocrystalline Mg-Matrix Composites with Ultrahigh Damping Properties, *Magnesium Technology 2011*, 2011, p 463-468.

20. B. Anasori, E.N. Caspi and M.W. Barsoum, Fabrication and Mechanical Properties of Pressureless Melt Infiltrated Magnesium Alloy Composites Reinforced with TiC and Ti2AlC Particles, *Materials Science and Engineering: A*, 2014, **618**, p 511-522.

21. M.J. Nelson, Synthesis and Characterization of Ti3SiC2/Mg and Cr2AlC/Mg Composites, in: Materials Science and Engineering, Drexel University, 2014.

22. M.W. Barsoum, MAX Phases: Properties of Machinable Ternary Carbides and Nitrides, John Wiley & Sons, 2013.

23. M.W. Barsoum and T. ElRaghy, Synthesis and Characterization of a Remarkable Ceramic: Ti_3SiC_2, *Journal of the American Ceramic Society*, 1996, **79**, p 1953-1956.

24. M.W. Barsoum, D. Brodkin and T. ElRaghy, Layered Machinable Ceramics for High Temperature Applications, *Scripta Mater*, 1997, **36**, p 535-541.

25. M.W. Barsoum, M.C. Flemings, E.J. Kramer, S. Mahajan and P. Veyssiere, Physical Properties of the MAX Phases, *In: Encyclopedia of materials science and technology*, 2006.

26. D.J. Tallman, M. Naguib, B. Anasori and M.W. Barsoum, Tensile Creep of Ti_2AlC in Air in the Temperature Range 1000–1150 °C, *Scripta Mater*, 2012, **66**, p 805-808.

27. A. Kontsos, T. Loutas, V. Kostopoulos, K. Hazeli, B. Anasori and M.W. Barsoum, Nanocrystalline Mg–MAX Composites: Mechanical behavior Characterization via Acoustic Emission Monitoring, *Acta Materialia*, 2011, **59**, p 5716-5727.

28. M. Sundberg, G. Malmqvist, A. Magnusson and T. El-Raghy, Alumina Forming High Temperature Silicides and Carbides, in: 3rd Asian Meeting on Electroceramics (AMEC-3), 7-11 Dec. 2003, Elsevier, UK, 2004, pp. 1899-1904.

29. B. Anasori, Fabrication and Mechanical Properties of Pressureless Melt Infiltrated Magnesium Alloy Composites Reinforced with TiC and Ti2AlC Particles, in: Materials Science and Engineering, Drexel University, Philadelphia, 2014.

30. J. Schuster, H. Nowotny and C. Vaccaro, The ternary systems: Cr Al C, V Al C, and Ti Al C and the behavior of H-phases (M2AlC), *Journal of Solid State Chemistry*, 1980, **32**, p 213-219.

31. S.Y. Oh, J.A. Cornie and K.C. Russell, Wetting of Ceramic Particulates with Liquid Aluminum Alloys: Part II. Study of Wettability, *Metallurgical Transactions A*, 1989, **20**, p 533-541.

32. D.A. Weirauch, W.M. Balaba and A.J. Perrotta, Kinetics of the Reactive Spreading of Molten Aluminum on Ceramic Surfaces, *Journal of Materials Research*, 1995, **10**, p 640-650.

33. B. Zou, P. Shen and Q. Jiang, Reaction synthesis of TiC–TiB2/Al composites from an Al–Ti–B4C system, *J Mater Sci*, 2007, **42**, p 9927-9933.

34. H. Okamoto, Al−B (Aluminum-Boron), *Journal of Phase Equilibria and Diffusion*, 2006, **27**, p 195-196.

35. A. Hall and J. Economy, The Al(L) + AlB12 ↔ AlB2 Peritectic Transformation and its role in the Formation of High Aspect Ratio AlB2 Flakes, *JPE*, 2000, **21**, p 63-69.

36. D. Mirković, J. Gröbner, R. Schmid-Fetzer, O. Fabrichnaya and H.L. Lukas, Experimental Study and Thermodynamic Re-assessment of the Al–B System, *Journal of Alloys and Compounds*, 2004, **384**, p 168-174.

37. C. Qiu and R. Metselaar, Solubility of Carbon in Liquid Al and Stability of Al4C3, *Journal of alloys and compounds*, 1994, **216**, p 55-60.

38. T. Nukami and M.C. Flemings, In Situ Synthesis of TiC Particulate-reinforced Aluminum Matrix Composites, *Metall and Mat Trans A*, 1995, **26**, p 1877-1884.

39. M. Pietzka and J. Schuster, Summary of Constitutional Data on the Aluminum-Carbon-Titanium System, *JPE*, 1994, **15**, p 392-400.

40. V. Raghavan, Al− C− Ti (Aluminum-Carbon-Titanium), *Journal of Phase Equilibria and Diffusion*, 2006, **27**, p 148-149.

41. H. Okamoto, Al-V (Aluminum-Vanadium), *Journal of Phase Equilibria and Diffusion*, 2012, p 1-1.

42. J.L. Murray, Al-V (aluminum-vanadium), *Bulletin of Alloy Phase Diagrams*, 1989, **10**, p 351-357.

43. L. Brewer and H. Haraldsen, The Thermodynamic Stability of Refractory Borides, *Journal of The Electrochemical Society*, 1955, **102**, p 399-406.

44. H. Okamoto, B−Ti (Boron-Titanium), *Journal of Phase Equilibria and Diffusion*, 2006, **27**, p 303-303.

45. A.I. Gusev, Phase Equilibria in the Ternary System Titanium–Boron–Carbon: The Sections TiCy–TiB2 and B4Cy–TiB2, *Journal of Solid State Chemistry*, 1997, **133**, p 205-210.

46. O.N. Carlson, A.H. Ghaneya and J.F. Smith, The C−V (Carbon-Vanadium) system, *Bulletin of Alloy Phase Diagrams*, 1985, **6**, p 115-124.

47. H. Okamoto, C-V (Carbon-Vanadium), *Journal of Phase Equilibria and Diffusion*, 2010, **31**, p 91-92.

48. F. Thévenot, Boron Carbide—A Comprehensive Review, *Journal of the European Ceramic Society*, 1990, **6**, p 205-225.

49. A. Grytsiv and P. Rogl, Aluminium – Boron – Carbon, in: G. Effenberg and S. Ilyenko (Eds.) Refractory metal systems, Springer Berlin Heidelberg, 2009, pp. 10-38.

50. G. Will, On the Crystal Structure of AIB10, *Journal of the American Chemical Society*, 1963, **85**, p 2335-2336.

51. V.I. Matkovich, J. Economy and R.F. Giese, Presence of Carbon in Aluminum Borides, *Journal of the American Chemical Society*, 1964, **86**, p 2337-2340.

52. V. Raghavan, Al-B-Ti (Aluminum-Boron-Titanium), *Journal of Phase Equilibria and Diffusion*, 2005, **26**, p 173-174.

53. J.C. Viala, J. Bouix, G. Gonzalez and C. Esnouf, Chemical Reactivity of Aluminium with Boron Carbide, *J Mater Sci*, 1997, **32**, p 4559-4573.

54. V.T. Witusiewicz, A.A. Bondar, U. Hecht, J. Zollinger, L.V. Artyukh and T.Y. Velikanova, The Al–B–Nb–Ti system: V. Thermodynamic Description of the Ternary System Al–B–Ti, *Journal of Alloys and Compounds*, 2009, **474**, p 86-104.

55. J. Rodríguez-Carvajal, Recent Advances in Magnetic Structure Determination by Neutron Powder Diffraction, *Physica B: Condensed Matter*, 1993, **192**, p 55-69.

56. H. Li, S. Li, X. Chen and Y. Zhou, Spontaneous Pulverisation of Al4C3 Containing MAX Bulk Ceramics at Room Temperature, *Advances in Applied Ceramics*, 2014, **113**, p 184-188.

57. D.C. Halverson, A.J. Pyzik, I.A. Aksay and W.E. Snowden, Processing of Boron Carbide-Aluminum Composites, *Journal of the American Ceramic Society*, 1989, **72**, p 775-780.

58. Z. Zhang, X.-G. Chen and A. Charette, Fluidity and microstructure of an Al–10% B4C composite, *J Mater Sci*, 2009, **44**, p 492-501.

59. N. Dhokey, S. Ghule, K. Rane and R. Ranade, Effect of KBF4 and K2TiF6 on Precipitation Kinetics of TiB2 in Aluminium Matrix Composite, *Journal of Advance Material Letters*, 2011, **2**, p 210-216.

60. S. Zhang, Y. Zhao, G. Chen, X. Cheng, C. She, X. Wang and D. Wu, Effects of In Situ TiB2 Particle on Microstructures and Mechanical Properties of AZ91 Alloy, *Journal of Alloys and Compounds*, 2010, **494**, p 94-97.

61. J. Zhang, J. Lee, Y. Cho, S. Kim and H. Yu, Effect of the Ti/B4C Mole Ratio on the Reaction Products and Reaction Mechanism in an Al–Ti–B4C Powder Mixture, *Materials Chemistry and Physics*, 2014, **147**, p 925-933.

62. P. Lü, X. Yue, H. Ru and L. Yu, Microstructure and mechanical properties of B4C-TiB2-Al composites fabricated by vacuum infiltration, *Rare metals*, 2010, **29**, p 92-97.

63. C.J. Hsu, P.W. Kao and N.J. Ho, Intermetallic-reinforced aluminum matrix composites produced in situ by friction stir processing, *Materials Letters*, 2007, **61**, p 1315-1318.

64. M.M. Pacheco, R. Bouma and L. Katgerman, Combustion synthesis of TiB2-based cermets: modeling and experimental results, *Applied Physics A*, 2008, **90**, p 159-163.

65. A.J. Pyzik and D.R. Beaman, Al-B-C Phase Development and Effects on Mechanical Properties of B4C/Al-Derived Composites, *Journal of the American Ceramic Society*, 1995, **78**, p 305-312.

66. T. Matsubara, T. Shibutani, K. Uenishi and K.F. Kobayashi, Fabrication of a thick surface layer of Al3Ti on Ti substrate by reactive-pulsed electric current sintering, *Intermetallics*, 2000, **8**, p 815-822.

67. I.-J. Shon, B.-R. Kim, J.-M. Doh and J.-K. Yoon, Consolidation of binderless nanostructured titanium carbide by high-frequency induction heated sintering, *Ceramics International*, 2010, **36**, p 1797-1803.

68. R.G. Munro, Material properties of titanium diboride, *Journal of Research of the National Institute of Standards and Technology*, 2000, **105**, p 709-720.

69. G. Schaffer, T. Sercombe and R. Lumley, Liquid phase sintering of aluminium alloys, *Materials Chemistry and Physics*, 2001, **67**, p 85-91.

70. V.L. Solozhenko and O.O. Kurakevych, Equation of state of aluminum carbide Al4C3, *Solid State Communications*, 2005, **133**, p 385-388.

71. M. Jahnátek, M. Krajčí and J. Hafner, Interatomic bonding, elastic properties, and ideal strength of transition metal aluminides: A case study for Al 3 (V, Ti), *Physical Review B*, 2005, **71**, p 024101.

72. J.M. Schneider, R. Mertens and D. Music, Structure of V2AlC studied by theory and experiment, *Journal of Applied Physics*, 2006, **99**, p 013501.